# Experimental Study on Eutectic Reactions and Isothermal Phase Equilibrium at 1800 °C in Mo-rich Mo-Si-B Alloys

**Doctoral Thesis**

# Experimental Study on Eutectic Reactions and Isothermal Phase Equilibrium at 1800 °C in Mo-rich Mo-Si-B Alloys

**Seong-Ho Ha**

**Graduate School of Environmental Studies**

**Tohoku University**

# Contents

# CHAPTER 1

# INTRODUCTION

## 1.1 Backgrounds

With the global warming and the exhaustion of fossil fuels, considerable efforts have been devoted to develop alternative energy sources. However, there are some industrial areas strongly depending on the use of fossil fuels due to the operation by gas turbine such as power plant and air crafts. Thus, the improvement of the efficiency of gas turbines is another issue. Fig. 1.1 shows the cross section and the temperature and pressure profiles in a jet engine (GE90-115B) [1]. During the operation, air is taken from the atmosphere and sucked through the fan and compressor. The working fluid receives mechanical power from the compressor causing that pressure and temperature increase rapidly. At that moment, air is given proper conditions to be sent to the combustion chamber. In the chamber, the air is mixed with fuels and generates the combustion with high-pressure. Finally, the temperature and pressure reach peaks (estimated to about 1500 $^{\circ}$C in temperature) in the high-pressure turbine (HPT) next to the combustor [2].

High-pressure turbine blades of gas turbines are made of Ni-based superalloys [3]. However, the operating temperature of gas turbines (1500 °C) exceeds the melting point of Ni-base superalloys (about 1400 °C). In order to overcome this problem, two additional processes should be applied. One is the application of cooling system to the blades and another is that of low thermal conductivity coatings on the surface of the blades [2]. The use of the cooling system, however, eventually causes the reduction of the engine efficiency. Therefore, new turbine blade materials able to operate without the cooling system have been studied with refractory metal alloys and ceramics. Therefore, new heat-resistant materials beyond Ni-base superalloys so-called "ultra-high temperature materials" have been explored.

## 1.2 Mo-Si Based Alloy

### 1.2.1 Mo-Si-B Ternary System

In Mo-Si-B system, there are various silicide and boride phases, which the melting point is over 2000 °C, attractive for ultra-high temperature applications. Silicide phases such as $MoSi_2$, $Mo_5Si_3$ and $Mo_3Si$ have good oxidation resistance due to the formation of a protective silica glass scale. However, they are brittle due to their poor fracture toughness at room temperature: e.g., $MoSi_2$ has fracture toughness on the order of 3

$MPa \cdot m^{1/2}$ [4]. $Mo_5SiB_2$ ($T_2$), only the ternary compound in the Mo-Si-B system, has excellent ultra high temperature yield strength [5], good oxidation resistance [6] and relatively low density comparable to Ni-base superalloys, but also poor fracture toughness as low as ceramic [7]. Mainly, three kinds of alloy systems have been suggested for the Mo-Si-B ternary alloys so far. The first one was intermetallic alloys consisting of $Mo_5Si_3$, $T_2$ and $Mo_3Si$ pioneered by Akinc and collaborators [8-10]. The alloys showed excellent oxidation resistance at elevated temperatures. Especially, B remarkably improved the oxidation resistance of the alloys. Using the same alloy system, Nomura et al. [11] studied the oxidation-resistant coating utilizing their reliable oxidation resistance. The second one is $Mo_{ss}$-$Mo_3Si$-$T_2$ studied by Berczik et al. [12, 13]. While the alloy system is not as oxidation-resistant as $Mo_5Si_3$-$T_2$-$Mo_3Si$ alloys suggested by Akinc et al. [8-10], they showed improved fracture toughness due to the existence of a ductile phase, $Mo_{ss}$. Depending on the volume fraction and distribution of $Mo_{ss}$, the room and high temperature fracture toughness of the alloys can be significantly improved. The final one is $Mo_{ss}$-$T_2$ two-phase alloys suggested by Yoshimi et al. [14, 15]. Since the $T_2$ phase also has a two-phase region with $Mo_{ss}$ in the phase diagram [16] and a $Mo_{ss}$-$T_2$ two-phase eutectic reaction in a solidification route [17], the combination of ductile $Mo_{ss}$ and $T_2$ phases is a simple concept for alloy design to meet

excellent ultra-high temperature properties and room temperature fracture toughness, simultaneously. The yield strength of $Mo_{ss}$-$T_2$ two-phase alloys at 1500 ° C was investigated by Yoshimi et al. [15] (see Fig. 1.2). An examined $Mo_{ss}$-$T_2$ two-phase alloy showed extremely high yield strength, higher than that of Nb-Si based alloys, which is the most powerful competitor of the Mo-Si based alloys. The creep properties of $Mo_{ss}$-$T_2$ two-phase and $Mo_{ss}$-$Mo_3Si$-$T_2$ three-phase alloys were also studied by Kumar and his co-workers [18] (see Fig. 1.3). From the comparison using the Larson-Miller parameter (LMP), it was considered that the two and three phase Mo-based alloys have much more excellent creep properties than those of the Ni-based superalloy Rene 80 and the typical second generation Ni-base single crystal (2GSX) alloy.

### 1.2.2 Mo-transition Metal Carbides

Carbides are attractive candidates as the partner of Mo for ultra-high temperature applications because of their high hardness, thermal stability and excellent creep resistance as well as low density. Mo-TiC and Mo-ZrC alloys were studied by Kurishita et al. [19]. According to their report [19], hyper eutectic Mo-40mol%TiC consisted of coarse particles of TiC and fine Mo-TiC eutectic phase. The strength of Mo-40mol%TiC showed almost the same level as that of monolithic TiC at high temperature. Mo-ZrC alloy also showed high creep resistance in hyper eutectic 40mol%ZrC, which could be

resistant to the stress of 130 MPa for 1% strain in 100h at 1673K. 30mol%ZrC showed the high fracture toughness of 14.7 $MPa \cdot m^{1/2}$ at room temperature [20]. Suzuki et al. [21] investigated the microstructures and high temperature strength of eutectic Mo-XC (X=Ti, Zr and Hf). In their study [21], Mo-16mol%HfC alloy exhibited excellent high temperature strength in spite of a low volume fraction of ZrC. These Mo-carbide composites may meet the high temperature properties and room temperature fracture toughness, simultaneously. However, they also would have poor oxidation resistance at elevated temperature.

## 1.3 Objectives of This Study

Through the backgrounds, it is realized that Mo-Si-B based alloys are a front runner as ultra-high temperature materials for new turbine system applications in the future. This point has been guaranteed by a number of studies for ultra-high temperature properties including oxidation resistance [8-10] and room-temperature fracture toughness [20, 22]. However, we should recognize that we are standing on the first step for the development of Mo-Si-B alloys now and still have a long way to go for the achievement of the practical use of the alloys. Their phase diagrams in the ultra-high temperature range have not been well established, yet. Alloy design accompanying with

micro-and/or macro-alloying has been in the gray of the daybreak, and no commercial Mo-Si-B alloy has been proposed so far. Microstructure controlling and materials processing has been almost untouched. To promote and accelerate the development of Mo-Si-B based alloys, the establishment of their ternary phase diagrams in the ultra-high temperature range is urgently needed. Accurate quantitative composition analysis by electron probe micro-analysis (EPMA) must be required to investigate phase diagrams, but the quantitative analysis of B that is one of light elements causing the inaccuracy of the EPMA analysis will present problems on phase diagram and stability studies. Microstructure change and evolution are unavailable phenomena at ultra-high temperature, and these are essential for microstructure controlling and materials processing. On the other hand, the excellent mechanical properties of Ni-based superalloys are largely attributed to the γ/γ′ microstructure, which is formed during solidification. Consequently, as-cast microstructures and their formation process (or mechanism) are also very important for microstructure controlling. From these viewpoints, the microstructure formation and evolution and the isothermal phase equilibrium in the Mo-Si-B ternary system are mainly focused on for the development of Mo-Si-B based ultra-high temperature materials in this study. The thesis is divided into 6 chapters.

In chapter 2, it is attempted to establish the calibration method of EPMA for the quantitative composition analysis of Mo-rich Mo-Si-B ternary alloys. Originally-tailored standard samples were employed for the ZAF correction in EPMA, and statistical treatment is adopted to conduct accurate quantitative composition analysis for the Mo-Si-B ternary alloys. The correction accuracy of the method is assessed by comparison with chemically analyzed data.

Chapter 3 focuses on $Mo_{ss}$-$T_2$ and the $Mo_{ss}$-$Mo_3Si$-$T_2$ eutectic reactions. Their compositional points are investigated in a liquidus projection. Based on the reaction points determined by the quantitative analysis with the calibration developed in Chapter 2, the solidification routes of Mo-rich Mo-Si-B ternary alloys are suggested involving the $Mo_{ss}$-$T_2$ and the $Mo_{ss}$-$Mo_3Si$-$T_2$ eutectic reactions in this chapter.

In chapter 4, the main concern is on the phase formation and microstructure stabilization of Mo-rich Mo-Si-B ternary alloys at 1800 °C. The solubility and off-stoichiometry limits of constituent elements are quantitatively investigated for $Mo_{ss}$, $Mo_3Si$, $Mo_5Si_3$, $Mo_2B$, MoB and $T_2$ at 1800 °C. A phase diagram in the Mo-rich portion of the Mo-Si-B ternary system at 1800 °C is presented in this chapter.

In chapter 5, TiC is incorporated into Mo-rich Mo-Si-B ternary alloys to meet the weight reduction, strengthening at ultra-high temperature and toughening at lower

temperature of the Mo-Si-B alloys. Density change, microstructure formation and phase equilibrium at 1800 ° C are investigated for TiC-incorporated Mo-Si-B alloys.

In chapter 6, the main contents of each chapter were summarized.

**References**

[1] Zhao JC, Westbrook JH. MRS Bulletin 2003;**28:**622-627.

[2] Estrada C. Scientia et Technica Ano XIII 2007;**36**:297-301.

[3] Zhao JC, Westbrook JH. MRS Bulletin, 2003;**28;**622 – 627.

[4] Vasudévan AK, Petrovic J. Mater Sci Eng A 1992;**155**:1-17.

[5] Ito K, Ihara K, Tanaka K, Fujikura M, Yamaguchi M. Intermetallics 2001;**9:**591-602.

[6] Yoshimi K, Nakatani S, Suda T, Hanada S, Habazaki H. Intermetallics 2002;**10:**407-414.

[7] R. Mitra: Intl. Mater. Rev. **51 (**2006) 13-64.

[8] M. K. Meyer, M. J. Kramer, M. Akinc: Intermetallics **4 (**1996) 273-281.

[9] M. Akinc, M. K. Meyer, M. J. Kramer, A. J. Thom, J. J. Huebsch, B. Cook Intermetallics A261 (1999) 16-23.

[10] Meyer MK, Thom AJ, Akinc M. Intermetallics 1999;7:153-162.

[11] Nomura N, Suzuki T, Yoshimi K, Hanada S. Intermetallics 2003;11:735-742

[12] Berczik DM, United States Patent 1997;5,595,616.

[13] Berczik DM. United States Patent 1997;5,693,156.

[14] Yoshimi K, Nakatani S, Suda T, Hanada S, Habazaki H. Intermetallics 2002;**10**:407-414.

[15] Yoshimi K, Nakatani S, Nomura N, Hanada S. Intermetallics 2003;11:787-794.

[16] Nowotny H, Kieffer R, Benesovsky F. Planseeberichte Fuer Pulvermetallurgie 1957;**5:**86.

[17] Nunes CA, Sakidja R, Dong Z, Perepezko JH. Intermetallics 2000;**8:**327-337.

[18] Jain P, Kumar KS. Acta Materialia 2010;58:2124-2142.

[19] Kurishita H, Shiraishi J, Matsubara R, Yoshiaga H. J Jpn Inst Met 1985;**49**:963-971.

[20] Suzuki T, Nomura N, Yoshimi K, Hanada S. Mater Trans JIM 2000;**41**:1164-1167.

[21] Suzuki T, Matsumoto H, Nomura N, Yoshimi K, Hanada S. Trans Mater Res Soc Jpn 2001;**26**:307-310.

[22] Kruzic JJ, Schneibel JH, Ritchie RO. Scripta Materialia 2004;50:459-464.

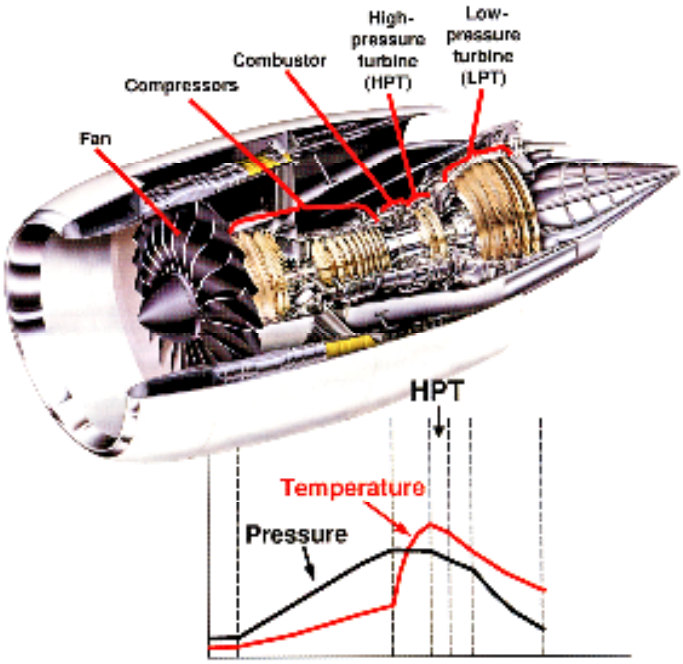


**Fig. 1.1 Cross section and profile of temperature and pressure in GE90-115B jet engine [1].**

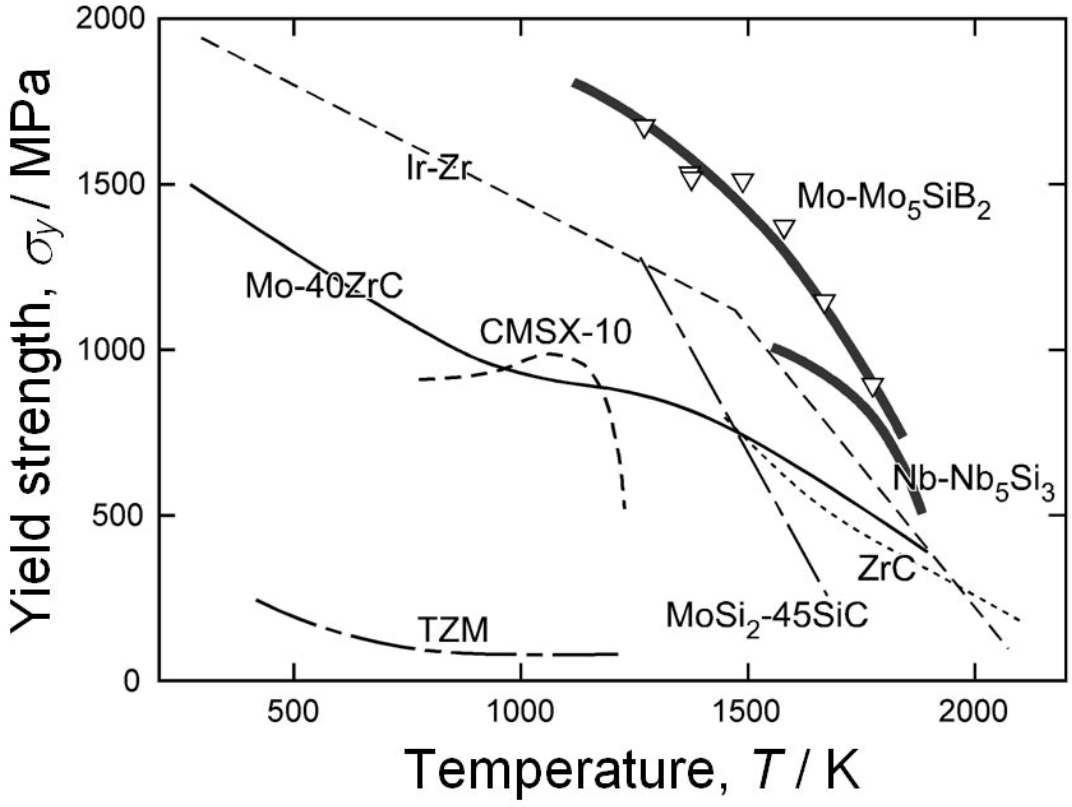


**Fig. 1.2 Yield strength of candidate materials shown by Yoshimi et al. [17].**

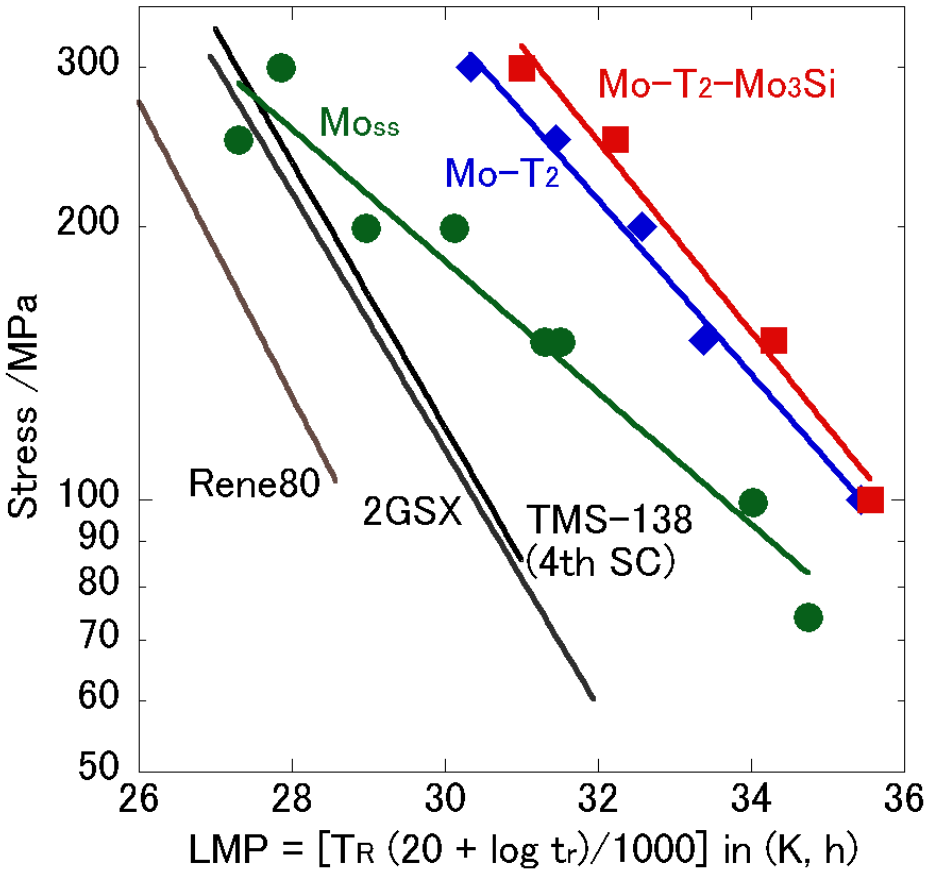


**Fig. 1.3 Larson–Miller parameter diagram showing a comparison of the creep resistance of the $Mo_{ss}$-$T_2$ two-phase and $Mo_{ss}$-$Mo_3Si$-$T_2$ three-phase alloys with the Ni-based superalloy Rene 80 and a typical Ni-based second generation single crystal (2GSX) alloy. [18].**

# CHAPTER 2

# Quantitative Analysis of Constituent Elements in Mo-Si-B System by FE-EPMA

## 2.1 Introduction

Recently, the Mo-Si-B ternary alloy system has been actively studied with respect to isothermal phase equilibria [1-3], microstructure evolution [1,4,5], ultra-high temperature strength [6,7], oxidation resistance [8-10], room temperature fracture toughness [11,12] and so on because of their high potentials for ultra-high temperature structural applications. The quantitative analysis of constituent elements conducted by electron-probe micro-analysis (EPMA) is crucially important to investigate the phase equilibria and to develop the alloy design of Mo-Si-B ternary alloys. However, the accurate element measurement by EPMA is interfered by inaccuracy in quantifying B for the Mo-Si-B system. In general, quantitative analysis by EPMA for light elements such as B, C, N and O is difficult because of their low fluorescence yield and the preferential absorption of X-rays from light elements [13]. In our earlier work [14], B concentration in a Mo-rich Mo-Si-B alloy was systematically overestimated by EPMA

compared with its chemical composition, and consequently Mo and Si concentrations were underestimated. Adequate calibration using proper standard samples is essential to raise the accuracy of quantitative analysis by EPMA. Unfortuately, no study on the calibration of quantitative analysis data by EPMA has been reported for the Mo-Si-B system. Perepezko and his coworkers reported the phase diagrams at 1600 °C of the Mo-rich portion of the Mo-Si-B ternary system [15]. The phase diagrams were experimentally obtained by quantitative composition measurements by EPMA. However, the details how to calibrate EPMA data was not described in there literature.

The purposes of this chapter are to tailor original Mo-Si-B standard samples in order to calibrate EPMA data by corresponding to chemically-analyzed composition data, and to attempt to raise the accuracy of the quantitative analysis using the standard samples for the Mo-Si-B alloy system.

## 2.2 Experimental Procedures

Six kinds of Mo-Si-B samples (S1-S6) were prepared by aiming to the single phases of $Mo_5SiB_2$ ($T_2$), Mo solid solution ($Mo_{ss}$), $Mo_3Si$, $Mo_5Si_3$ ($T_1$), $Mo_2B$ and MoB as standard samples for the calibration of quantitative analysis by EPMA. 0.5at% of Si or B was added into the borides or silicides to raise the accuracy for a small amount of

Si or B in the boride or silicide phases. In the case of $Mo_{ss}$, 1at% of Si and B were added since $Mo_{ss}$ was expected to have a relatively higher solubility of Si and/or B in the borides or silicides. The Mo-Si-B sample alloys of approx. 20g in weight were produced from pure Mo (99.99 wt%), Si (99.9999 wt%) and B (99.95 wt%) by a conventional arc-melting technique with a water-cooled copper crucible in an Ar atmosphere. Each alloy ingot was flipped after melting and re-melted more than 5 times to ensure compositional homogeneity as possible. Prior to each melting, the furnace was evacuated and filled with high-purity Ar gas several times. A commercially pure Ti ingot was preliminary melted before every melting to remove residual $O_2$ and $N_2$ gases as possible. There was not great difference in alloy weight between before and after melting. The atomic ratios of Mo, Si and B in the as-cast alloys were analyzed by inductively coupled plasma (ICP) - the optical emission spectrometry (OES) method. The details on the ICP-OES method was described elsewhere [16]. The impurity levels of Ti, Cu and W were also measured by the ICP-OES method. Specimens for the chemical analyses other analyses and observations were taken from the center of the ingots. Table 2.1 shows the chemically analyzed composition of the six samples. The chemical compositions were also plotted on the Mo-Si-B ternary phase diagram reported by Kim et al. [15] as shown in Fig. 2.1. Composition will be expressed as

atomic percent hereafter.

Heat treatment was carried out at 1800 °C for 24 h in an Ar atmosphere for Alloy S1 – S6. Constituent phases in the heat-treated alloys were identified by X-ray diffractometry (XRD) (Bruker D8 Advance) using the Cu-*Ka* radiation. Microstructures were observed by scanning electon microscopy (SEM) (JEOL JSM-6500F) with back-scattered electron (BSE) images. Quantitative composition analysis was performed by field-emission gun-type electron-probe micro-analysis (FE-EPMA) (JEOL JXA-8530F) operated at 15 kV and 20 nA. Pentaerythritol (PET) - H, Thallium acid phthalate (TAP) and Layered dispersion element (LDE) - 2H were used as dispersive crystals for the Mo, Si and B measurements, respectively, in FE-EPMA. As initial standard samples for FE-EPMA, pure Mo, $SiO_2$ or Si and B or $NdB_6$ were employed for quantifying Mo, Si and B. In order to obtain the average compositions of the alloys, multi-point measurements were carried out by FE-EPMA. The Mo-Si-B compositions at 400 (20 × 20) points were quantitatively analyzed with the electron-probe size of approx. 30 μm in diameter in an area of approx. 0.6 × 0.6 $mm^2$ as shown in Fig. 2.2.

## 2.3 Results and Discussion

### 2.3.1 Characterization of S1 – S6 Standard Samples

Fig. 2.3 shows the XRD profiles of the six samples after heat treatment at 1800 °C for 24 h. Alloy S1, prepared by aiming to the $Mo_5SiB_2$ ($T_2$) single phase, exhibited that almost all the peaks came from $T_2$ phase and a few from MoB, suggesting that the main phase was $T_2$ as aiming and a small amount of MoB was included. Similarly, it was found from the XRD profiles that the main phase of each alloy was $Mo_{ss}$ for S2, $Mo_3Si$ for S3, $Mo_5Si_3$ (T1) for S4, $Mo_2B$ for S5 and MoB for S6, respectively. Second and third phases detected are $Mo_2B$ for S2, $T_1$ and $T_2$ for S3, MoB for S5 and $T_2$ for S6. In Alloy S4, all of the peaks observed were only from T1, suggesting that the sample prepared was of T1 single phase.

The microstructures of the standard samples annealed at 1800 °C for 24 h are shown in Fig. 2.4. As seen in the figure, all of the samples contain second and third phases in the parent phase except for Alloy S4. The existence of second and third phases indicates that the solubility of Si or B in the borides or silicides and the off-stoichiometry of $T_2$ are quite limited even at 1800 °C. On the other hand, no second phase was observed in the BSE image of Alloy S4. No second phase was detected by XRD as mentioned above. These results indicate that the composition of Alloy S5 was in $T_1$ single-phase region, meaning that the solubility of B in $T_1$ is beyond 0.7 at%.

### 2.3.2 Dispersibility of Mo, Si and B Peaks in FE-EPMA Quantitative Analysis

Wavelength dispersive X-ray spectroscopic (WDX) curves of Mo, Si and B obtained from $T_2$ in Alloy S1, $Mo_{ss}$ in Alloy S2 and MoB in Alloy S6 are shown in Figs. 2.5 – 2.7. For $T_2$ and $Mo_{ss}$, the Mo-*La* and Si-*Ka* peaks were sharp and well-dispersive as shown in Figs. 2.5 and 2.6. The Mo-*La*□ peak was also sharp and no Si-*Ka* peak for MoB as shown in Fig. 2.7. In contrast, the B-*Ka* peak dispersed by LDE-2H has a problem on dispersibility against the Mo-*MZ* peak. For $Mo_{ss}$, a very faint peak of B-*Ka* X-ray lied on the foot of the Mo-*MZ* peak as shown in Fig. 2.5(a). A small and broadening peak of B-*Ka* X-ray intensity was detected for $T_2$; however, the peak clearly overlapped with the foot of the Mo-*MZ* peak as shown in Fig. 2.6(a). For MoB, a large but broadening peak of B-*Ka* X-ray intensity completely overlapped with the Mo-*MZ* peak as shown in Fig. 2.7(a). Basically, the weakness and broadening of the B-*Ka* peak caused by the low fluorescence yield and preferential X-ray absorption of B deteriorates the dispersibility of the B-*Ka* peak. In addition, the overlapping of the Mo-*MZ* peak with the B-*Ka* peak is definitely supposed to affect the quantitative analysis of B in the Mo-B and Mo-Si-B systems, though the Mo-*MZ* peak is not taken into account for the quantitative analysis of Mo. Therefore, the combination of Mo and B would generate an additional cause for the deterioration of B dispersibility.

Fig. 2.8 shows the compositions of $T_2$ in S1, $Mo_{ss}$ in S2, $Mo_3Si$ in S3, $T_1$ in S4,

$Mo_2B$ in S5, and MoB in S6 determined by FE-EPMA using the standard samples of commercially pure Mo, Si or $SiO_2$, and B or $NdB_6$. The determined compositions of all the phases are largely deviated from the chemical compositions of the samples S1-S6. For example, S4 consisted of $T_1$ single phase and its B concentration was about 0.7 at% as shown in Table 2.1. Thus, it was considered that all the compositions determined by FE-EPMA were under the overestimation of B. Furthermore, the determined compositions of some phases were quite different depending on standard samples, for example, as seen for $Mo_2B$. Consequently, it was demonstrated that the reliability of quantitative analysis by FE-EPMA is considerably deteriorated for the Mo-Si-B system if using the conventional standard samples with the conventional ZAF correction.

### 2.3.3 Calibration of FE-EPMA using Original Standard Samples Tailored for The Mo-Si-B Ternary System

As mentioned in 2.3.1, the prepared samples except S4 contained second and third phases though aiming to the single-phase regions of $T_2$, $Mo_{ss}$, $Mo_3Si$, $Mo_2B$ and MoB. Thus, the composition of each phase except $T_1$ in S4 must be slightly different from the chemical composition of each alloy shown in Table 2.1. In order to compensate this difference for quantitative analysis by FE-EPMA, the analyses were conducted in a wide area using the conventional standard samples as shown in 2.2, and then a statistical

treatment was applied to the calibration of the quantitative analyses for the measured data. For Alloy S1, the average compositions of two areas of 20 points × 20 points with an electron-beam of 30 μm in diameter (totally 800 points) were Mo-(11.8 ± 2.4)Si-(33.4 ± 3.7)B and Mo-(10.3 ± 3.1)Si-(34.8 ± 4.5)B, respectively, when the standard samples of commercially pure Mo, $SiO_2$ and $NdB_6$ were employed for the conventional ZAF correction. The total average composition of the 800 measured points was Mo-11.1Si-34.1B. Compared with the chemical composition of Mo-12.2Si-24.8B for Alloy S1, the average composition of Mo-11.Si-34.1B was largely deviated toward the B-rich side as shown in Fig. 2.9. Subsequently, a point having the composition closest to Mo-11.1Si-34.1B was found out among the 800 measured points, and through a re-measurement at that point the calibration algorithm of the ZAF correction was modified to correct the composition from Mo-11.1Si-34.1B to Mo-12.2Si-24.8B.

Similarly, the average compositions of 20 points × 20 points (totally 400 points) with an electron-beam of 30 μm in diameter were obtained using the standard samples of commercially pure Mo, $SiO_2$ and $NdB_6$ for S2 to S6. The obtained results are also shown in Fig. 2.9. All of the average composition values have systematic errors that were largely deviated toward the B-rich side compared with the chemical compositions. They were also calibrated by the method mentioned above.

Using the corrected calibration algorithm of the ZAF correction obtained for Alloys S1 to S6, $T_2$ in S1, $Mo_{ss}$ in S2, $Mo_3Si$ in S3, T1 in S4, $Mo_2B$ in S5 and MoB in S6 were quantitatively analyzed by FE-EPMA again. The obtained results are shown in Fig. 2.10. Compared with the results shown in Fig. 2.8, the B concentrations of all of the compositions examined were largely decreased. For example, the measured composition of $T_1$ in Alloy S4 consisting of the $T_1$ single phase was Mo-37.7Si-0.9B as shown in Table 2.2, which is in good agreement with the chemical composition of Mo-38.5Si-0.7B. The measured composition of $Mo_{ss}$ in Alloy S2 was slightly shifted to a Si-rich and B-poor side compared with the chemical composition of Alloy S2. As shown in Figs. 2.3 and 2.4(b), S2 had a small amount of $Mo_2B$ as second phase. From the evidence of the phase separation to $Mo_2B$, the compositional shift of $Mo_{ss}$ seen in Fig. 2.10 is very reasonable. No Si was detected from MoB in S6 as shown in Table 2.2. Most Si atoms added to S6 would be consumed to form $T_2$. The measured composition of MoB in S6 was Mo-49.8B (Table 2.2), which is very close to the stoichiometric composition of MoB and in good agreement with Mo-B binary phase diagrams [17]. The measured composition of $T_2$ in S1 was out of the $T_2$ single-phase region in the ternary phase diagram at 1600 °C by Kim et al. [16]. However, the chemical composition of Alloy S1 was Mo-12.2Si-24.8B. Besides the value was slightly shifted

toward a Si and B-poor side, there were the second and third phases of $Mo_5Si_3$ and MoB in Alloy S1 as shown in Figs. 2.3 and 2.4(a). These results indicate that the composition of $T_2$ in S1 was apparently in a Si and B-poor side, also strongly supporting the composition of $T_2$ measured by FE-EPMA. Therefore, the corrected compositions of all the phases obtained by FE-EPMA were quite reasonable, and thus it was concluded that the calibration method was very successful to analyze the composition of Mo-Si-B alloys by EPMA. If the conventional standard samples such as $Mo_{ss}$, Si or $SiO_2$ and B or $NdB_6$ were employed to the ZAF correction for the quantitative analysis by EPMA, B concentration would be always overestimated.

## 2.4 Conclusions

In this study, the accuracy of quantitative analysis by EPMA for the Mo-Si-B ternary system was investigated, and the eventually the calibration method with the statistical treatment using the original standard samples was successfully established for more accurate element measurements. Conclusions obtained in this study are as following:

1. The WDX peak of B-*Ka* for the quantitative analysis of B overlaps with that of Mo-*MZ*. The combination of Mo and B would cause worse inaccuracy for the

quantitative analysis of B in the Mo-Si-B system.

2. The quantitative analysis results obtained by FE-EPMA using the conventional standard samples such as commercially pure Mo, Si, B and so on systematically show the large overestimation of B for all the samples examined.

3. The calibration method modified using the original standard samples with the statistical treatment provided good accuracy within 0.1at%-order data-scattering for the quantitative analysis in the Mo-Si-B system. By the corrected calibration method, the compositions of $T_2$, $Mo_{ss}$, $Mo_3Si$, $Mo_5Si_3$, $Mo_2B$ and MoB were quantitatively determined with good accuracy.

4. The determined composition of $T_2$ phase balanced with MoB and Mo5Si3 at 1800 °C was slightly shifted toward a B- and Si-poor composition from its stoichiometric composition, which was out of the $T_2$ single-phase region in the phase diagram at 1600 °C reported previously.

**References**

[1] Katrych S, Grytsiv A, Bondar A, Rogl P, Velikanova T, Bohn M. J Alloy Compd 2002;347:94-100.

[2] Nowotny H, Kieffer R, Benesovsky F. Planseeberichte Fuer Pulvermetallurgie 1957;**5:**86.

[3] Nunes CA, Sakidja R, Perepezko JH. in Structural Intermetallics 1997 ed by Nathal MV, Darolia R, Liu CT, Martin PL, Miracle DB, Wagner R, Yamaguchi M; TMS, Warrendale, PA, 831-839.

[4] Nunes CA, Sakidja R, Dong Z, Perepezko JH. Intermetallics 2000;**8:**327-337.

[5] Yang Y, Chang YA. Intermetallics 2005;**13:**121-128.

[6] Schneibel JH. Intermetallics 2003;**11**:625-632.

[7] Yoshimi K, Nakatani S, Nomura N, Hanada S. Intermetallics 2003;**11**:787-794.

[8] Meyer MK, Thom AJ, Akinc M. Intermetallics 1999;**7**:153-162.

[9] Yoshimi K, Nakatani S, Suda T, Hanada S, Habazaki H. Intermetallics 2002;10:407-414.

[10] Nomura N, Suzuki T, Yoshimi K, Hanada S. Intermetallics 2003;**11**:735-742.

[11] Sturm D, Heilmaier M, Schneibel JH, J´ehanno P, Skrotzki B, Saage H. Mater Sci Eng A 2007;**463**:107-114.

[12] Choe H, Chen D, Schneibel JH, Ritchie RO, Intermetallics 2001;**9**;319-329.

[13] Birajdar B, Peranio N, Eibl O. Microsc Microanal 2007;**13**:290-291.

[14] Ha SH, Yoshimi K, Maruyama K, Tu R, Goto T. Materials Transactions 2010;**51**:1699-1074.

[15] Kim ST, Perepezko JH. J Phase Equilib Diffus 2006;**27:**605-613.

[16] Danzaki Y, Wagatsuma K, Syoji T, Yoshimi K. Fresenius J Anal Chem 2001;**369:**184-186.

[17] Spear KE, Liao PK. Bull Alloy Phase Diag. 1988;9:457-466.

**Table 2.1 Nominal and chemically analyzed compositions of samples.**

| Alloy | Nominal composition | | Chemical composition | | | | |
|---|---|---|---|---|---|---|---|
| | Si (at%) | B (at%) | Si (at%) | B (at%) | Ti (ppm) | Cu (ppm) | W (ppm) |
| S1 | 12.8 | 25 | 12.2 | 24.8 | <10 | <10 | <100 |
| S2 | 1 | 1 | 1.1 | 1.2 | <10 | <10 | 140 |
| S3 | 24.9 | 0.5 | 25.6 | 0.5 | <10 | <10 | <100 |
| S4 | 37.3 | 0.5 | 38.5 | 0.7 | <10 | <10 | <100 |
| S5 | 0.5 | 33.2 | 0.50 | 33.0 | <10 | <10 | <100 |
| S6 | 0.5 | 49.8 | 0.50 | 49.1 | <10 | <10 | <100 |

**Table 2.2 Compositions of constituent phases in Mo-rich portion of Mo-Si-B ternary system analyzed by EPMA with pure B and $NdB_6$ for B standard sample.**

| Phase | Si: $SiO_2$, B: pure B | | | B: $NdB_6$ | | |
|---|---|---|---|---|---|---|
| | Mo | Si | B | Mo | Si | B |
| $T_2$ | 53.8 | 9.0 | 37.2 | 53.5 | 8.5 | 38 |
| $Mo_{ss}$ | 89.0 | 3.9 | 7.1 | 88.8 | 3.8 | 7.4 |
| $Mo_3Si$ | 70.1 | 23.7 | 6.2 | 69.9 | 23.6 | 6.5 |
| $Mo_5Si_3$ | 54.8 | 37.6 | 7.5 | 54.9 | 37.6 | 7.5 |
| $Mo_2B$ | 56.9 | 0.4 | 42.7 | 56.0 | 0.5 | 43.5 |
| MoB | 42.1 | 0.0 | 57.9 | 41.1 | 0.0 | 58.9 |

| Phase | Si: pure Si | | |
|---|---|---|---|
| | Mo | Si | B |
| $T_2$ | 53.7 | 9.1 | 37.1 |
| $Mo_5Si_3$ | 54.9 | 37.2 | 8.0 |
| $Mo_2B$ | 56.6 | 0.4 | 42.9 |

**Table 2.3 Averages of 400 points measurements for each sample.**

| Alloy | Average for 400 points (standard deviation) | | |
|---|---|---|---|
| | Mo | Si | B |
| S2 | 94.6 (±2.1) | 0.8 (±0.2) | 4.6 (±2.1) |
| S3 | 66.3 (±1.2) | 24.0 (±0.9) | 9.6 (±1.1) |
| S4 | 59.4 (±1.7) | 37.2 (±1.4) | 3.4 (±0.8) |
| S5 | 52.2 (±1.0) | 0.5 (±0.4) | 47.3 (±1.1) |
| S6 | 38.6 (±0.3) | 0.4 (±0.5) | 60.9 (±0.6) |

**Table 2.4 Compositions of constituent phases in Mo-rich portion of Mo-Si-B ternary system analyzed by EPMA with the standard samples prepared in this study.**

| Phase | Standard sample S1-S6 | | |
|---|---|---|---|
| | Mo | Si | B |
| $T_2$ | 63.2 | 13.3 | 23.5 |
| $Mo_{ss}$ | 96.9 | 2.0 | 1.1 |
| $Mo_3Si$ | 73.9 | 25.7 | 0.4 |
| $Mo_5Si_3$ | 61.4 | 37.7 | 0.9 |
| $Mo_2B$ | 65.7 | 0.3 | 34.0 |
| MoB | 50.2 | 0.0 | 49.8 |

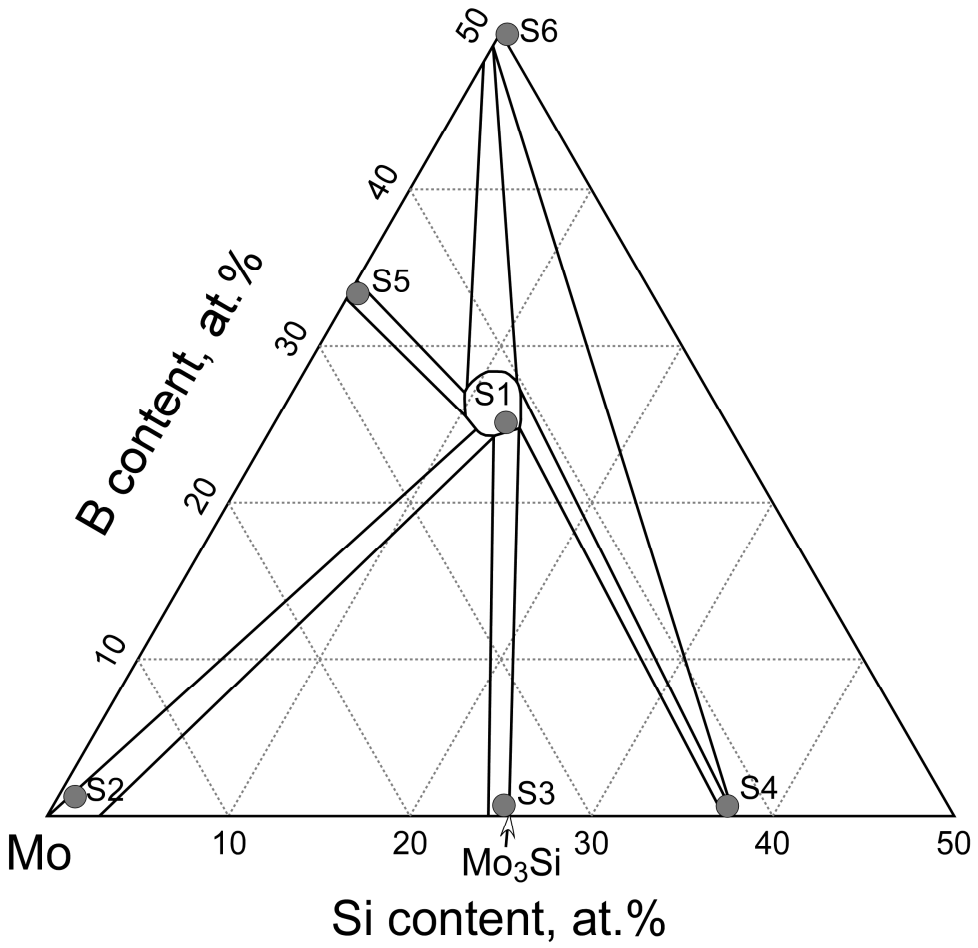


**Fig. 2.1 Chemically analyzed compositions of all the examined samples plotted in the1600 ˚C isothermal Mo-Si-B phase diagram by Kim et al. [13] and the liquidus projection by Yang et al. [9].**

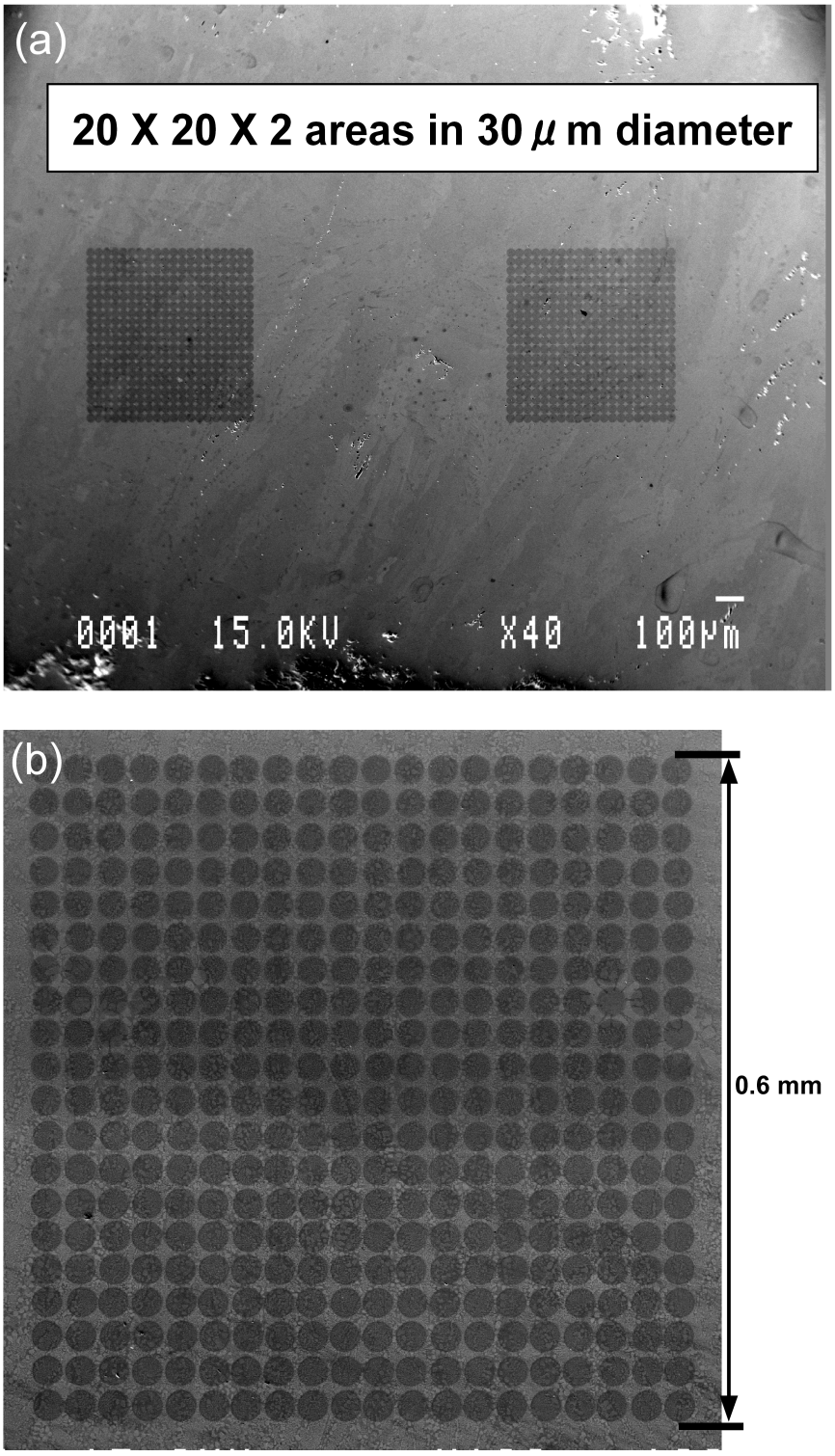


**Fig. 2.2 800 point measurements; (a) analyzed surface and (b) area of 400 point measurements.**

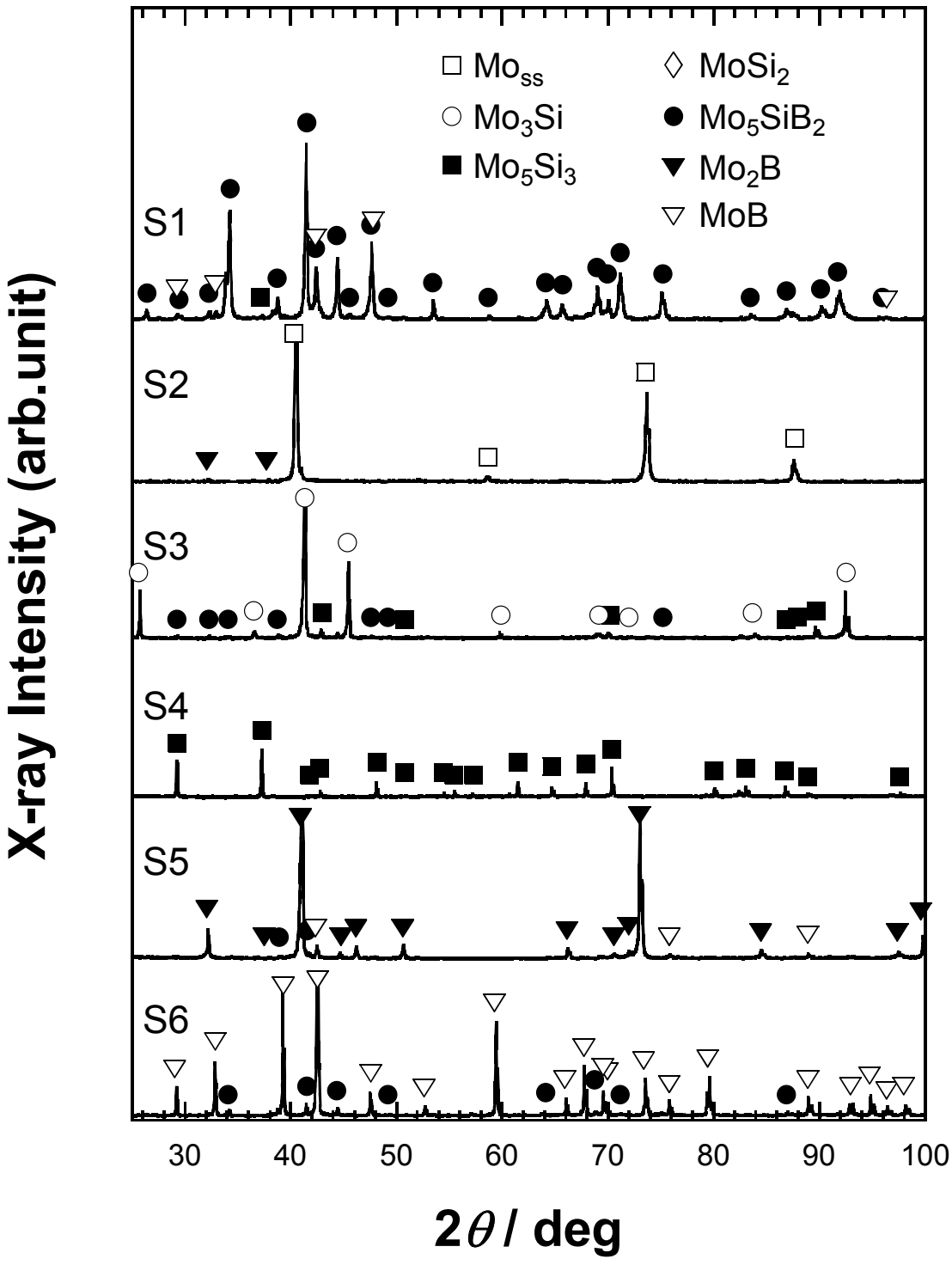


**2.3 XRD results of (a) S1, (b) S2, (c) S3, (d) S4, (e) S5 and (f) S6 alloys after heat treatment at 1800 ˚C.**

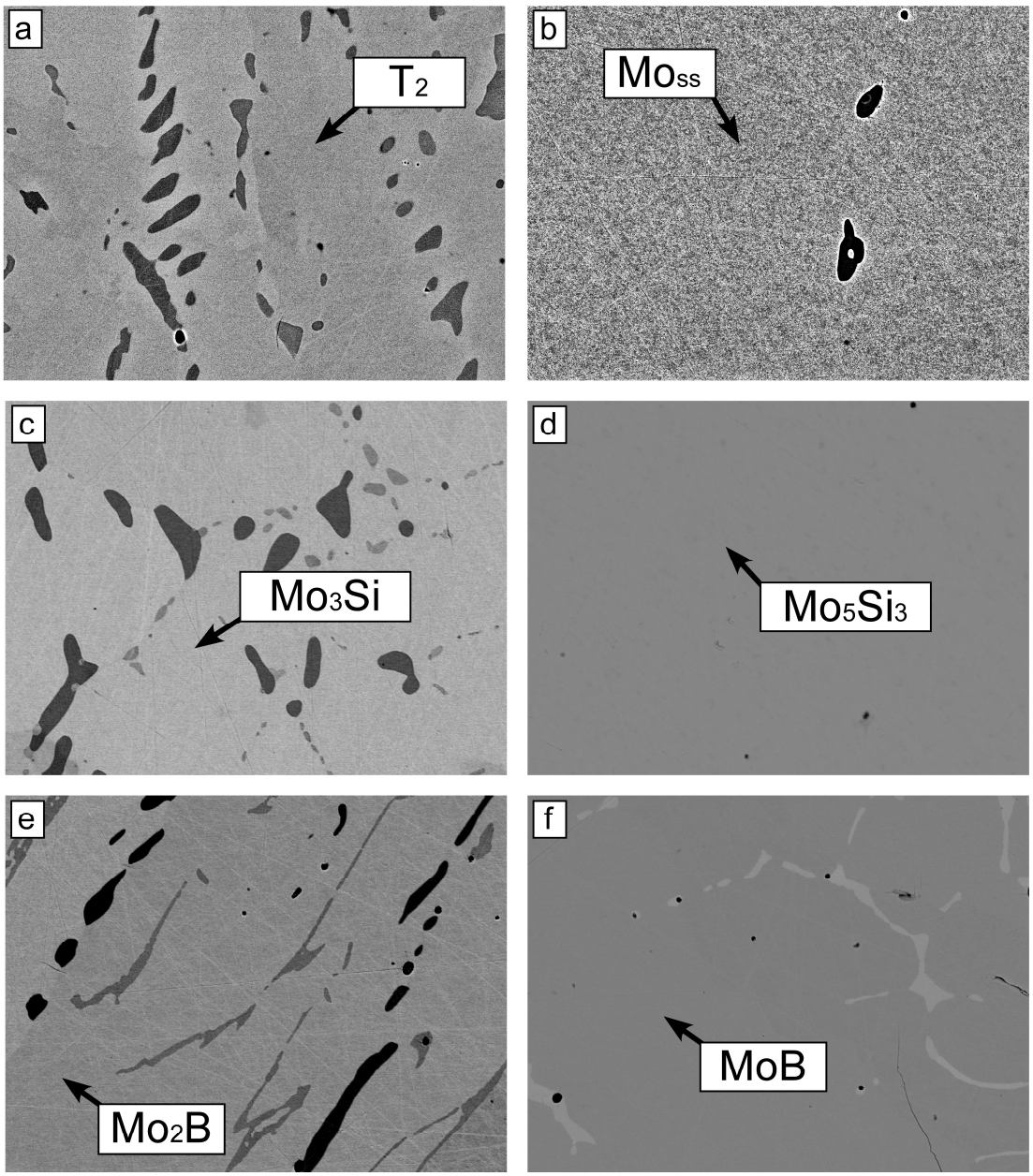


**Fig. 2.4 BSE images of (a) S1, (b) S2, (c) S3, (d) S4, (e) S5 and (f) S6 alloys after heat treatment at 1800 ˚C.**

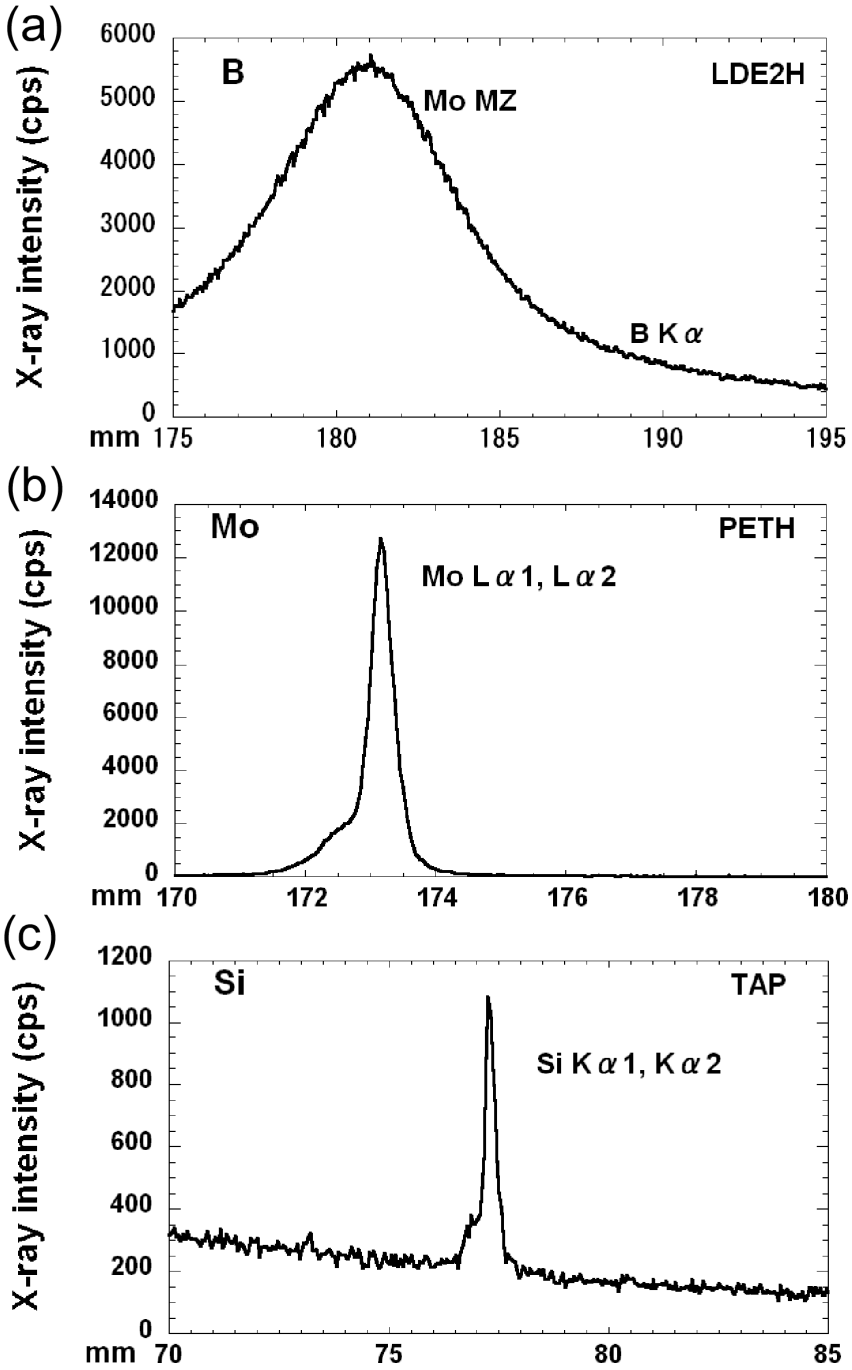


**Fig. 2.5 WDX peak of (a) B, (b) Mo and (c) Si for $Mo_{ss}$ obtained in this study.**

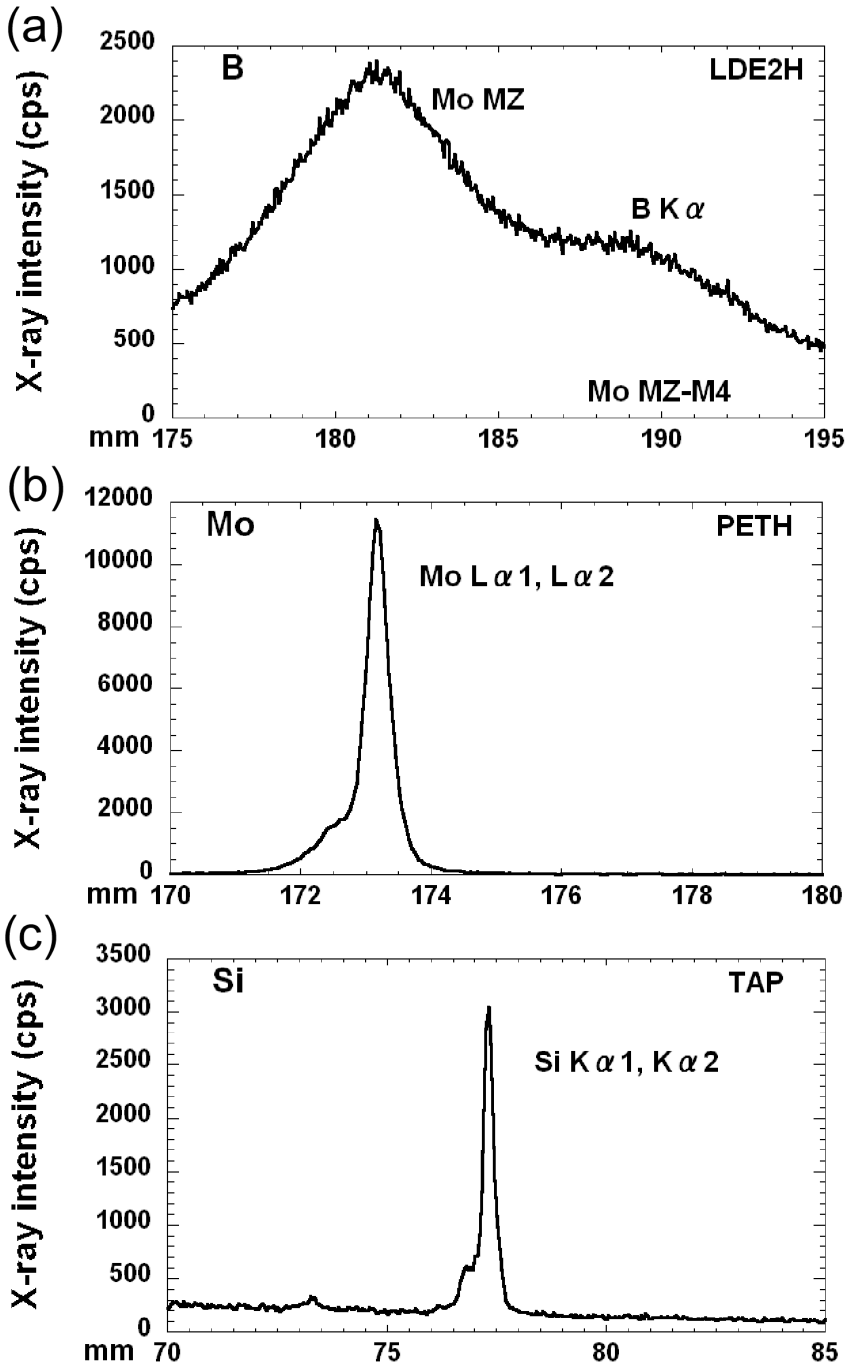


**Fig. 2.6 WDX peak of (a) B, (b) Mo and (c) Si for $T_2$ obtained in this study.**

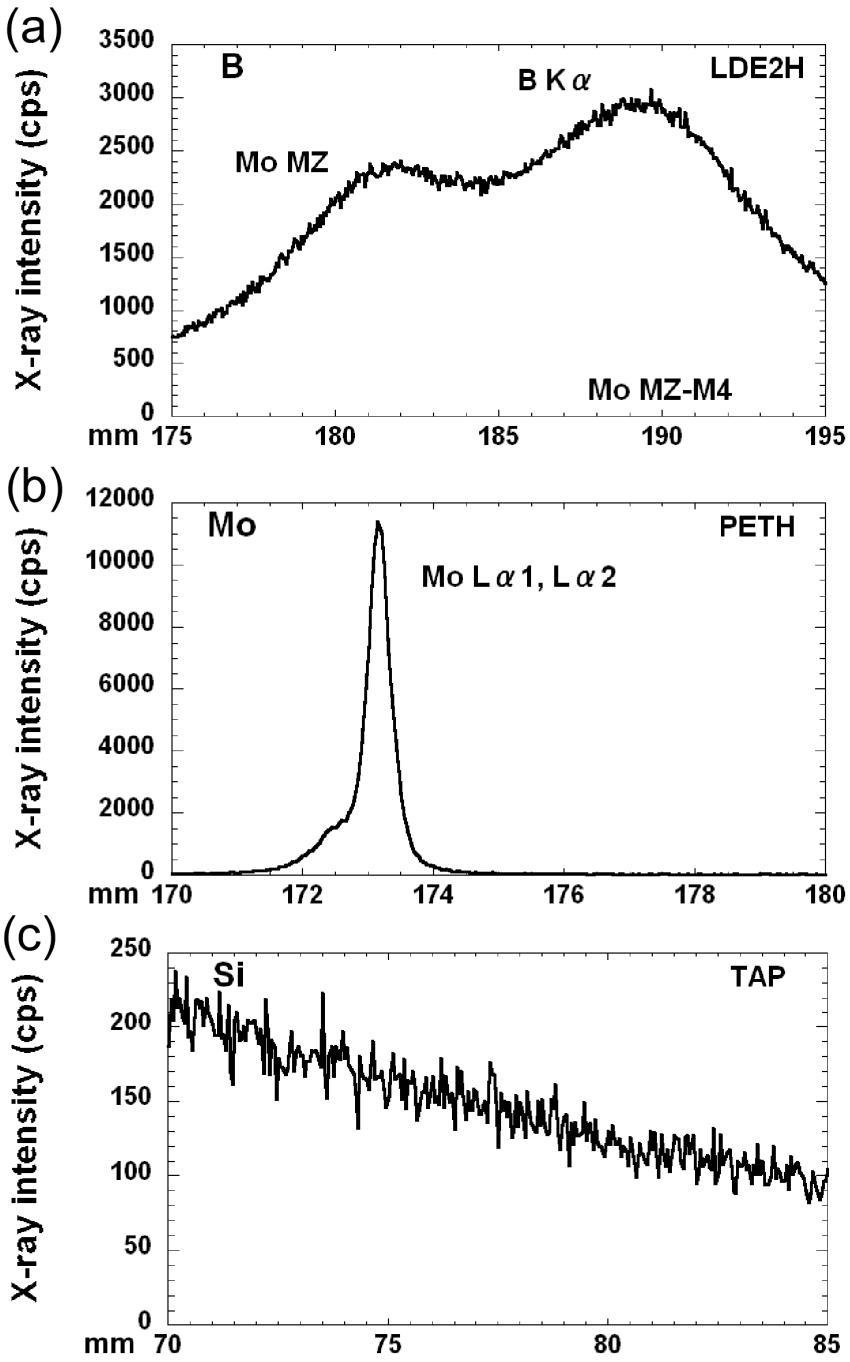


**Fig. 2.7 WDX peak of (a) B, (b) Mo and (c) Si for MoB obtained in this study.**

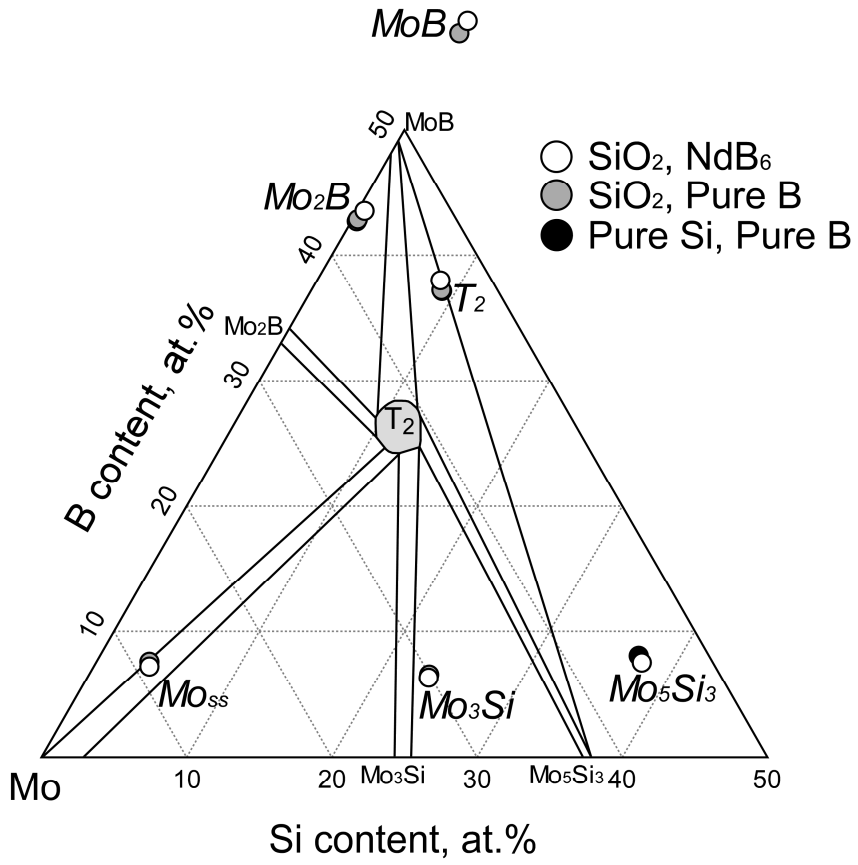


**Fig. 2.8 Compositions of constituent phases in Mo-rich portion of Mo-Si-B ternary system analyzed by EPMA with pure B and $NdB_6$ for B standard sample.**

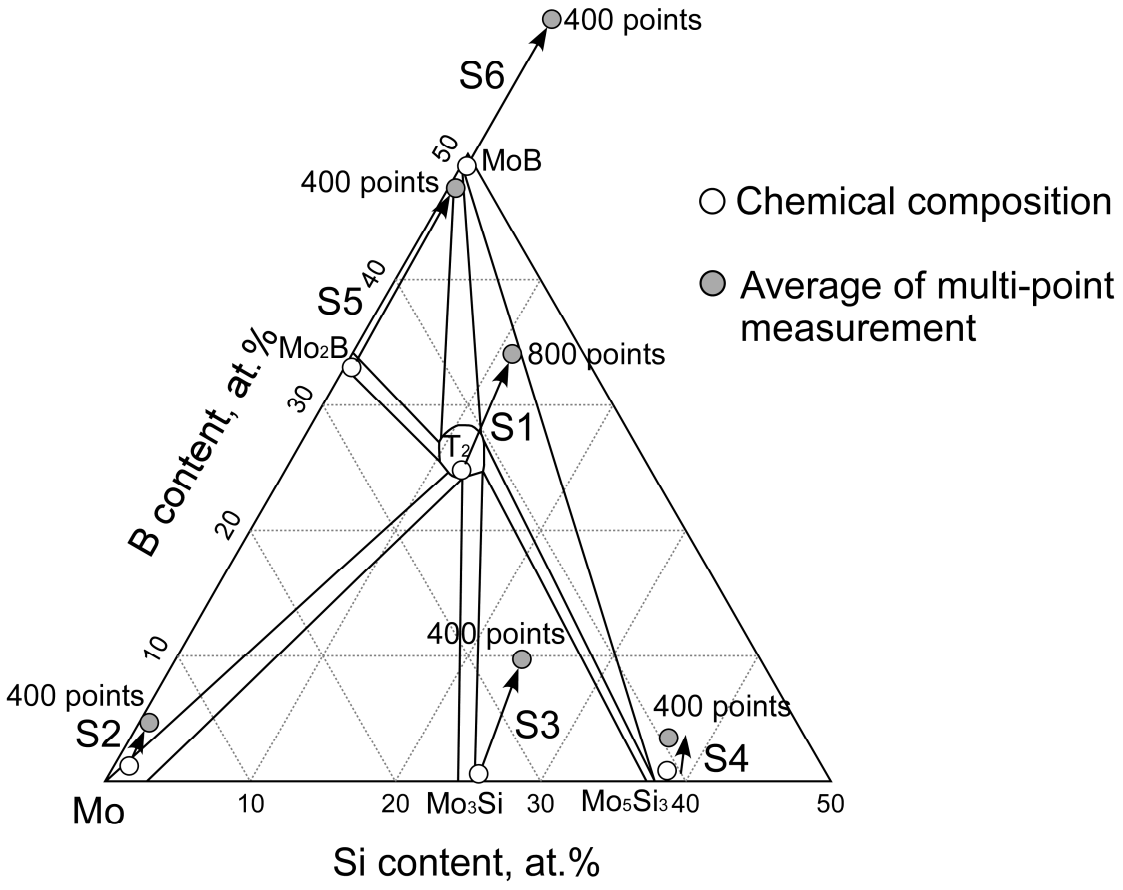


**Fig. 2.9 Comparison between chemical compositions and averages of multi-point measurements by EPMA for S1-S6 alloys.**

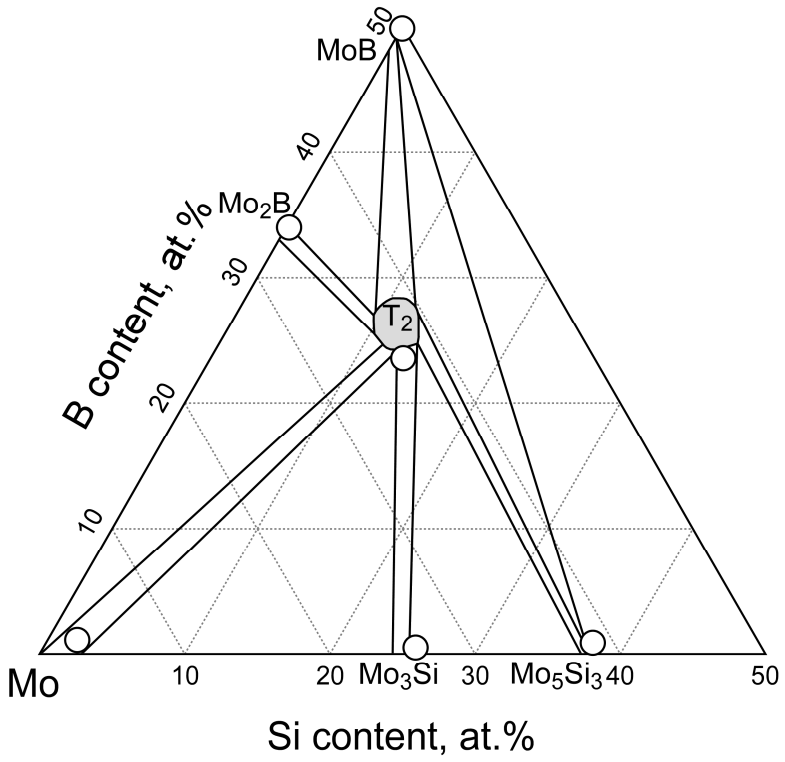


**Fig. 2.10 Compositions of constituent phases in Mo-rich portion of Mo-Si-B ternary system analyzed by EPMA with the standard samples prepared in this study.**

# CHAPTER 3

# Experimental Study on Mo-$T_2$ and Mo-$Mo_3Si$-$T_2$ Eutectic Reactions in the Mo-rich Portion of the Mo-Si-B Ternary System

## 3.1 Introduction

Recently, Mo-Si-B ternary alloys have attracted great attention due to their favorable properties in high-temperature structural application. The main properties are high thermal stability and oxidation resistance at ultra-high temperature [1, 2]. There exist various silicide and boride phases and a ternary compound phase of $Mo_5SiB_2$ ($T_2$) in the Mo-Si-B ternary system, which have melting points over 2000 °C [3]. However, the high melting temperature points generate a trade-off problem, that is make materials processing such as melting and casting, forging, powder sintering and etc. extremely difficult compared with that for steels and titanium alloys. Concerning melting and casting, to utilize eutectic reactions is one of the ways to bypass the difficulty with lowering process temperature.

Liquidus projection gives solidification routes and reaction points during the

solidification of materials. The liquidus projection of the Mo-Si-B system was first suggested by Nunes et al. in 2000 with microstructure examination [4]. After their work, it was reconsidered in terms of the solidus temperatures by Katrych et al. in 2002 by Pirani-Athertum melting point data, differential thermal analysis (DTA) [5]. In 2005, a liquidus projection was further considered thermodynamically by Yang et al. [6], referring mainly to experimental data in the liquidus projections reported by Nunes et al. [4] and Katrych et al. [5]. In their literature, the existence of some eutectic reactions, for example, with Mo solid solution ($Mo_{ss}$) and $T_2$, with $Mo_{ss}$, $Mo_3Si$ and $T_2$ and with $Mo_5Si_3$ ($T_1$) and $T_2$ was pointed out in the Mo-rich portion of the Mo-Si-B system. The eutectic reaction with $Mo_{ss}$, $Mo_3Si$ and $T_2$ is invariant since the three phases are formed from a liquid phase in the ternary system. On the other hand, those with $Mo_{ss}$ and $T_2$ and with $T_1$ and $T_2$ are mono-variant, following a subsequent solidification step since the mono-variant reactions equilibrate with a liquidus phase. These eutectic reactions would be useful to lower the melting and casting temperatures of Mo-Si-B ternary alloys. However, there is still room for argument on the compositional points of the eutectic reactions.

In this chapter, the compositional points of the eutectic reactions are experimentally investigated mainly using field-emission (FE) gun-type electron probe

micro-analysis (EPMA) calibrated in the preceding chapter. Solidification routes in the Mo-rich portion of the Mo-Si-B ternary system will be discussed based on obtained results.

### 3.2 Experimental Procedures

The liquidus projections reported by Nunes et al. [4], Katrych et al. [5] and Yang et al. [6] are superimposed in Fig. 3.1 to clarify the differences between them. The compositions of alloys examined in this study were plotted on this figure. The nominal compositions of the examined alloys also are shown in Table 3.1. The button ingots of Mo-Si-B alloys in the weight of approx. 20 g were prepared by a conventional arc-melting technique from pure Mo (99.9 wt.%), Si (99.9999 wt.%) and B (99.95 wt.%) with a water-cooled copper crucible under an Ar atmosphere. Prior to each melting, the furnace was evacuated and filled with high-purity Ar gas several times. A commercially pure Ti ingot was preliminary melted before every melting to remove residual $O_2$ and $N_2$ gases as possible. Each alloy ingot was flipped after melting and re-melted more than 5 times to ensure compositional homogeneity as possible. There was no large difference in alloy weight between before and after melting. The specimens were taken from the center of the ingots and prepared for chemical analysis,

X-ray diffractometry (XRD) and scanning electron microscopy (SEM). The atomic ratios of Mo, Si and B in the as-cast alloys were analyzed by inductively coupled plasma (ICP) - the optical emission spectrometry (OES) method as reported by Danzaki et al. [8]. The compositions chemically-analyzed are also in Table 3.1. Impurity levels were measured by ICP-OES method for Ti, Cu and W. The constituent phases of as-cast specimens were identified by XRD (Bruker D-8 Advance) using the Cu-Kα radiation and their microstructures were observed by SEM (JEOL JSM-6500F) perated at 15kV with back scattered electron (BSE) images. The quantitative composition analysis of primary and eutectic phases was performed by FE-EPMA (JEOL JXA-8530F) operated at 15 kV and 20 nA. The calibration method for the quantitative analysis was modified by the statistical treatment same as that adopted in Chapter 2 using originally tailored standard samples. Especially, Alloy 1 and 11 were employed as standard samples for the analysis of eutectic phases. Layered dispersion element (LDE) - 2H, Thallium acid phthalate (TAP) and Pentaerythritol (PET) - H were employed as dispersive crystals. Microstructure observation and semi-quantitative compositon analysis were also carried out using a transmission electron microscopy (TEM) (JEOL JEM3010) operated at 300 kV equipped with an energy dispersive X-ray spectroscope (EDX) (EDAX Genesis).

## 3.3 Results

### 3.3.1 $Mo_{ss}$ Primary Phase Region

Fig. 3.2 shows the SEM-BSE images of the as-cast microstructures of Alloys 1 to 4. Alloy 1 (Fig. 3.2(a)) was almost entirely composed of two types of eutectic phases: one had a two-phase eutectic microstructure (super-fine) and the other a three-phase fine microstructure between the super-fine eutectic areas. A bright phase of approx. 20 μm in size was occasionally observed as primary phase in Alloy 1. A XRD profile obtained from Alloy 1 (Fig. 3.3) indicated the existence of $Mo_{ss}$, $Mo_3Si$ and $T_2$ phases in the alloy. FE-EPMA showed that the primary phase mostly consisted of $Mo_{ss}$ and contained a small amount of Si and B. From these results, it was found that the primary phase of Alloy 1 was $Mo_{ss}$, and suggested that the alloy composition was very close to a eutectic point. The microstructures of Alloys 2 to 4 displayed a bright and dendritic primary phase as shown in Figs. 3.2(b) and (d). Alloys 2 and 3 had a gray, elongated second phase as shown in Figs. 3.2(b) and (c). They also had super-fine two-phase and fine three-phase eutectic areas between the primary and secondary phase areas. XRD profiles obtained from Alloys 2 to 4 (Fig. 3.3) showed the existence of $Mo_{ss}$, $Mo_2B$, $Mo_3Si$ and $T_2$ phases in Alloys 2 and 3 and $Mo_{ss}$, $Mo_3Si$ and $T_2$ phases in Alloy 4. The obtained results including FE-EPMA ones indicated that the primary phase of Alloys 2

to 4 was also $Mo_{ss}$ and the secondary phase of Alloys 2 and 3 was $Mo_2B$. Therefore, it was determined that Alloys 1 to 4 were in the Moss primary phase region of a Mo-Si-B liquidus projection.

As mentioned above, Alloy 1 was almost entirely composed of two types of eutectic phases. In order to determine constituent phases in the eutectic areas, microstructure characterization was examined by TEM-EDX for Alloy 1. Fig. 3.4 shows the TEM-EDX results of a fine three-phase area. The crystal structure determination according to the diffraction patterns shown in Figs. 3.4(b) to (c) suggested the existence of $Mo_{ss}$, $Mo_3Si$ and $T_2$ in the observed area shown in Fig. 3.4(a). The X-ray intensity profiles for the constituent phases were analyzed by EDX; there was a moderate B-Kα peak but a slight Si-Kα peak for $Mo_{ss}$ as seen in Fig. 3.4(e), a strong B-Kα peak compared to the Mo-Kα peak and a moderate Si peak for $T_2$ (Fig. 3.4(f)), and moderate B-Kα and Si-Kα peaks for $Mo_3Si$ (Fig. 3.4(g)). These results indicated that the three-phase areas seen in the SEM micrograph shown in Fig. 3.2(a) were composed of $Mo_{ss}$ (bright phase), $Mo_3Si$ (grey phase) and $T_2$ (dark phase). The two-phase eutectic areas were also characterized by TEM-EDX, and the results are shown in Fig. 3.5. The characteristic X-ray intensity profiles of Figs. 3.5(b) and (c) indicate that the matrix is $T_2$ and the dispersions are $Mo_{ss}$. The composition of the two-phase eutectic area in Alloy

1 was selectively analyzed by the calibrated FE-EPMA, and determined to be Mo-7.9Si-15.4B. That in Alloys 2 were also selectively analyzed by the calibrated FE-EPMA, and the obtained results were summarized in Table 3.2.

### 3.3.2 $Mo_2B$ Primary Phase Region

Fig. 3.6 shows the SEM-BSE images of the as-cast microstructures of Alloys 5 to 7. The microstructures of Alloy 5 to 7 showed a gray primary phase and bright second phase formed along primary. They also had the $Mo_{ss}$-$T_2$ two-phase and $Mo_{ss}$-$Mo_3Si$-$T_2$ three-phase eutectic areas between the primary and secondary phase areas, defined through Alloy 1. XRD profiles obtained from Alloys 6 to 7 (Fig. 3.7) showed the existence of $Mo_{ss}$, $Mo_2B$, $Mo_3Si$ and $T_2$ phases in Alloys 6 and 7. The obtained results including FE-EPMA ones indicated that the primary phase of Alloys 5 to 7 was also $Mo_2B$ and the secondary phase of Alloys 5 and 7 was $Mo_{ss}$. Therefore, it was determined that Alloys 5 to 7 were in the $Mo_2B$ primary phase region of a Mo-Si-B liquidus projection. The composition of the two-phase eutectic area in Alloy 6 was selectively analyzed by the calibrated FE-EPMA, and determined to be Mo-8.2Si-14.4B.

### 3.3.3 $T_2$ Primary Phase Region

Fig. 3.8 shows the SEM-BSE images of the as-cast microstructures of Alloys 8 to

11. The microstructures of Alloy 8 to 11 showed a dark dendrite primary phase and no second phase as those of $Mo_{ss}$ and $Mo_2B$ primary phase region in Alloys 8 to 10, but a gray dendrite primary phase and a dark second phase. There exist the $Mo_{ss}$-$T_2$ two-phase and $Mo_{ss}$-$Mo_3Si$-$T_2$ three-phase eutectic areas surrounding primary $T_2$ in Alloy 8 to 10. However, other fine two-phase was mainly observed in Alloy 11. XRD profiles obtained from Alloys 8 to 11 (Fig. 3.9) showed the existence of $Mo_{ss}$, $Mo_3Si$ and $T_2$ phases in Alloys 8 to 10 and $Mo_5Si_3$, $T_2$ and $Mo_3Si$ in Alloy 11. The XRD and FE-EPMA results indicated that the primary phase of Alloys 8 to 11 was $T_2$ and the secondary phase of Alloy 11 was $Mo_5Si_3$. Therefore, it was determined that Alloys 8 to 11 were in the $T_2$ primary phase region of a Mo-Si-B liquidus projection. The composition of the two-phase eutectic area in Alloy 6 was selectively analyzed by the calibrated FE-EPMA, and determined to be Mo-8.8Si-16.8B.

As mentioned above, Alloy 11 was mainly composed of fine two-phase eutectic phase. In order to determine constituent phases in the eutectic areas, microstructure characterization was examined by TEM for Alloy 11. Fig. 3.10 shows the TEM results of a fine two-phase area. The crystal structure determination according to the diffraction patterns shown in Figs. 3.10(b) to (c) suggested the existence of $Mo_3Si$ and $T_2$ in the observed area shown in Fig. 3.10(a). These results indicated that the two-phase areas

seen in the SEM micrograph shown in Fig. 3.8(a) were composed of $Mo_3Si$ (bright phase) and $T_2$ (gray phase).

### 3.3.4 Alloy 12

Fig. 3.11 shows the SEM-BSE images of the as-cast microstructures of Alloy 12. In Alloy 12, fine two- and three-phases was entirely observed with no primary phase. XRD profiles obtained from Alloy 12 (Fig. 3.12) showed the existence of $Mo_{ss}$, $Mo_3Si$ and $T_2$ phases in Alloy 12. As mentioned above, Alloy 12 was composed of fine two- and three-phase eutectic phase. In order to determine constituent phases in the eutectic areas, microstructure characterization was examined by TEM for Alloy 12. Fig. 3.13 shows the TEM results of a fine three-phase area. The crystal structure determination according to the diffraction patterns shown in Figs. 3.13(b) to (c) suggested the existence of $Mo_3Si$ and $T_2$ in the observed area shown in Fig. 3.13(a). These results indicated that the two-phase areas seen in the SEM micrograph shown in Fig. 3.11(a) were composed of $Mo_{ss}$ (bright phase), $Mo_3Si$ (gray phase) and $T_2$ (dark phase). The two-phase eutectic areas were also characterized by TEM, and the results are shown in Fig. 3.14. The diffraction patterns of Figs. 3.14(b) and (c) indicate that the matrix is $Mo_3Si$ and the dispersions are $T_2$. The compositions of the two- and three-phase eutectic areas in Alloy 12 were selectively analyzed by the calibrated FE-EPMA, and

determined to be Mo-20.6Si-6.7B and Mo-16.3Si-6.7B, respectively.

### 3.4 Discussion

Primary phase formation observed in this study are shown in Fig. 3.15 with the Mo-Si-B ternary phase diagram and the liquidus projection reported by Nunes et al. [4], Katrych et al. [5] and Yang et al. [6]. It was considered that the results obtained in this study are in good agreement of that of Yang et al. [6] by thermodynamic calculation. The differences among three liquidus projections were focused in this study. In terms of primary regions, the three liquidus projections have differences, especially between that of yang et al. [6] determined thermodynamically and others (see Fig. 3.15). In fact, however, there has been no issue on the differences of the primary regions in the liquidus projection works. In the work by Yang et al. [6], actually, it was described that the determined primary regions were in good agreement of those of Nunes et al. [4]. The overlap of the three liquidus projections with isothermal phase diagram of Mo-Si-B ternary system at 1600 $^{\circ}$C [7] is shown in Fig. 3.16. As seen in enlargement for the $Mo_{ss}$-$T_2$ eutectic point area, there is an obvious difference between the three liquidus projections. The $Mo_{ss}$-$T_2$ eutectic points of Katrych et al. [5] and Nunes et al. [4] are included in $Mo_{ss}$-$T_2$ two-phase region of the phase diagram, while that of Yang et al. [6]

expands to $Mo_{ss}$-$Mo_3Si$-$T_2$ three-phase region. This would be a big difference in the $Mo_{ss}$-$T_2$ two-phase or $Mo_{ss}$-$Mo_3Si$-$T_2$ three-phase processing after heat treatment at 1600 °C. From the result of this study, it was concluded that the $Mo_{ss}$-$T_2$ two-phase region in the Mo-Si-B phase diagram is roughly divided into three primary regions by the liquidus projection; $Mo_{ss}$, $Mo_2B$ and $T_2$. Thus, the primary phase formation of $Mo_{ss}$, $Mo_2B$ and $T_2$ can not be avoided in solidification process even if the alloy composition is aimed to that of $Mo_{ss}$-$T_2$ two-phase region. On the other hand, after heat treatment at 1600 °C, the $Mo_{ss}$ and $T_2$ primary phases would remain since they are equilibrium phases in the $Mo_{ss}$-$T_2$ two-phase region. Primary $Mo_2B$, a non-equilibrium phase in $Mo_{ss}$-$T_2$ region, would decompose. This could lead to the fine distribution of $Mo_{ss}$.

Considering the solidification routes of Alloy 1, 11 and 12 in eutectic phase formation, the solidification steps of Alloy 1 were found to be $Mo_{ss}$ (primary) $\rightarrow$ $Mo_{ss}$ + $T_2$ eutectic $\rightarrow$ $Mo_{ss}$ + $T_2$ + $Mo_3Si$. The $Mo_{ss}$-$Mo_3Si$-$T_2$ point in the liquidus projections of Nunes et al. [4] and Yang et al. [6] is triple junction where L+$Mo_{ss}$$\rightarrow$$Mo_3Si$ peritectic, $Mo_{ss}$-$T_2$ and $Mo_3Si$-$T_2$ eutectic valleys meet one another. In the case of Alloy 1, the formation of the $Mo_{ss}$-$Mo_3Si$-$T_2$ is attributed by L + $Mo_{ss}$ $\rightarrow$ $Mo_3Si$ + $T_2$ peritectic reaction.

The same thing as that of Alloy 12 is that the final product followed by the

formation of the superfine two-phase eutectic phase is the $Mo_{ss}$-$Mo_3Si$-$T_2$ phase. However, it is morphologically different between Alloy 1 and 12. This is attributed to the different formation path of the $Mo_{ss}$-$Mo_3Si$-$T_2$ phase. As shown in enlargement of Fig. 3.16, there is the extremely short eutectic valley of the $Mo_3Si$-$T_2$ in the liquidus projection of Yang et al. [6], indicating that the $Mo_{ss}$-$Mo_3Si$-$T_2$ point is close to the $Mo_3Si$-$T_2$ point. Since the chemical composition of Alloy 12 is slightly deviated from the weighing composition to Si-rich, the formation of the $Mo_3Si$-$T_2$ eutectic would be the preferential reaction. And then, the $Mo_3Si + T_2 + L \rightarrow Mo_{ss}$ reaction would occur at the $Mo_{ss}$-$Mo_3Si$-$T_2$ point.

In the case of Alloy 11, the primary phase appears to be $T_2$, indicating that the alloy composition would be slightly deviated to the $T_2$ primary region. After primary $T_2$ was solidified as dendritic form, $Mo_5Si_3$ would be formed between primary $T_2$ dendrites owing to rapid change of the composition to Si-rich, indicating that the $T_2$ and $Mo_5Si_3$ were formed like $T_2$-$Mo_5Si_3$ monovariant eutectic phase. Thus, this obviously indicates the microstructure formation near a eutectic valley. The microstructure formation observed for Alloy 11 strongly supports that the results of this study are in good agreement with that of Yang et al. [6]. As shown in Fig. 3.16, the three liquidus projections also have a visible difference in terms of the $Mo_5Si_3$-$T_2$ eutectic valley. The

$Mo_3Si$-$T_2$ eutectic point followed by $Mo_5Si_3$-$T_2$ eutectic valley in the liquidus projection of Nunes et al. [4] is much B-poorer than that of Yang et al. [6]. As described in Chapter 1, the alloy system including $Mo_5Si_3$ has been considered for oxidation resistant coating because of its excellent oxidation resistance. Microstructure formation of the alloy system involving $Mo_5Si_3$ suggested so far should be reconsidered by the solidification route involving $Mo_5Si_3$ shown by Yang et al. [6].

The $Mo_{ss}$-$T_2$ and $Mo_{ss}$-$Mo_3Si$-$T_2$ eutectic in Alloy 1, 2, 3 and 4 and two eutectic phases involving $Mo_3Si$ in Alloy 12 were analyzed for compositional determination of each eutectic point. The results for the quantitative analyses are plotted in Fig. 3.17 and also shown in Table 3.2. The compositions of each phase are quite different from those of Yang [6]. In the case of Alloy 2 and 3, the compositions of $Mo_{ss}$-$T_2$ appear to correspond rather to that of the $Mo_{ss}$-$T_2$ eutectic point in the liquidus projection by Nunes et al. [4]. All the determined compositions for $Mo_{ss}$-$T_2$ eutectic phases in this study differ from that of one another. In the case of Alloy 2, 3 and 4 including primary, the same thing is that the determined $Mo_{ss}$-$T_2$ eutectic points are off the corresponding primary regions. For example, the $Mo_{ss}$-$T_2$ eutectic point in Alloy 2 with primary $Mo_{ss}$ is included in $Mo_2B$ primary region. This would be attributed to super-cooling during arc-melting. Therefore, it is considered that the change of the $Mo_{ss}$-$T_2$ eutectic points

depends on cooling rate and formation of primary phase. The composition of the $Mo_{ss}$-$T_2$ eutectic phase in Alloy 1 with few primary particles is located in $Mo_{ss}$-$Mo_2B$ eutectic valley. However, it should be noted that they were included in the $Mo_{ss}$-$T_2$ two-phase region of Mo-Si-B ternary phase diagram at 1600 °C. In the case of the $Mo_{ss}$-$Mo_3Si$-$T_2$ eutectic phase, the determined composition was included in the $Mo_{ss}$ primary region and the determined $Mo_3Si$-$T_2$ point was somewhat shifted toward Si-rich from the alloy composition near the $Mo_5Si_3$-$T_2$ eutectic valley. From the compositional determination for each eutectic phase in this study, all the determined eutectic points are off those of Yang et al. [6]. Therefore, it was assumed that practical solidification in the Mo-Si-B ternary system follows different routes with those of the liquidus projection. The compositional solidification route from the $Mo_{ss}$-$T_2$ and $Mo_3Si$-$T_2$ to the $Mo_{ss}$-$Mo_3Si$-$T_2$ eutectic reaction is suggested from the EPMA results as seen in Fig. 3.16 (c).

### 3.5 Conclusions

In this study, the phase formation behavior of the Mo-Si-B system during solidification was experimentally examined around the $Mo_{ss}$-$T_2$ and Mo-$Mo_3Si$-$T_2$ eutectic points in the Mo-Si-B liquidus projection proposed by Yang and Chang [6]. The

conclusions are as follows.

(1) The primary phase formation observed in this study was in good agreement with that of the liquidus projection thermodynamically obtained by Yang et al. [6]. The liquidus projection of Yang et al. [6] was quite different with those of Nunes et al. [4] and Katrych et al. [5] in terms of near the $Mo_{ss}$-$T_2$ eutectic point and the eutectic valley involving $Mo_5Si_3$ mainly considered for Mo-Si-B alloy process.

(2) Alloy 1 (Mo-9.5Si-14.2B) with a composition closest to the $Mo_{ss}$-$T_2$ point had two microstructural areas, $Mo_{ss}$-$T_2$ superfine eutectic and $Mo_{ss}$-$T_2$-$Mo_3Si$ fine three-phase areas. Alloy 12 aimed to that of the $Mo_{ss}$-$Mo_3Si$-$T_2$ eutectic point also showed the development of fine $Mo_3Si$-$T_2$ eutectic phase and the existence of $Mo_{ss}$-$Mo_3Si$-$T_2$.

(3) Utilizing the microstructural and compositional homogeneity of Alloy 1 and 5, the quantitative analysis results obtained by EPMA were well calibrated, with particular interest in the results for B.

(4) From the existence of the $Mo_5Si_3$-$T_2$ phase by the monovariant eutectic reaction in the microstructure of Alloy 11, it was reconfirmed that the result of this study was in a good agreement of the liquidus projection by Yang et al. [6].

(5) From the EPMA results, the compositional determined $Mo_{ss}$-$T_2$, $Mo_3Si$-$T_2$ and

$Mo_{ss}$-$Mo_3Si$-$T_2$ eutectic points were suggested in this study. They were different from those of the liquidus projection of Yang et al. [6]. Thus, it was realized that each reaction point in practical solidification differs from that of the liquidus projection.

**References**

[1] Ito K, Ihara K, Tanaka K, Fujikura M, Yamaguchi M. Intermetallics 2001; **9**:591-602.

[2] Yoshimi K, Nakatani S, Suda T, Hanada S, Habazaki H. Intermetallics 2002;**10**:407-414.

[3] Mitra R. Intl Mater Rev 2006;**51**:13-64.

[4] Nunes CA, Sakidja R, Dong Z, Perepezko JH. Intermetallics 2000;**8:**327-337.

[5] Katrych S, Grytsiv A, Bondar A, Rogl P, Velikanova T, Bohn M. J Alloy Compd 2002;347:94-100.

[6] Yang Y, Chang YA. Intermetallics 2005;**13:**121-128.

[7] Kim ST, Perepezko JH. J Phase Equilib Diffus 2006;**27:**605-613.

[8] Danzaki Y, Wagatsuma K, Syoji T, Yoshimi K. Fresenius J Anal Chem 2001;**369:**184-186.

**Table 3.1 Nominal and chemical compositions of the alloys.**

| Alloy | Nominal composition | | Chemical composition | | | | |
|---|---|---|---|---|---|---|---|
| | Si (at%) | B (at%) | Si (at%) | B (at%) | Ti (ppm) | Cu (ppm) | W (ppm) |
| 1 | 9.5 | 14.2 | 9.3 | 14.0 | 15 | <10 | <200 |
| 2 | 6.6 | 13.2 | 6.5 | 13.0 | 60 | <20 | 100 |
| 3 | 7.3 | 14.6 | 7.7 | 14.8 | <10 | <10 | <100 |
| 4 | 13 | 10 | 13.2 | 10.3 | <10 | <10 | <100 |
| 5 | 8 | 16 | 8.1 | 16.2 | <10 | <10 | <100 |
| 6 | 8.7 | 17.4 | 8.5 | 17.2 | <10 | <15 | <100 |
| 7 | 5.7 | 20.4 | 6.0 | 20.7 | <10 | <10 | <100 |
| 8 | 9.7 | 19.4 | 9.8 | 19.8 | <10 | <15 | <100 |
| 9 | 10.5 | 14.2 | 10.8 | 14.5 | <10 | <10 | <100 |
| 10 | 15 | 11 | 15.1 | 11.0 | <10 | <10 | <100 |
| 11 | 21.8 | 8.5 | - | - | - | - | - |
| 12 | 19.1 | 6.5 | 19.8 | 6.7 | <10 | <10 | <100 |

**Table 3.2 Compositions of each eutectic phase determined by EPMA.**

| Phase | Alloy No. | Mo (at%) | Si (at%) | B (at%) |
|---|---|---|---|---|
| $Mo_{ss}$-$T_2$ | 1 | 76.7 | 7.9 | 15.4 |
| | 2 | 75.1 | 8.8 | 16.1 |
| | 6 | 77.4 | 8.2 | 14.4 |
| | 9 | 74.4 | 8.8 | 16.8 |
| $Mo_{ss}$-$Mo_3Si$-$T_2$ | 12 | 77.0 | 16.3 | 6.7 |
| $Mo_3Si$-$T_2$ | | 72.8 | 20.6 | 6.6 |

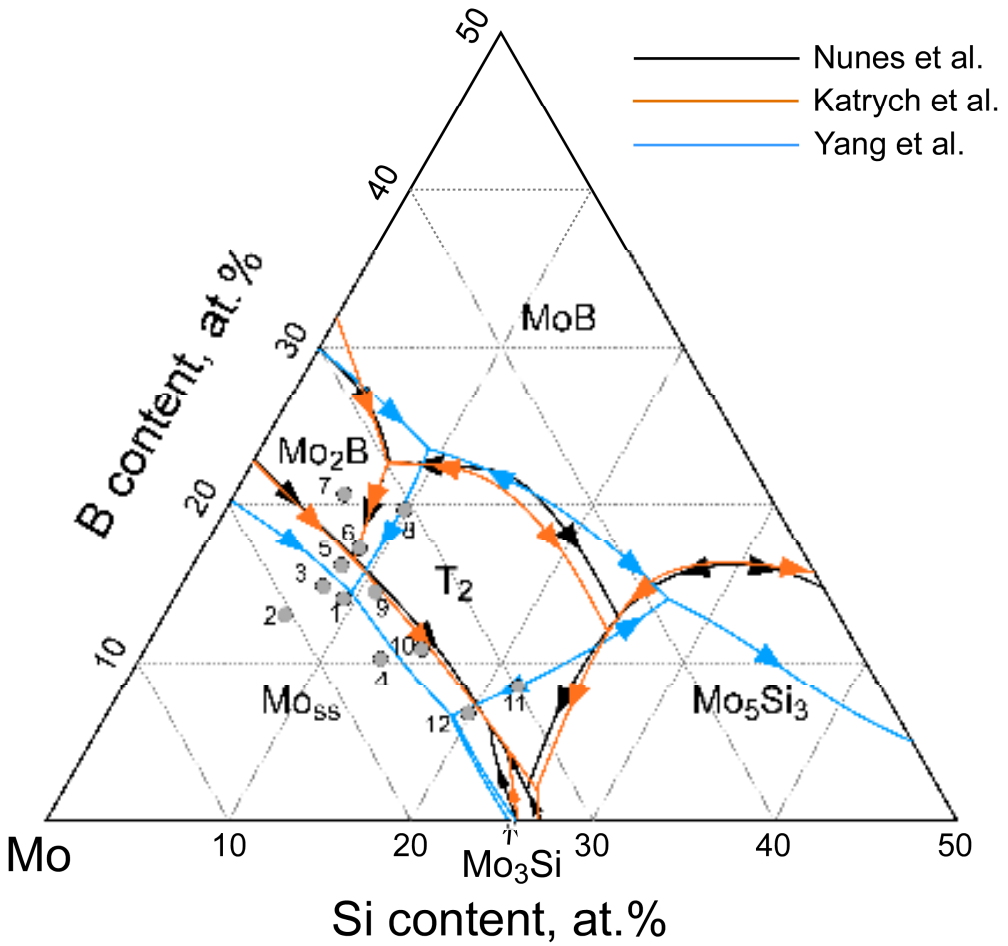


**Fig. 3.1 Chemical composition of the examined alloys plotted in liquidus projection [4-6].**

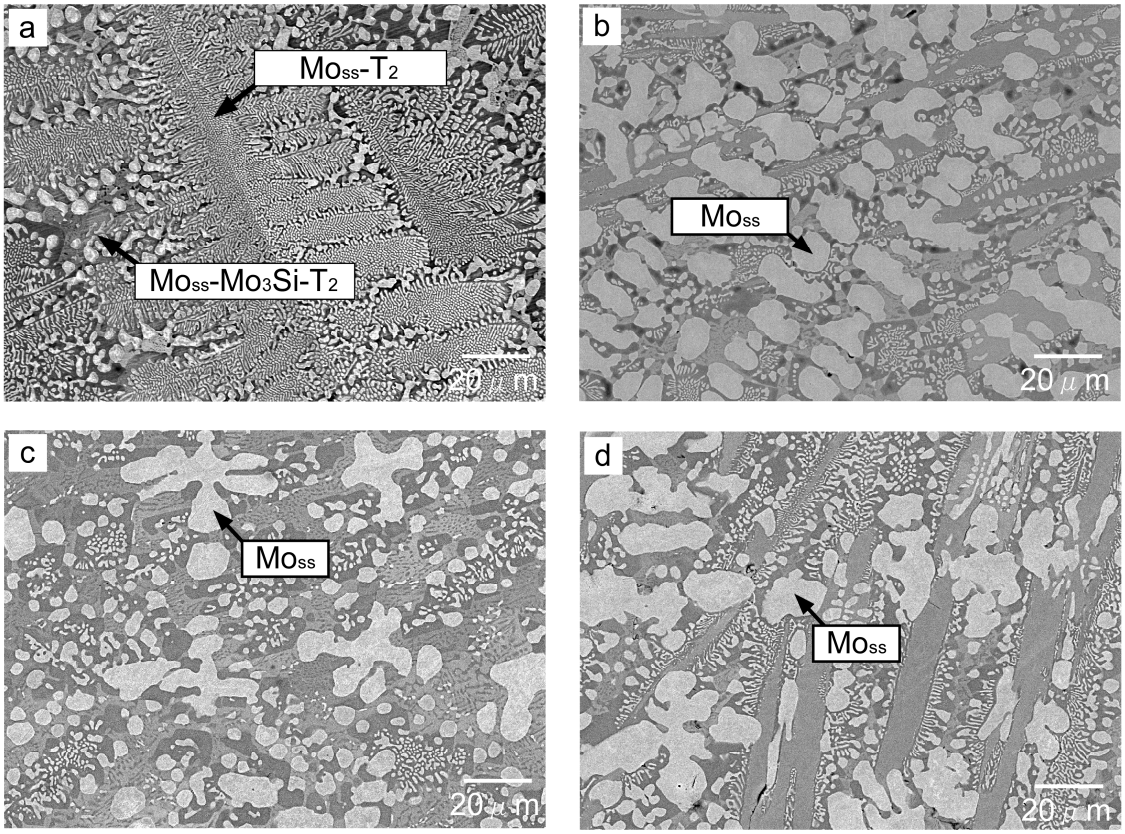


**Fig. 3.2 As-cast microstructures of Alloy (a) 1, (b) 2, (c) 3 and (d) 4.**

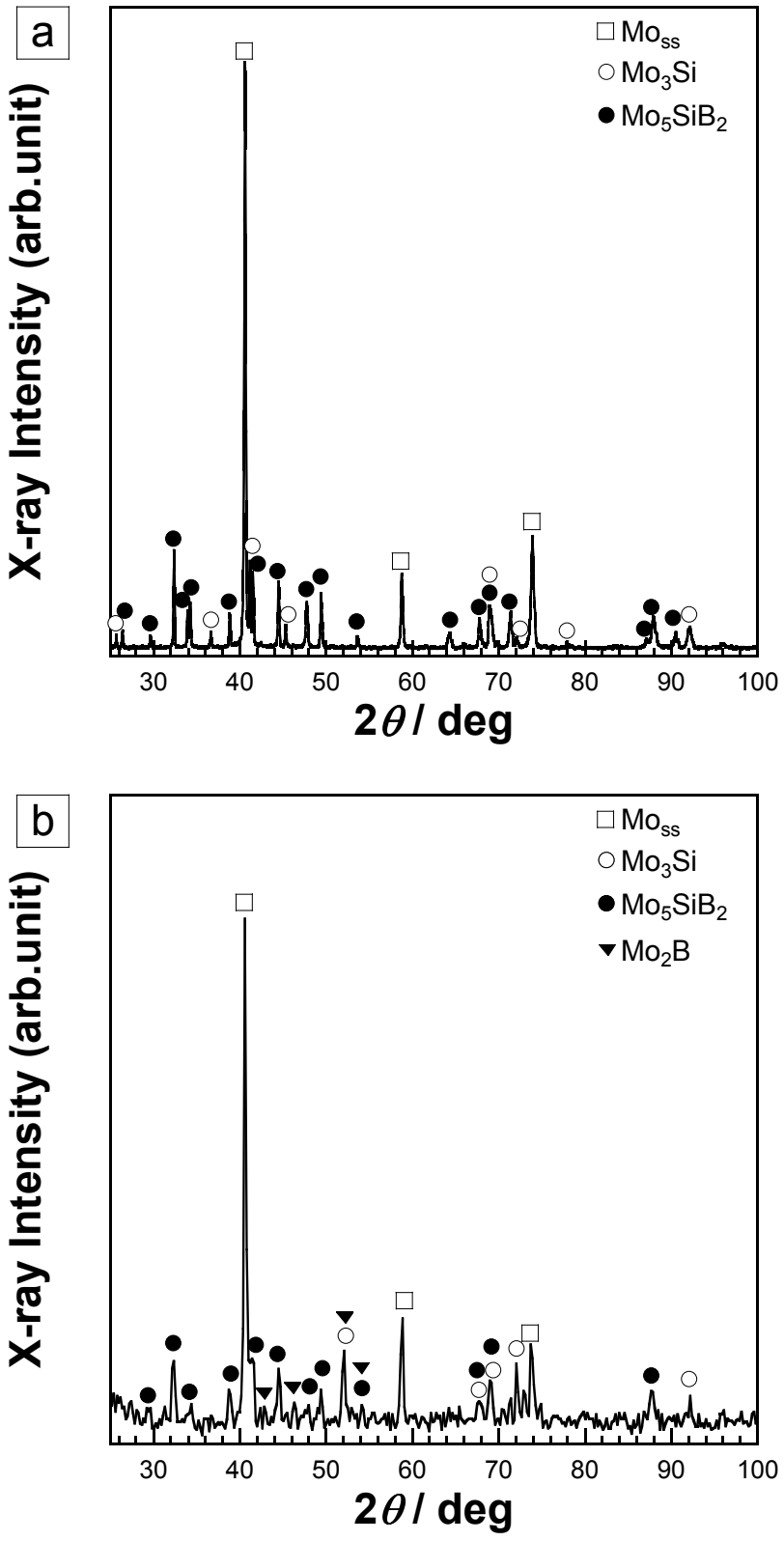


**Fig. 3.3 XRD diffraction pattern of Alloys (a) 1 and (b) 2.**

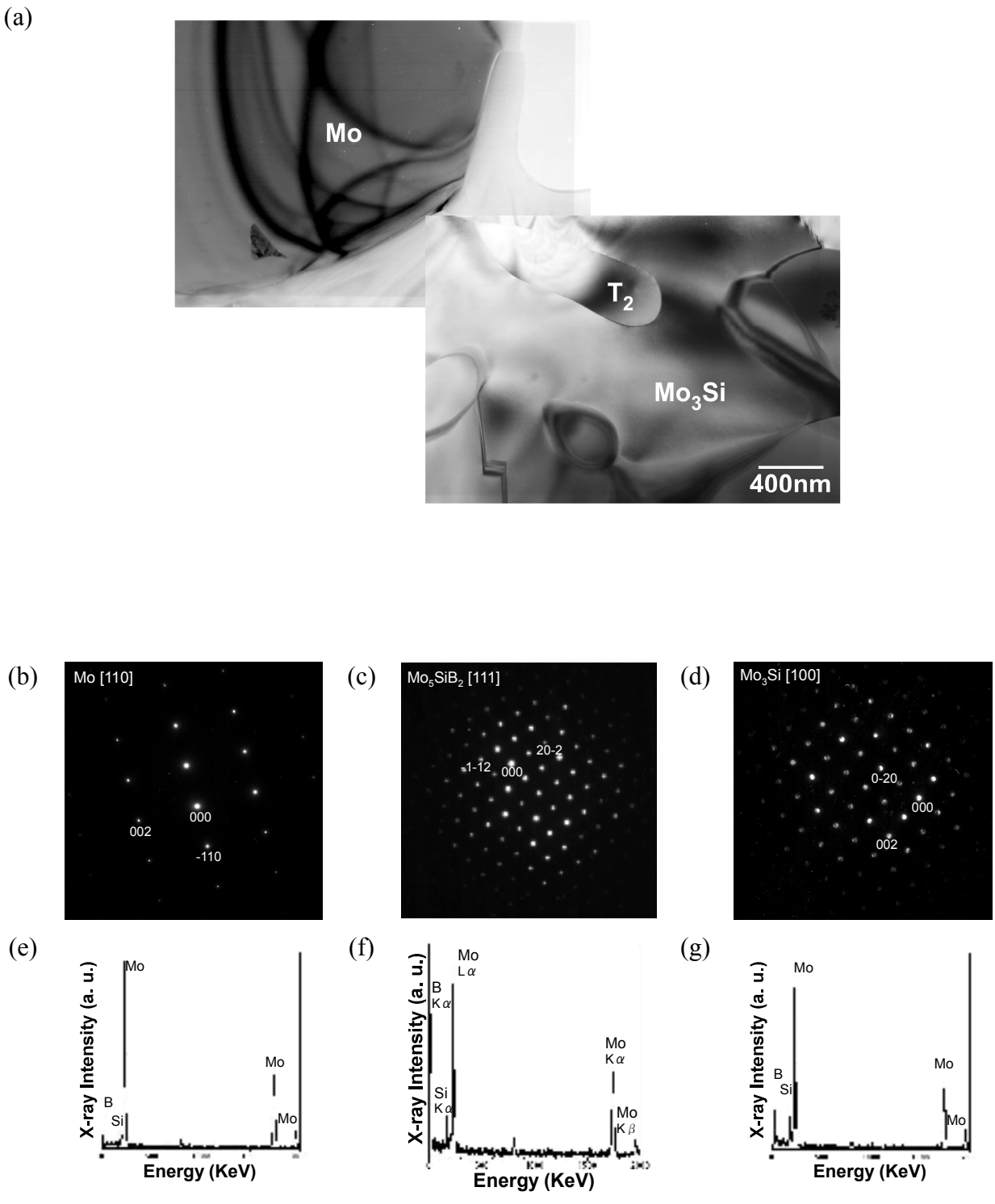


**Fig. 3.4 Bright field TEM micrograph for $Mo_{ss}$-$Mo_3Si$-$T_2$ phase in Alloy 1; (b)-(d) Diffraction patterns, and (e)-(f) characteristic X-ray intensity profiles by EDX for the three phases, respectively.**

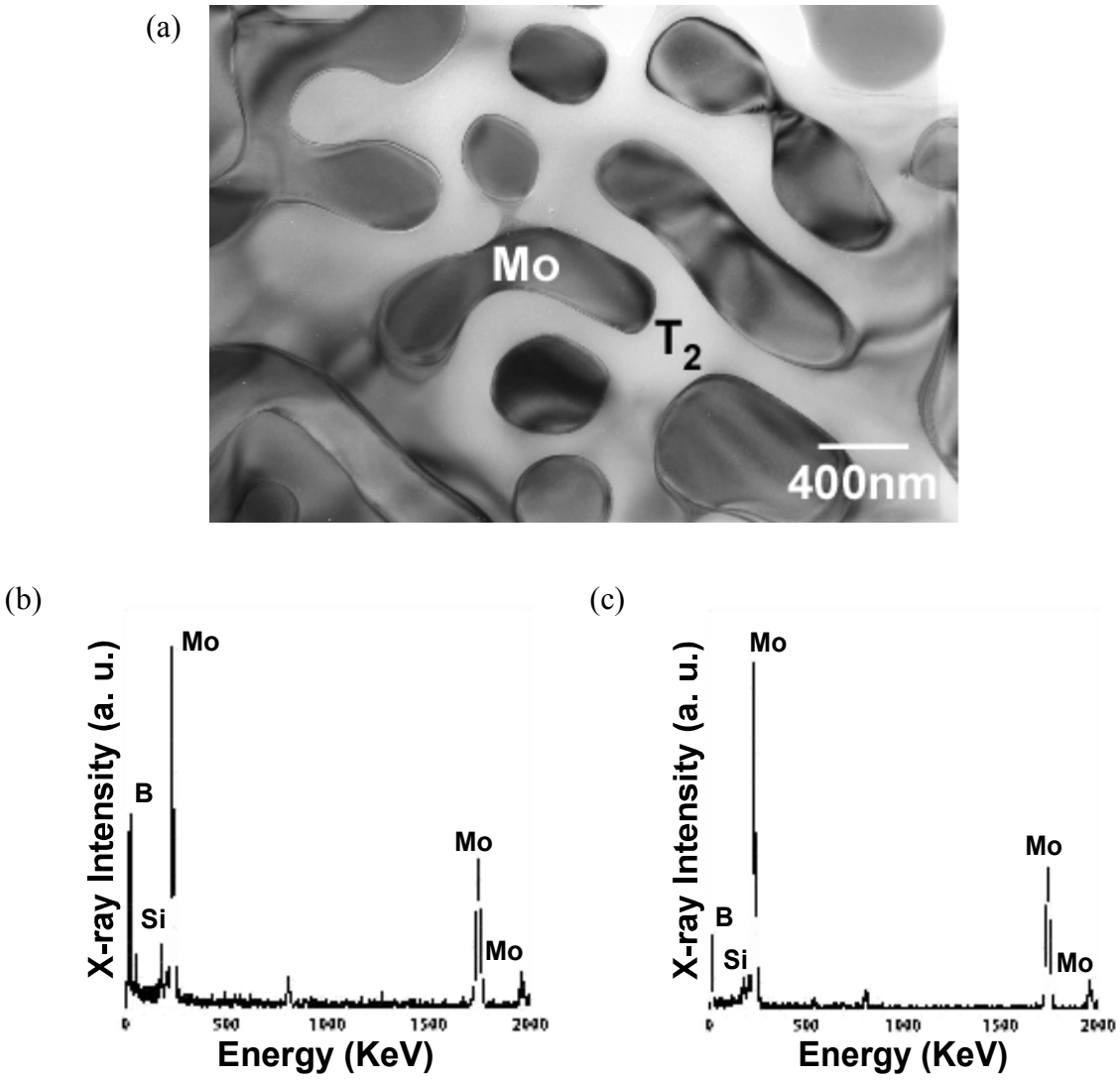


**Fig. 3.5 (a) Bright field TEM micrograph for Mo-$T_2$ eutectic phase in Alloy 1; (b), (c) characteristic X-ray intensity profiles for Mo and $T_2$, respectively.**

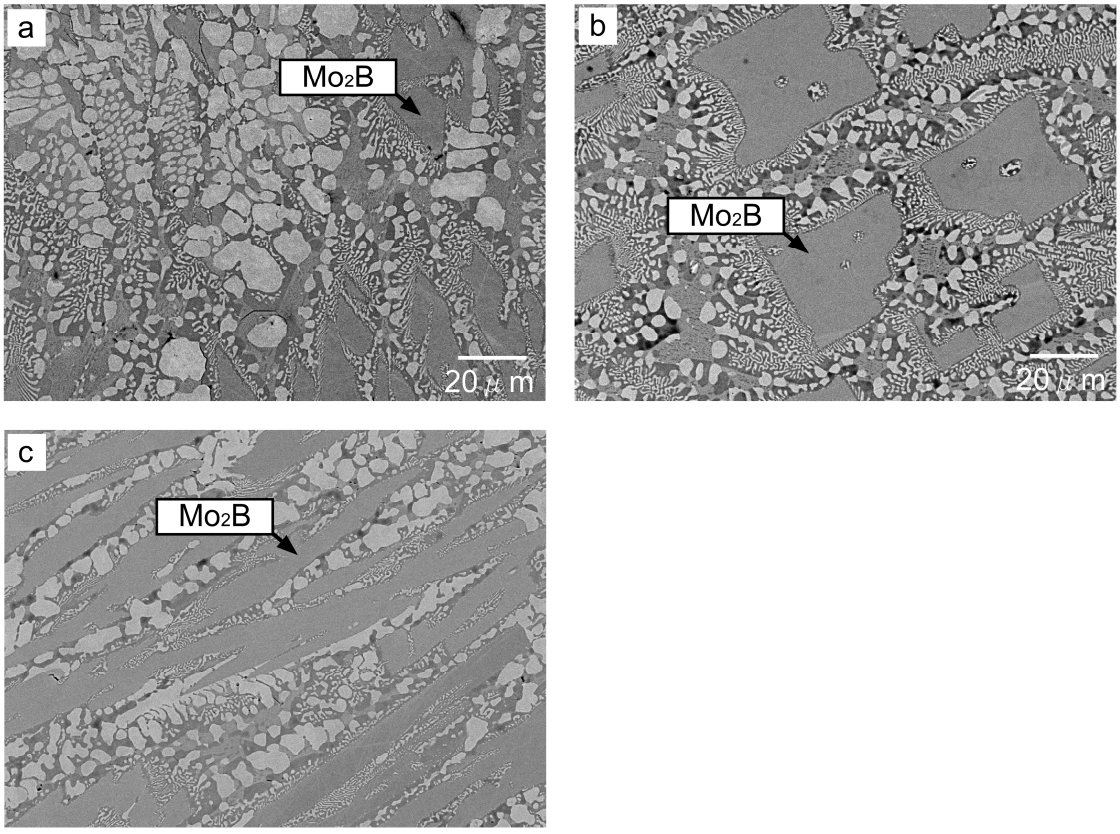


**Fig. 3.6 As-cast microstructures of Alloy (a) 5, (b) 6 and (c) 7.**

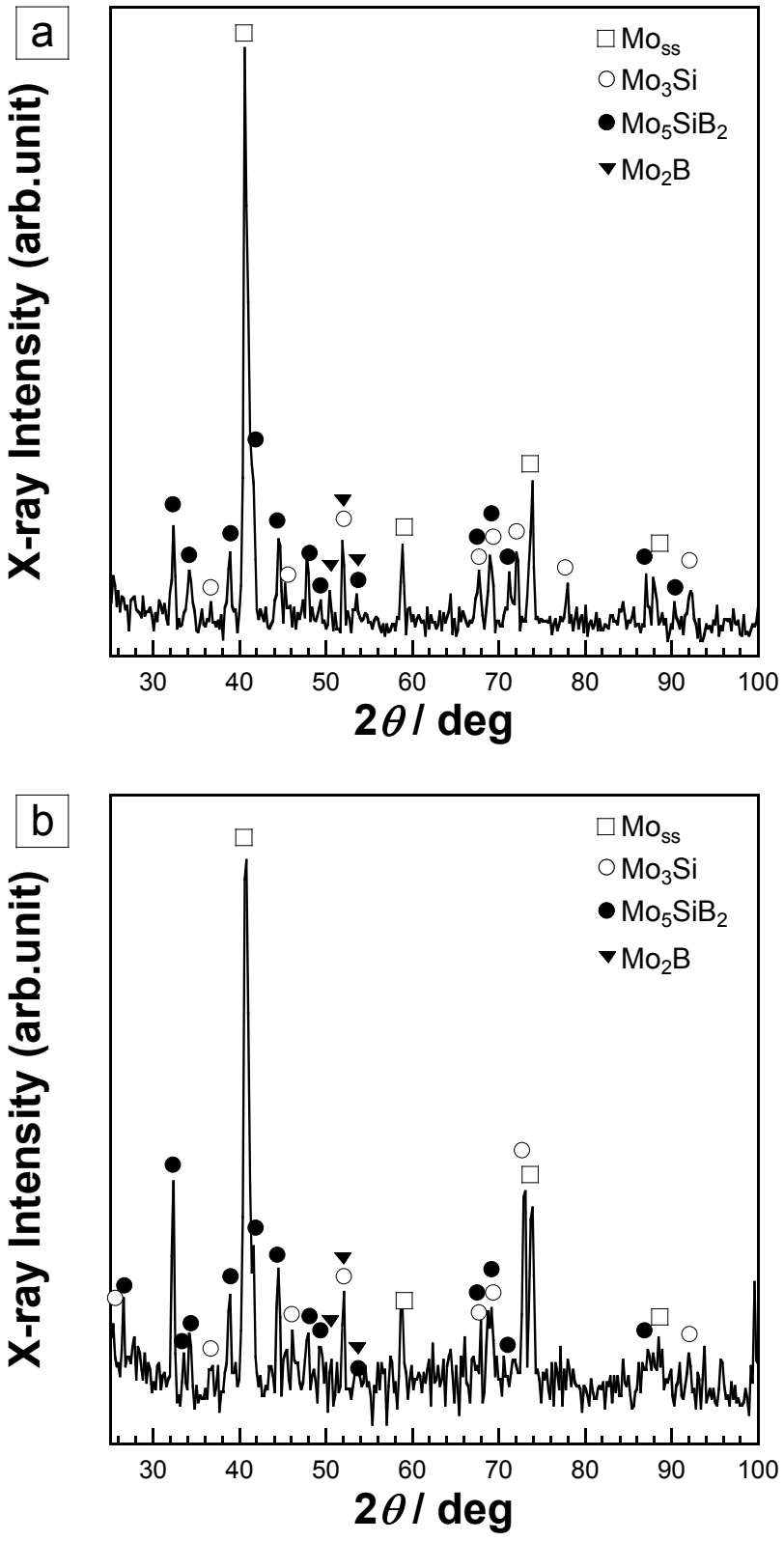


**Fig. 3.7 XRD diffraction pattern of Alloys (a) 6 and (b) 7.**

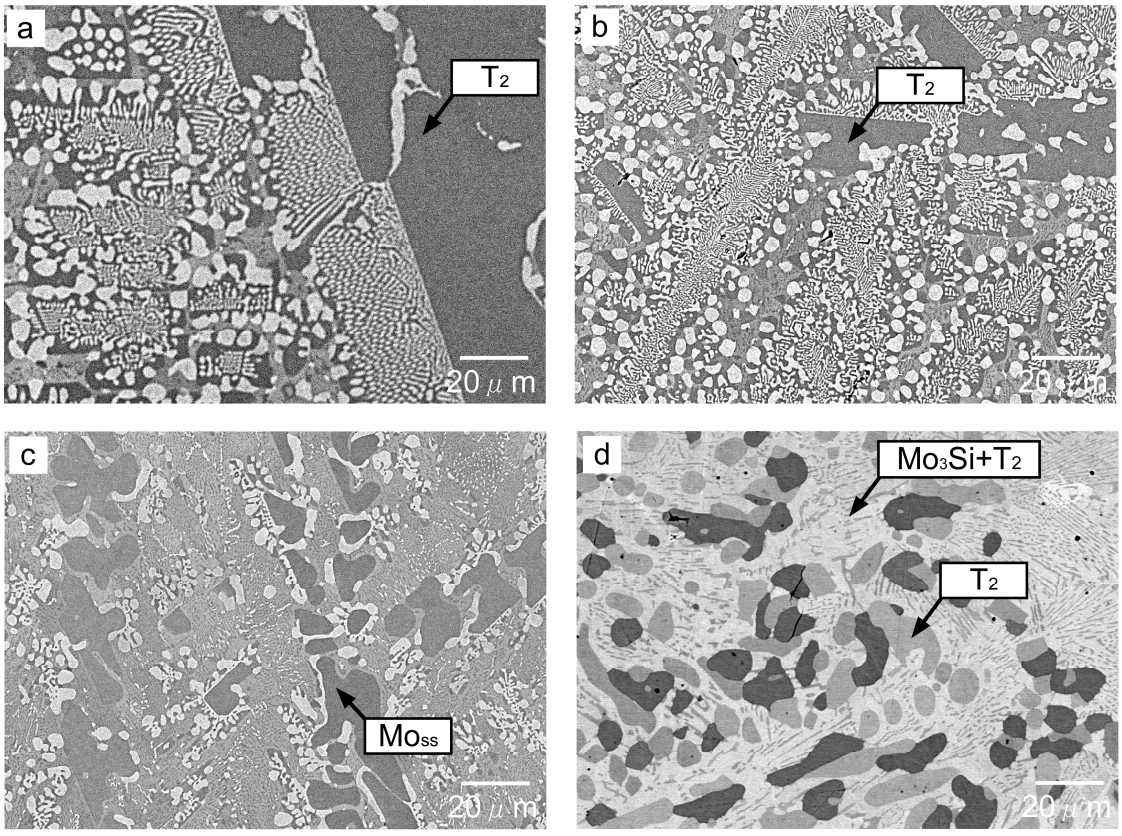


**Fig. 3.8 As-cast microstructures of Alloy (a) 8, (b) 9, (c) 10 and (d) 11.**

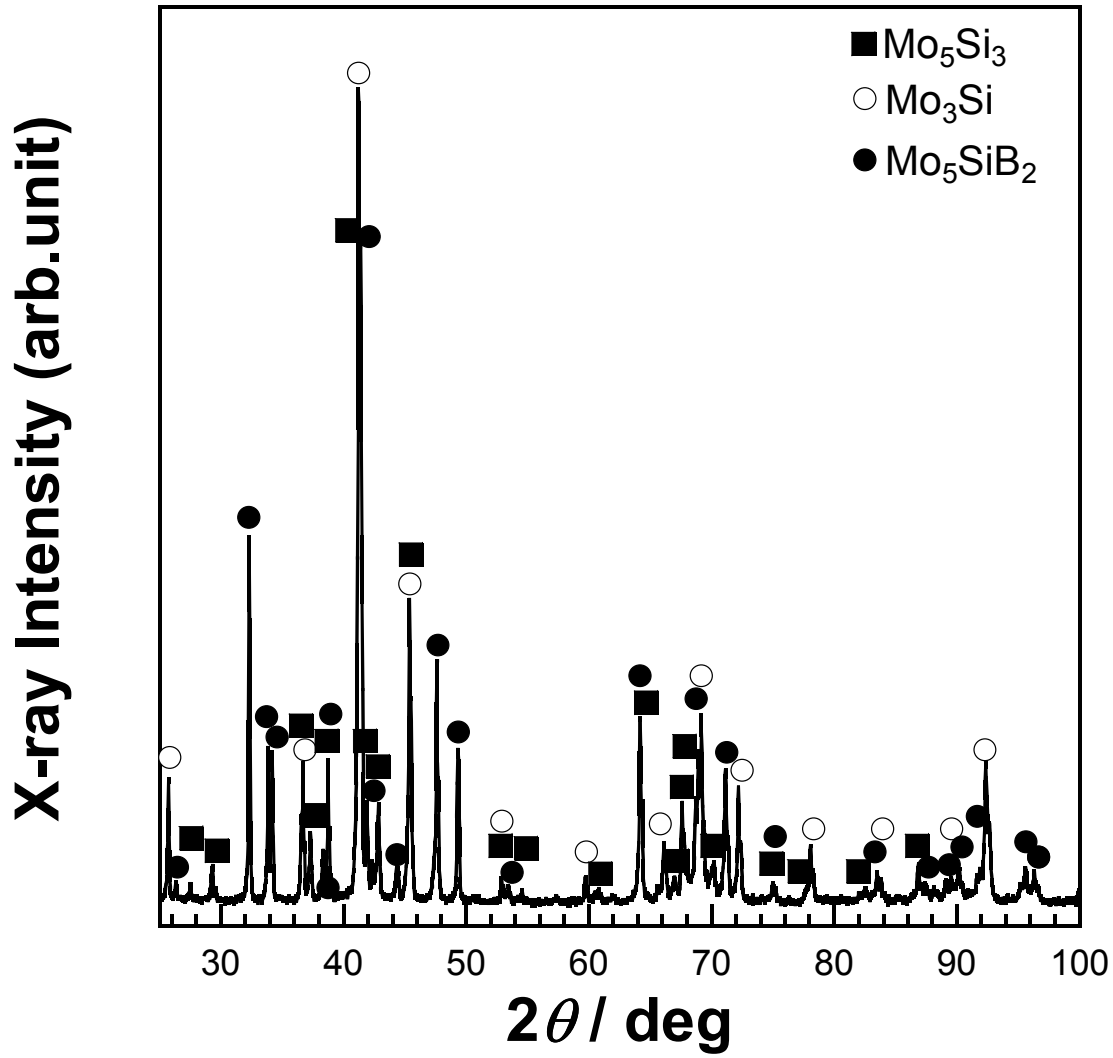


**Fig. 3.9 XRD diffraction pattern of Alloy 11.**

(a)

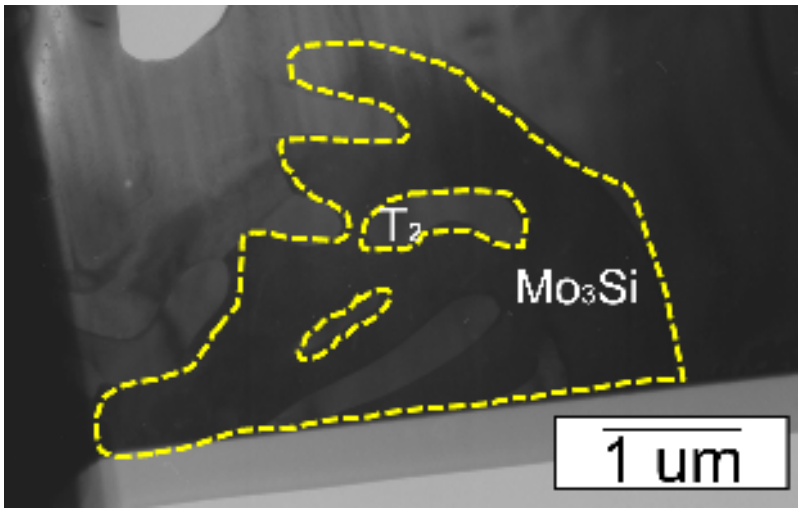


(b)

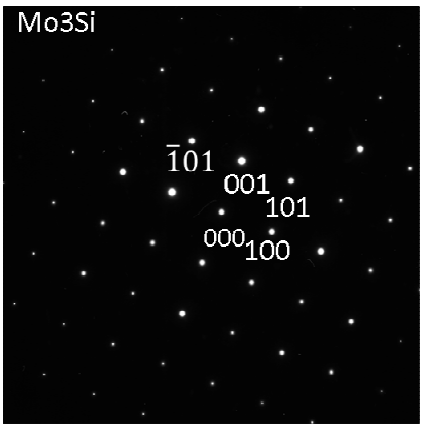


(c)

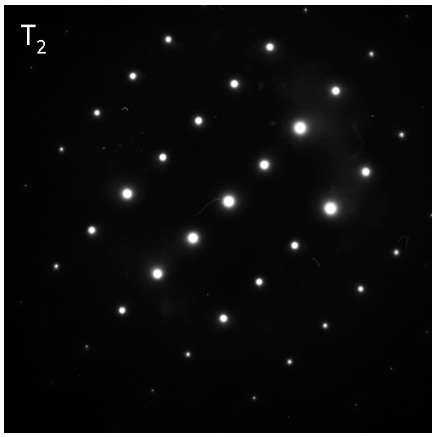


**Fig. 3.10 (a) Bright field TEM micrograph for $Mo_3Si$-$T_2$ eutectic phase in Alloy 11; (b), (c) characteristic X-ray intensity profiles for $Mo_3Si$ and $T_2$, respectively.**

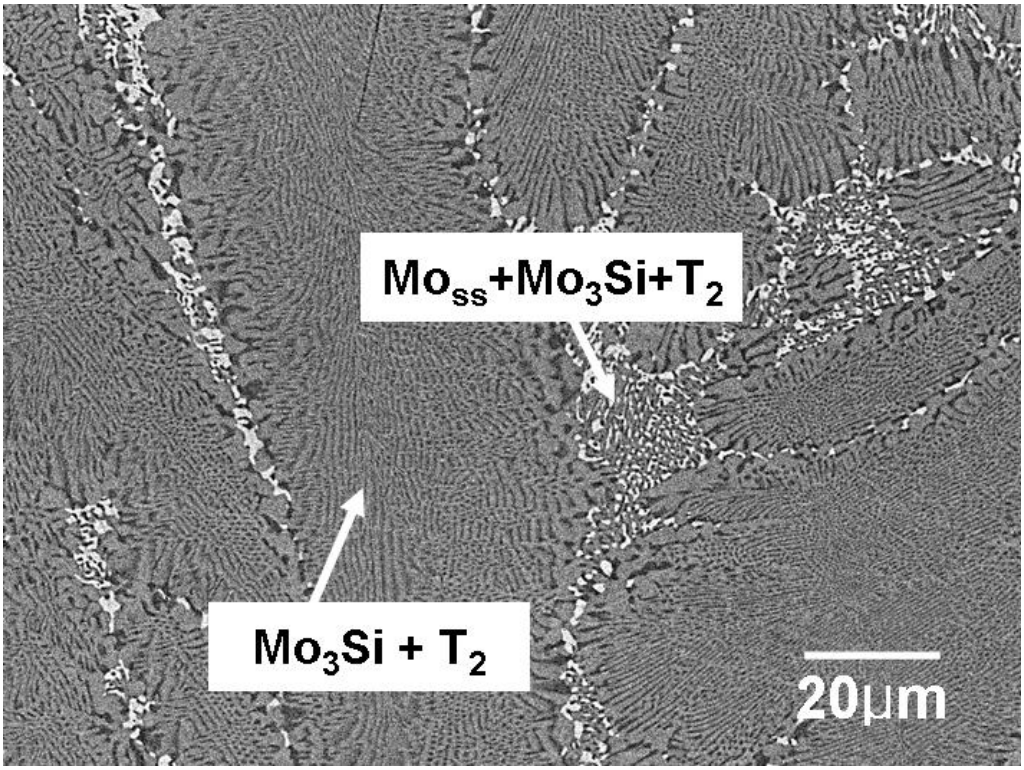


**Fig. 3.11 As-cast microstructures of Alloy 12.**

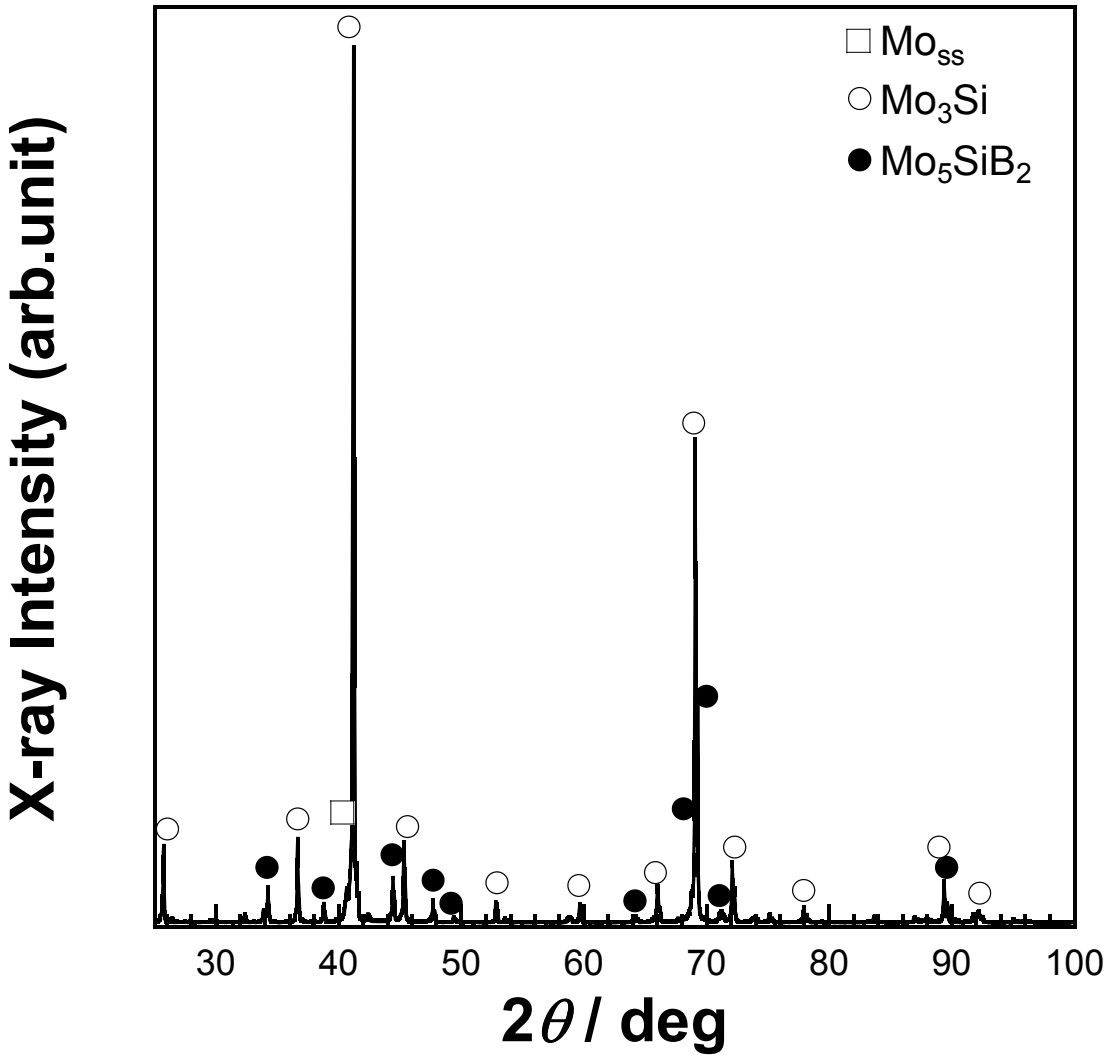


**Fig. 3.12 XRD diffraction pattern of Alloy 12.**

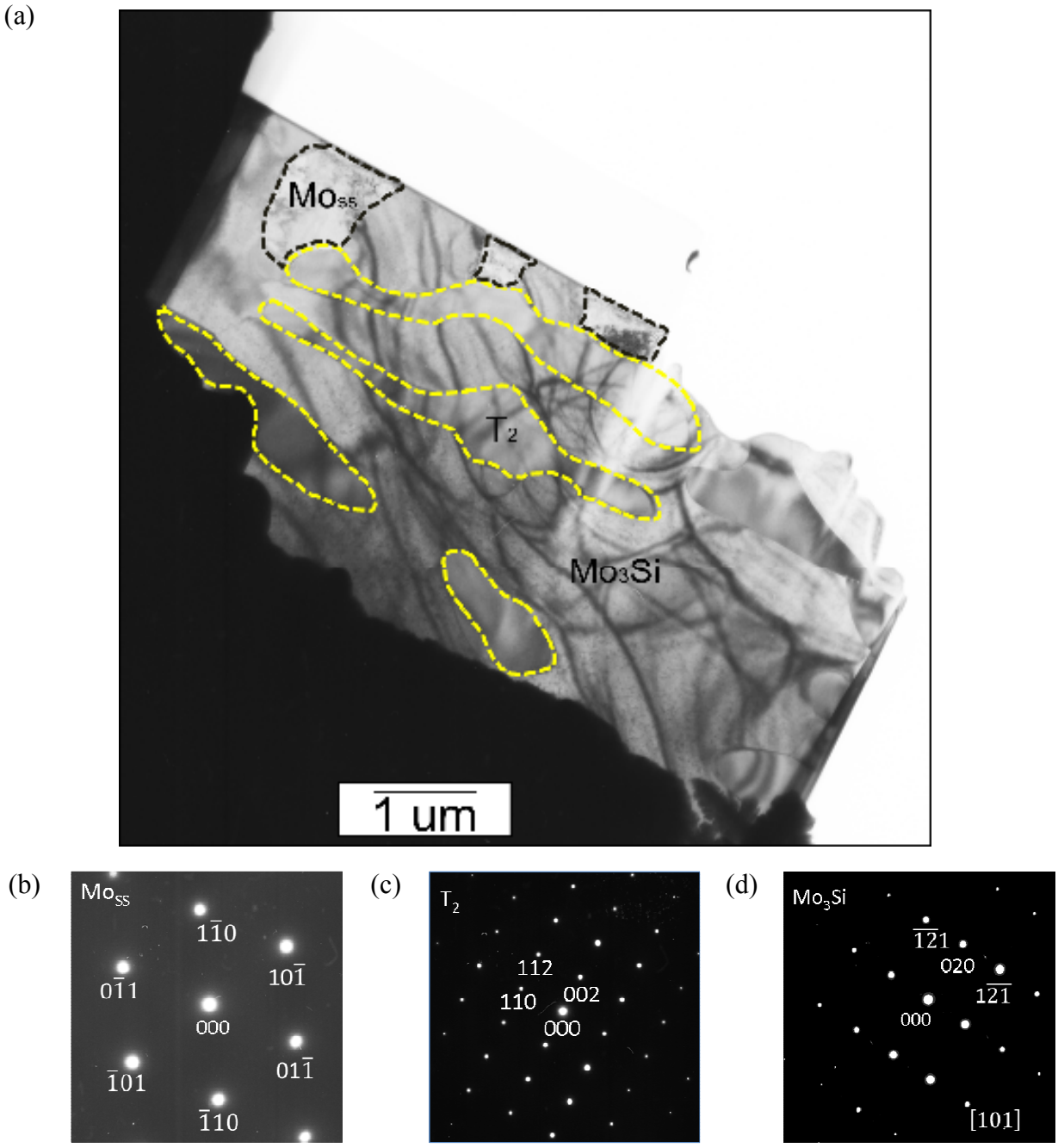


**Fig. 3.13 Bright field TEM micrograph for $Mo_{ss}$-$Mo_3Si$-$T_2$ phase in Alloy 12; (b)-(d) Diffraction patterns for the three phases, respectively.**

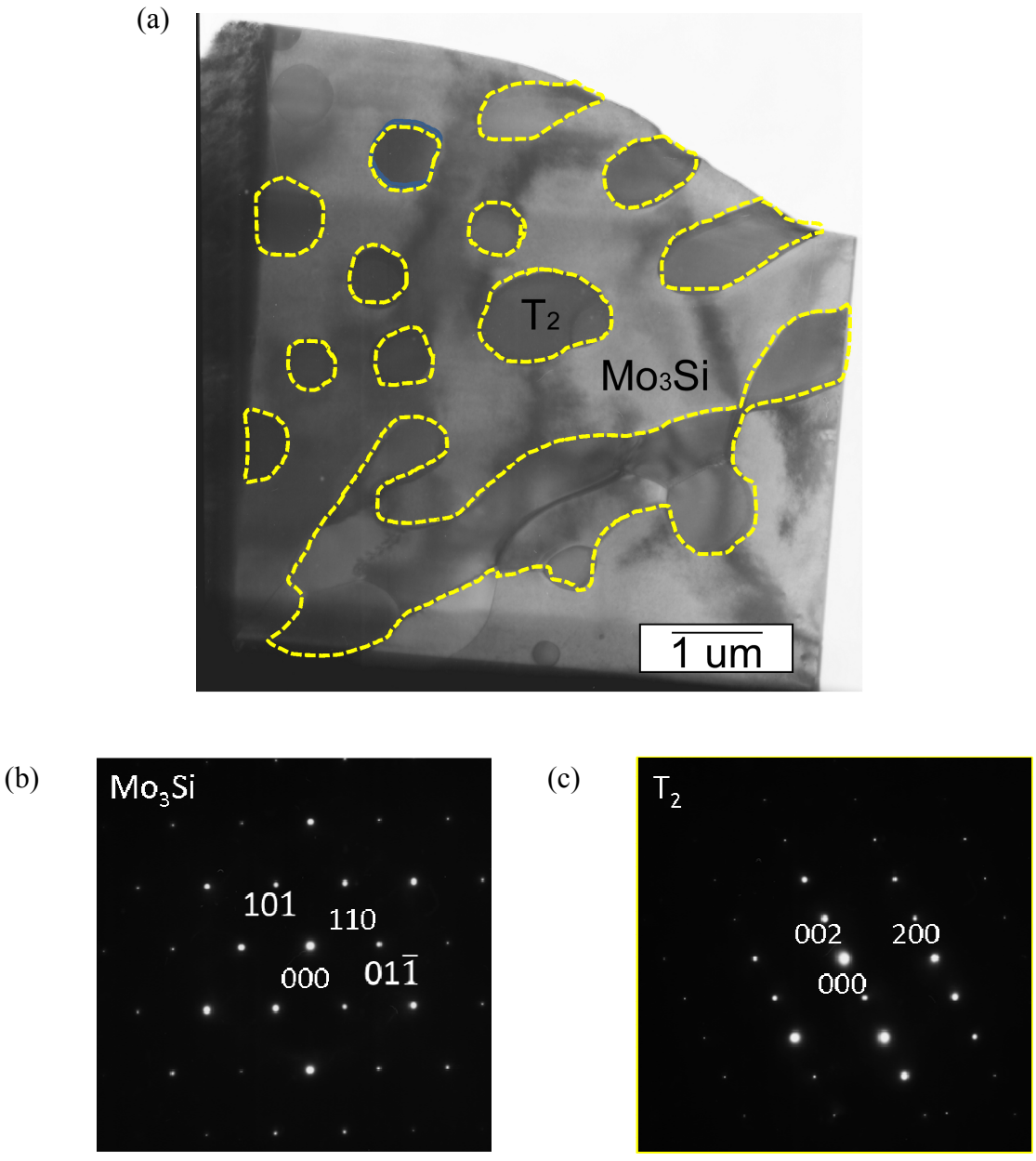


**Fig. 3.14 (a) Bright field TEM micrograph for $Mo_3Si$-$T_2$ eutectic phase in Alloy 12; (b), (c) characteristic X-ray intensity profiles for $Mo_3Si$ and $T_2$, respectively.**

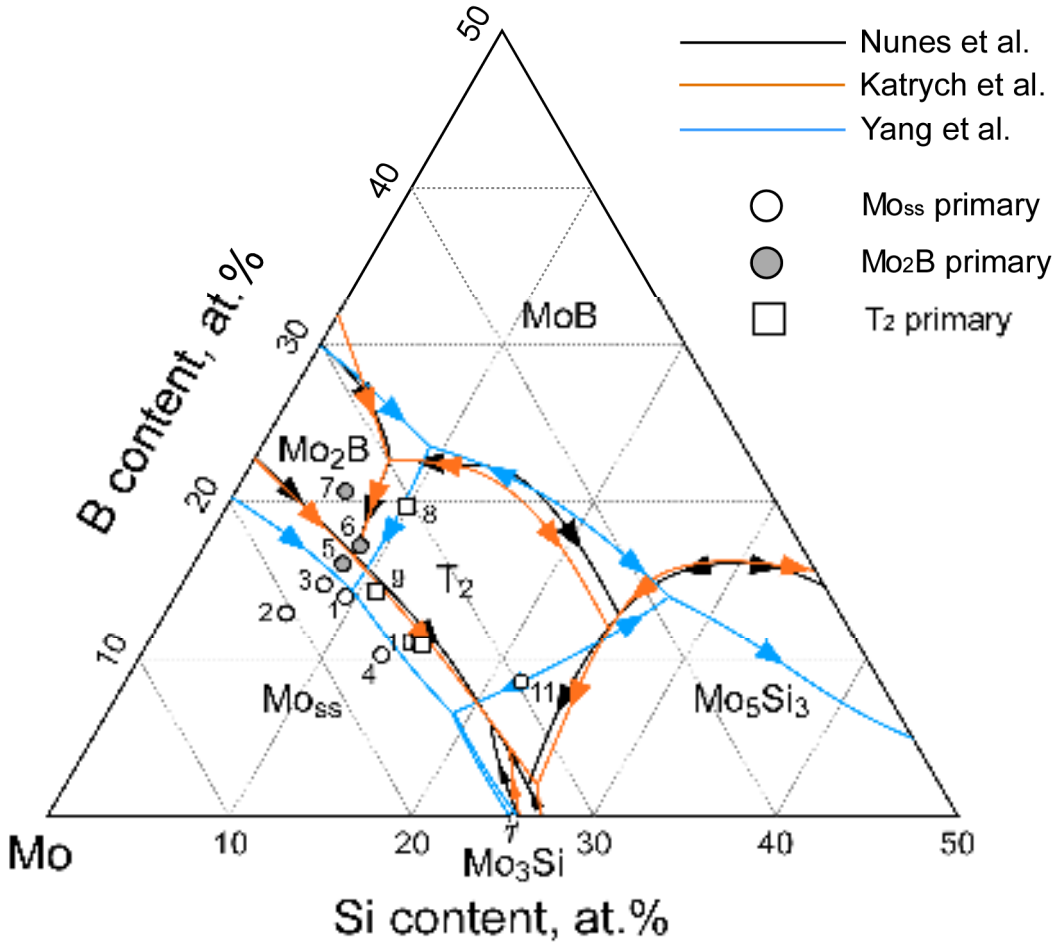


**Fig. 3.15 Primary phase formation observed in this study.**

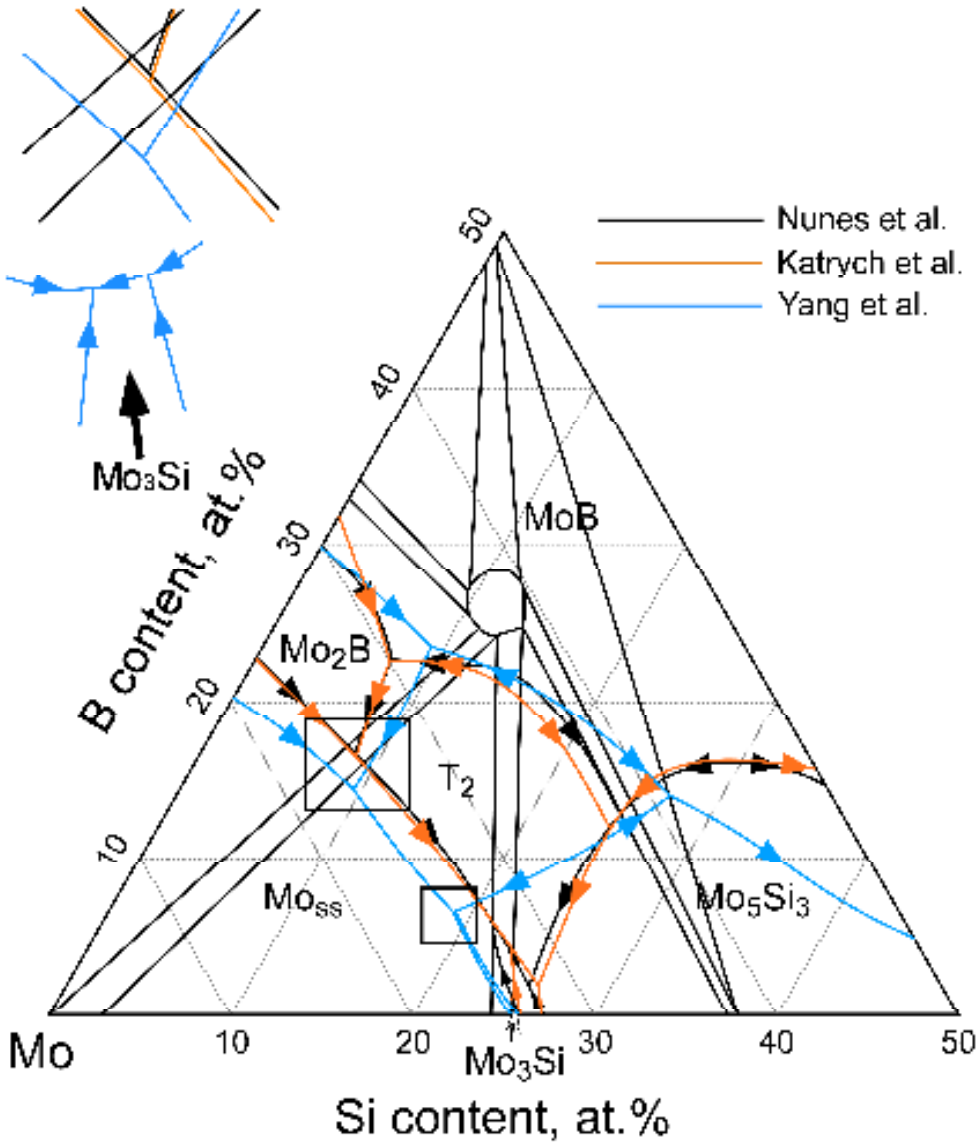


**Fig. 3.16 Comparison between three liquidus projections overlapping phase diagram at 1600 ˚C by Kim et al. [4-7].**

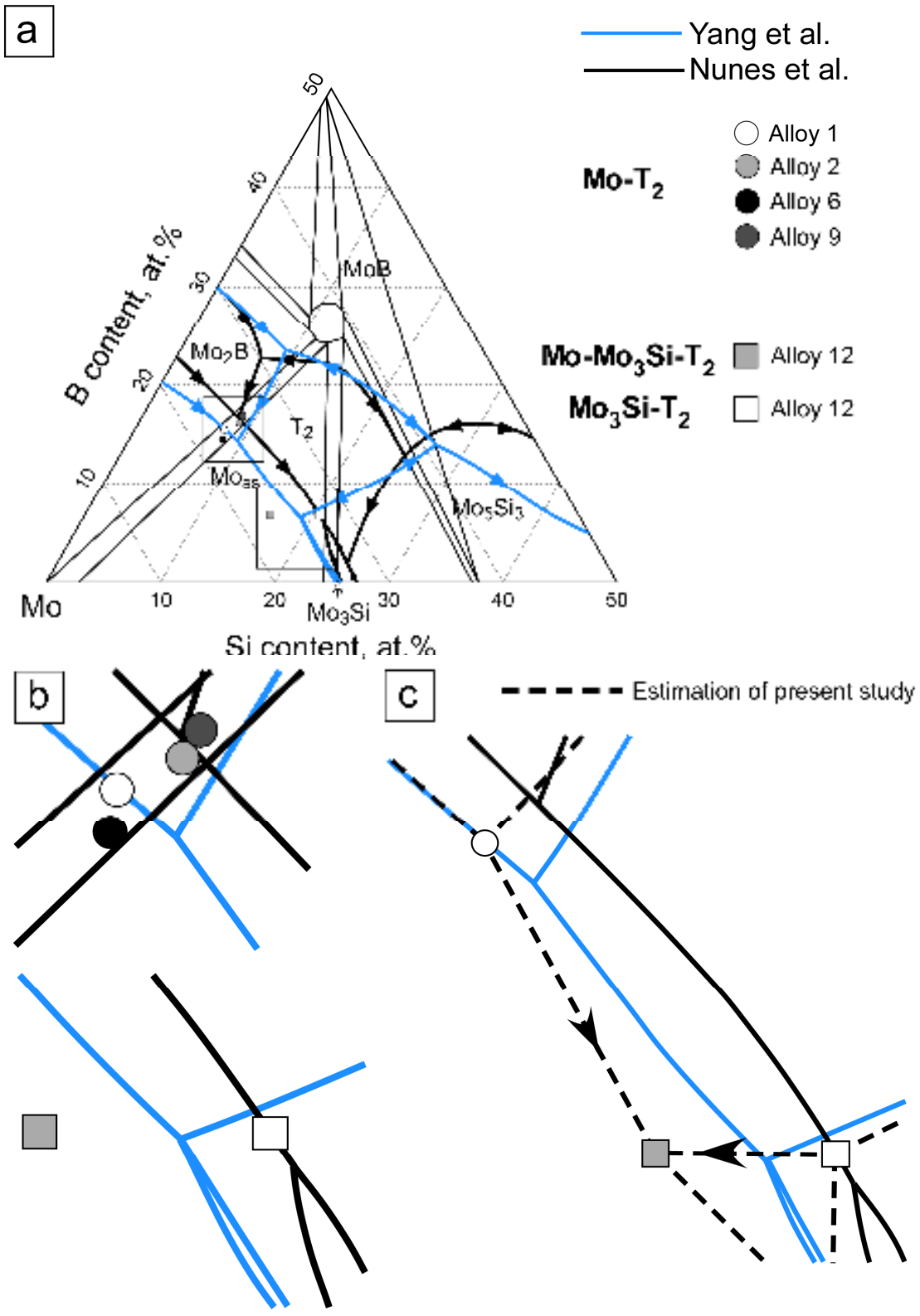


**Fig. 3.17 Phase compositions determined by EPMA; (b) enlargement and (c) solidification route based on the determined phase compositions.**

# CHAPTER 4

## Experimental Study on Single Phase Regions at 1800 °C in Mo-rich Portion of the Mo-Si-B Ternary System

### 4.1. Introduction

Recently, there have been large interests in developing ultra-high temperature structural materials as alternatives to Ni-based superalloys in order to improve the energy efficiency of gas turbine systems [1]. Nb-based alloys [2, 3], platinum group super-alloys [4, 5], eutectic ceramic oxides [6, 7], and Mo-TiC, ZrC or HfC eutectic alloys [8-10], have been put forward as new ultra-high temperature materials. Mo-Si-B ternary multi-phase alloys also have attracted great attention for ultra-high temperature applications [11-13]. In the Mo-rich portion of the ternary phase diagrams [14], there are silicide, boride and borosilicide phases, which have the melting point over 2000 °C.

The phase equilibrium of the Mo-Si-B ternary system was first studied by Nowotny et al. in 1954 [14]. Their phase diagram indicated that the compositional region of $Mo_5SiB_2$, so-called $T_2$, positioned near the stoichiometric composition of Mo-12.5mol%Si-25mol%B and expanded toward $Mo_5Si_3$ so-called $T_1$ region. After

Nowotny, the isothermal phase diagram at 1600 °C had been modified by Perepezko and his coworkers [15-17]. According to their reports, differently from that of Nowotny et al.[14], $T_2$ has a compositional region expanding toward the B-rich region, and Si and B solubility are negligible in borides and silicides. Yang et al. also reported an isotherm at 1600 °C obtained by thermodynamic calculations in 2005 [18]. Another isotherm work for the Mo-Si-B ternary system was also carried out at the higher temperature. In 2002, Katrych et al. [19] reported an isothermal diagram at 1850 °C with a liquidus projection. Their study, however, was mainly focused on solidification route for multi-phase formation. The information in terms of solubility values and element range was not sufficiently suggested for each single phase region. Huebsch et al. studied the solubility limit of B in $Mo_5Si_3$ at 1800 °C [20]. However, there was no report for the Mo-rich portion of the Mo-Si-B ternary system that all the single phase regions at temperature higher than 1600 °C were examined at temperature higher than 1600 °C with detailed values.

The main concern in this study is on the phase formation and microstructure stabilization of Mo-Si-B alloys at 1800 °C. In an earlier study, during annealing at 1800 °C, all as-cast microstructures were dramatically changed as if they reached phase equilibrium [21]. In this study, the solubility limits of constituent elements in Mo solid

solution, $Mo_3Si$, $Mo_5Si_3$, $Mo_2B$, MoB and $T_2$ at 1800 ° C were quantitatively investigated using field-emission (FE) gun-type electron probe micro-analysis (EPMA) calibrated in Chapter 2.

## 4.2. Experimental Procedures

In this study, 22 samples were prepared. The nominal compositions of the samples prepared are shown in Table 4.1 and also in the Mo-Si-B phase diagram [17] of Fig. 4.1. The button ingots of approx. 20 g in weight were produced by a conventional arc-melting technique from pure Mo (99.9 wt.%), Si (99.9999 wt.%) and B (99.95 wt.%) with a water-cooled copper crucible under an Ar atmosphere. Each alloy ingot was flipped and re-melted more than 5 times to ensure compositional homogeneity as possible. Prior to each melting, the furnace was evacuated and filled with high-purity Ar gas several times. A pure Ti ingot was melted before every melting to remove residual $O_2$ and $N_2$ gases. There was no large difference in alloy weight between before and after melting. Specimens for chemical analysis and microstructure observation were taken from the center of the ingots. The atomic ratios of Mo, Si and B in the as-cast alloys were analyzed by the inductively coupled plasma (ICP) – the optical emission spectrometry (OES) method [22]. The compositions chemically measured are also

shown in Table 4.1. Composition is expressed as atomic percent throughout this paper. The chemical composition measurements were skipped for Alloys T4-T12 and B1-B4 since the ICP-OES results of Alloys T1-T3 showed there was no visible change between the weighed and measured compositions. The impurity levels were measured by ICP-OES for Ti, Cu and W, and the obtained results are also shown in Table 4.1. Microstructures were observed by scanning electron microscopy (JEOL JSM-6500F) with back-scattered electron (BSE) images, and constituent phases were identified by X-ray diffractometry (XRD) (Bruker D-8 Advance). The quantitative composition analysis for constituent phases was performed by FE-EPMA (JEOL JXA-8530F) operated at 15kV and 20 nA. The calibration for quantitative analysis was based on the adopted in Chapter 2.

## 4.3. Results and Discussion

### 4.3.1 $Mo_{ss}$ Single Phase Region

The $Mo_{ss}$ single phase region was determined by quantifying the composition of $Mo_{ss}$ phase in Mo-11.7Si-14.4B (Alloy T1), Mo-8.7Si-17.4B (Alloy T2) and Mo-5.7Si-20.4B (Alloy T3) alloys, corresponding to the $Mo_{ss}$-$Mo_3Si$-$T_2$, $Mo_{ss}$-$T_2$ and $Mo_{ss}$-$Mo_2B$-$T_2$ regions, respectively, as well as in Mo-15Si (Alloy B1) for the

Mo-$Mo_3Si$ two-phase region and Mo-20B (Alloy B4) for the Mo-$Mo_2B$ two-phase region. In this study, binary determination at 1800 °C was examined mainly with previous Mo-Si and Mo-B binary phase diagram (Fig. 4.2 and 4.3) [23, 24]. The microstructures of Mo-15Si and Mo-20B alloys after heat treatment at 1800 °C for 24 h are shown in Fig.4.4. In Mo-15Si (Alloy B1), spherical or elongated $Mo_{ss}$ is distributed in $Mo_3Si$ matrix. The as-cast microstructure of Mo-15Si alloy is expected to form primary $Mo_{ss}$ and the microstructure of $L+Mo_{ss} \rightarrow Mo_3Si$ peritectic reaction based on Mo-Si binary phase diagram [23]. Mo-20B alloy (Alloy B4) corresponding to the Mo-$Mo_2B$ eutectic composition in the Mo-B binary system [24] shows the fine and homogeneous distribution of $Mo_{ss}$ in $Mo_2B$ matrix. The solubility of Si and B in $Mo_{ss}$ for the Mo-Si and Mo-B binary systems was determined using the Mo-15Si and Mo-20B alloys. The solubility limit of Si in $Mo_{ss}$ was found to be about 4.8 at%. Katrych et al. [19] reported that Si of about 5 at % was dissolved at 1850 °C in $Mo_{ss}$, confirming the data for the Mo-Si binary system obtained by Gokhale and Abbaschian [25]. The Si solubility at 1800 °C obtained in the present work is in good agreement with that by Katrych et al. [19], suggesting that there is little significant change by 50 °C difference. Concerning B solubility in $Mo_{ss}$, the limit at 1800 °C was found to be about 1.2 at% in the present work. Some experimental results obtained in previous

studies [26-28] support the obtained B solubility. Nowotny et al. [14] reported that $Mo_{ss}$ has the B solubility of 1 – 2 at% at 1600 °C. At the eutectic temperature of 2175 °C, Rudy et al. [26] estimated less than 2 at%B, and Portnoi et al. [27] reported about 1at%B. Zakharov et al. [28] reported the maximum solubility of 0.97 at% B at the eutectic point and about 0.5 at% B at 1600 °C.

In the Mo-Si-B ternary phase diagram at 1850 °C suggested by Katrych et al. [19], it was expressed that $Mo_{ss}$ has a small amount of B (approx. 1 at%), while there is no solubility when $Mo_{ss}$ contains the largest amount of Si. Recently, it was reported that the B solubility in $Mo_{ss}$ rises from 0 at% to 1.29 at% as temperature increases from 1600 °C to 1950 °C by Sakidja et al. [29]. On the other hand, B solubility appears to be negligible in the ternary phase diagram at 1600 °C experimentally obtained by Kim et al. [17]. It was also negligible in the Mo-B binary phase diagram obtained by thermodynamic calculations [18]. Anyhow, B solubility is not high compared with Si solubility in $Mo_{ss}$.

The microstructures of Mo-11.7Si-14.4B (Alloy T1), Mo-8.7Si-17.4B (Alloy T2) and Mo-5.7Si-20.4B (Alloy T3) alloys after heat treatment at 1800 °C for 24 h are shown in Fig. 4.5. Basically, each microstructure consists of $T_2$ matrix and $Mo_{ss}$ as dispersed phase. In Mo-11.7Si-14.4B (Alloy T1) (Fig. 4.5(a)), coarse $T_2$ phase were

occasionally observed, suggesting that the primary phase during solidification was $T_2$. Fine grain structures consisting of $Mo_{ss}$ and $Mo_3Si$ exist between coarse $T_2$ phase areas. Fine $Mo_{ss}$ precipitates were also observed in the primary $T_2$. Nunes et al. [15] suggested that the solubility of Mo in $T_2$ decreases as temperature decreases in a $Mo_{ss}$-$T_2$ pseudo-binary system. Therefore, the existence of $Mo_{ss}$ precipitates in $T_2$ after the heat treatment appears to be attributed to the change of Mo solubility. Mo-8.7Si-17.4B (Alloy T2) had a $Mo_{ss}/T_2$ two-phase microstructure (see Fig. 4.5(b)). Isolated fine $Mo_{ss}$ grains distributed in $T_2$ matrix often connecting each other. In Mo-5.7Si-20.4B (Alloy T3) (Fig. 4.5(c)), dendritic $Mo_{ss}$ and $Mo_2B$ phases remained in $T_2$ matrix. Based on the liquidus projection [18], the observed microstructure is reasonable because its composition lies in the region where $Mo_2B$ is the primary phase during solidification besides $Mo_2B$ is in equilibrium at 1800 °C. A small amount of microcracks was rarely observed in the $T_2$ matrix of Mo-5.7Si-20.4B (Alloy T3). The introduction of microcracks would be interpreted in terms of the difference in the coefficient of thermal expansion (CTE) of the constituent phases. Since CTE of $T_2$ phase is relatively higher ($a_a = 7.1 \times 10^{-6}$ /K, $a_c = 8.6 \times 10^{-6}$ /K) than that of $Mo_2B$ ($a = 5 \times 10^{-6}$ /K), $Mo_3Si$ ($a = 3 \times 10^{-6}$ /K) and Mo ($a = 6 \times 10^{-6}$ /K) [13, 30, 31], tensile stress should be generated in $T_2$ phase upon cooling. It should be noted that the microstructures largely changed from

their as-cast microstructures during the heat treatment through the decomposition of non-equilibrium phases [24]. For example, Mo-8.7Si-17.4B (Alloy T2) lies in the region where $Mo_2B$ is the primary phase in the liquidus projection [18], and its microstructure consists of coarse primary $Mo_2B$ phase and $Mo_{ss}$-$T_2$ and $Mo_{ss}$-$Mo_3Si$-$T_2$ eutectic phases [32]. After heat treatment at 1800 °C for 24 h, the primary $Mo_2B$ and $Mo_3Si$ disappeared, meaning that they were completely decomposed because they are non-equilibrium phases at the composition and temperature. Therefore, the heat treatment at 1800 °C for 24 h was proper to develop microstructure and obtain equilibrium phase relations for the Mo-Si-B alloys.

The solubility of Si and B in $Mo_{ss}$ measured for the alloys (Alloy B1, B4 and T1 – T3) is summarized in Fig. 4.6. B solubility was almost constant at 1.0-1.2 at% independent of Si concentration. Si solubility was decreased from 4.8 at% in the Mo-Si binary system to 3.4 at% with the addition of B for $Mo_{ss}$-$Mo_3Si$-$T_2$ three-phase alloys (T1 point) and to 1.6 at% Si for $Mo_{ss}$-$Mo_2B$-$T_2$ three-phase alloys (T3 point). In the Mo-1Si-1B alloy, a small amount of $Mo_2B$ was observed even after the heat treatment. Since the B concentration in the Mo-1Si-1B alloy analyzed by ICP was approx. 1.19 at%, which is almost the same as that in Mo-20B (Alloy B4), it is considered that the composition of the Mo-1Si-1B alloy is on the phase boundary between $Mo_{ss}$ and $Mo_2B$

compositional regions.

### 4.3.2 $Mo_3Si$ Single Phase Region

The $Mo_3Si$ single-phase region was determined by quantifying the composition of $Mo_3Si$ phase in Mo-18Si-10B (Alloy T4) and Mo-22Si-10B (Alloy T5) corresponding to $Mo_{ss}$-$Mo_3Si$-$T_2$ and $Mo_3Si$-$T_1$-$T_2$ three-phase regions, respectively, in addition to Mo-30Si (Alloy B2) as well as Mo-15Si (Alloy B1) examined in 3.2.1 for the Mo-Si binary system. The microstructure of Mo-30Si (Alloy B2) after heat treatment at 1800 °C for 24 h is shown in Fig. 4.7(a). For Mo-30Si (Alloy B2), the formation of the as-cast microstructure can be explained by the Mo-Si phase diagram [23]. The primary $Mo_5Si_3$ solidifies in liquid, and the solidification proceeds to the eutectic reaction of $Mo_3Si$-$Mo_5Si_3$. After the heat treatment, coarse and fine $T_1$ phase existed in $Mo_3Si$ matrix. Microcracks were occasionally observed in both coarse $T_1$ phase and $Mo_3Si$ matrix. The microcracking would be attributed to CTE ($a_a = 5.2 \times 10^{-6}$ /K, $a_c = 11.5 \times 10^{-6}$ /K) much higher than that of $Mo_3Si$ and its high anisotropy ($a_c/a_a \approx 2.2$) [ref.] in addition to the poor fracture toughness of $T_1$ [33]. The Si concentrations in binary $Mo_3Si$ were determined using Mo-15Si (Alloy B1) and Mo-30Si (Alloy B2). The compositional limit of Si was found to be about 24.9 at% in the Si-poor side and about 25.8 at% in the Si-rich side of $Mo_3Si$, which the deviation from the stoichiometric

composition is approx. ±1 at%. The values of the compositional limit of Si are in good agreement with the Mo-Si binary phase diagram [23].

The microstructures of Mo-18Si-10B (Alloy T4) and Mo-22Si-10B (Alloy T5) alloys after heat treatment at 1800 °C for 24 h are shown in Figs. 7(b) and (c). Since the compositions of both the alloys lie in the region where $T_2$ is the primary phase during solidification as shown in the liquidus projection [18], dendritc primary $T_2$ existed in $Mo_3Si$ matrix for Mo-18Si-10B (Alloy T4), and the complex dendrites consisting of $T_1$ and $T_2$ existed in $Mo_3Si$ matrix for Mo-22Si-10B (Alloy T5). The formation of the complex dendrites would be caused by that the composition of Alloy T5 lies near the $T_1$-$T_2$ mono-variant eutectic line in the liquidus projection [18].

For the Si compositional limits in the ternary $Mo_3Si$, there is no significant difference from that in the binary $Mo_3Si$ as shown in Fig. 4.8. With respect to the B compositional limits in the ternary $Mo_3Si$, it was found to be about 0.4 at%, though it was negligible in a previous study done by EPMA for the 1600 °C isotherm determination [17].

### 4.3.3 $Mo_5Si_3$ Single Phase Region

The $Mo_5Si_3$ single phase region was determined by quantifying the composition of $Mo_5Si_3$ phase in Mo-18Si-24.6B (Alloy T6) and Mo-22Si-24.6B (Alloy T7)

corresponding to the $T_1$-$T_2$-MoB and $T_1$-$MoSi_2$-MoB three-phase regions, respectively, as well as Mo-22Si-10B (Alloy T5) examined in 3.2.2, in addition to Mo-50Si (Alloy B3) as well as Mo-30Si (Alloy B2) examined in 3.2.2 for the Mo-Si binary system. The microstructure of Mo-50Si (Alloy B3) after heat treatment at 1800 °C for 24 h is shown in Fig. 4.9(a). In Mo-50Si (Alloy B3), dendritic $T_1$ exists in $MoSi_2$ matrix. Since the composition was close to that of the $T_1$-$MoSi_2$ eutectic point (55at%Si in the Mo-Si binary phase diagram [23]), fine $T_1$ particles also distributed between $T_1$ dendrites. Microcracks were observed particularly in $T_1$ phase and at the interface between $T_1$ and $MoSi_2$. The Si concentrations in binary $T_1$ were determined using Mo-30Si (Alloy B2) and Mo-50Si (Alloy B3), and obtained results are plotted in Fig. 10. The compositional range of Si in $T_1$ is from 38.4 to 41.1 at%, which is 1 at% higher than that of the Mo-Si binary phase diagram [23], i.e. 37.4 to 40 at%. As described before, the quantitative analysis of Mo and Si for Mo-Si binary alloys was conducted by the ZAF correction with pure Mo and $SiO_2$. The ZAF correction with a binary $T_1$ standard sample should be needed to quantify a large amount of Si.

For the ternary alloys, the Mo-18Si-24.6B (Alloy T6) alloy had a relatively homogeneous three-phase microstructure consisting of $T_1$, $T_2$ and MoB phases as shown in Fig. 4.9(b). In the Mo-22Si-24.6B (Alloy T7) alloy, $MoSi_2$ and MoB homogeneously

distributes in $Mo_5Si_3$ matrix as shown in Fig. 4.9(c). In both the ternary alloys, extensive microcracks were preferentially introduced in $T_1$ phase. Si concentration determined for $T_1$ phase in these ternary alloys ranged from about 37.7 at%, which is close to the stoichiometric composition of $T_1$, to about 40.7 at% as shown in Fig. 10. B concentration in $T_1$ phase ranged from about 0.9 at% in Mo-22Si-10B (Alloy T5) to about 1.2 at% in Mo-22Si-24.6B (Alloy T7), corresponding to the end of $Mo_3Si$-$T_1$-$T_2$ and $T_1$-$MoSi_2$-MoB three-phase regions.

A wider compositional area of $T_1$ phase was shown in the ternary phase diagram by Nowotny et al. [14]. The compositional limit of B in $T_1$ was about 4.5 at%. However, it is questionable since a B material as pure as about 83 at% was employed as the standard for the quantitative analysis of B in their study [20]. After Nowotny et al., a more careful work was carried out by Huebsch et al. [20] to determine the $T_1$ single-phase region at 1800 °C. In the study, the concentrations of Mo and Si were determined by EPMA, while B concentration was derived from alloy composition and XRD measurement. The value of B concentration in $T_1$ phase obtained by Huebsch et al. ranged from 1.5 to 2 at% [20], which is higher than that obtained in the present study. The higher B concentration obtained by Huebsch et al. might be caused by the uncertain detection ability of XRD against phases in a small volume fraction. The B

concentrations of $T_1$ phase shown in the studies by Nowotny et al. [14] and Huebsch et al. [20] have the maximum values at the end of the $T_1$-$T_2$-MoB three-phase region, corresponding to the T6 point in Fig. 4.10(b). On the other hand, the B concentration is slightly higher at the end of $T_1$-$MoSi_2$-MoB corresponding to the T7 point than at the T6 point in this study. However, it would be nothing worth to consider the difference due to a level of about 0.1 at%.

### 4.3.4 $T_2$ Single Phase Region

$T_2$ single phase region was determined by quantifying the composition of $T_2$ phase in the alloys corresponding to all three-phase regions surrounding the $T_2$ single phase region; Mo-11.7Si-14.4B (Alloy T1), Mo-22Si-10B (Alloy T5), Mo-22Si-10B (Alloy T6), Mo-7.7Si-38.4B (Alloy T8), Mo-6.2Si-33B (Alloy T10) and Mo-6.2Si-27B (Alloy T12) after the heat treatment. The microstructures of Mo-7.7Si-38.4B (Alloy T8), Mo-6.2Si-33B (Alloy T10) and Mo-6.2Si-27B (Alloy T12) are shown in Fig. 4.11. Mo-7.7Si-38.4B (Alloy T8) had a homogeneous microstructure consisting of $T_1$, $T_2$ and MoB as shown in Fig. 4.11 (a). The volume fraction of $T_2$ phase was smaller than other phases, indicating that the composition is away from the $T_2$ single-phase region. Microcracks were somewhat observed in $T_1$ phase as in other alloys. In Mo-6.2Si-33B (Alloy T10), it was obvious that the matrix is $T_2$ phase. $Mo_2B$ and MoB particles are

homogeneously distributed in the matrix. In Mo-6.2Si-27B (Alloy T12), a dendritic structure of $T_2$ and $Mo_2B$ remained with a small amount of $Mo_{ss}$. $T_2$ phase contained $Mo_{ss}$ precipitates, different from the aspect of $T_2$ in Mo-6.2Si-33B (Alloy T10) mentioned above.

The compositional region of $T_2$ single-phase determined by EPMA ranges from 10.2 to 13.3 at% for Si and from 23.5 to 25.6 at% for B as shown in Fig. 12. The range does not include the $T_2$ stoichiometric composition. This implies that a $T_2$ single-phase could not be obtained at the stoichiometric composition at 1800 °C. The $T_2$ single-phase region obtained in the present work had an elongated shape from near the $T_2$ stoichiometric composition toward $Mo_2B$. This shape is very similar to those at 1600 °C reported by Yang et al. [18] and at 1850 °C by Katrych [19]. On the other hand, it is considerably different from that at 1600 °C by Kim et al. [17]. They reported a round-shape $T_2$ single-phase region widely expanding from the $T_2$ stoichiometric composition toward the B-rich side. The $T_2$ single-phase regions reported by Nowotny et al. [14] is much smaller than that by Kim et al. [17] but just lies on the $T_2$ stoichiometric composition. Therefore, there have been conflicts on $T_2$ single-phase region between phase diagrams so far, suggesting that it is more difficult to determine $T_2$ single-phase region than other phase regions. As shown in chapter 2, the standard

sample S1 prepared for $T_2$ measurements, having almost the stoichiometric composition of $T_2$ (Mo-12.2Si-24.8B), showed the $T_2$ matrix with a small amount of MoB. This result strongly supports the validity of the $T_2$ single-phase region obtained in the present work.

### 4.3.5 MoB Single Phase Region

MoB single phase region was determined by quantifying the composition of MoB phase in Mo-18Si-24.6B (Alloy T6), Mo-22Si-24.6B (Alloy T7), Mo-7.7Si-38.4B (Alloy T8), Mo-3.7Si-38.4B (Alloy T9) and Mo-6.2Si-33B (Alloy T10) alloys, corresponding to $T_1$-$T_2$-MoB, $T_1$-$MoSi_2$-MoB and $T_2$-$Mo_2B$-MoB three-phase regions, respectively. The microstructure of Mo-3.7Si-38.4B (Alloy T9) is shown in Fig. 4.13. It mainly consisted of $T_2$ and MoB and also a small amount of $Mo_2B$ frequently at the interfaces between $T_2$ and MoB. B concentration in binary MoB was considered to be almost the same as that in ternary MoB due to the extremely small solubility of Si in MoB [19]. Therefore, the compositional range in binary MoB was not examined in this study.

The compositional limit of B in the MoB single phase region was found to be 48.8 at% in the B-poor side at the T9 or T10 point, 49.77 at% at the end point of the $T_1$-$T_2$-MoB three-phase region corresponding to the T6 or T8 point, and 50.55 at% in the

B-rich side at the T7 point as shown in Fig. 4.14. In a Mo-B binary phase diagram, there are two structural forms of MoB; αMoB and βMoB [24]. Both of them have a nearly stoichiometric composition with small off-stoichiometric ranges; 48 to 50 at% B for αMoB and 48 to 51 at% B for βMoB [15-17, 19]. βMoB exists in temperature range from 1800 °C corresponding to that of the heat treatment in this study to about 2600 °C which is the melting point. Thus, there may be two structural forms of MoB in the alloys examined in the present study. Si solubility in MoB was negligible because Si concentration under 0.1at% was detected to dissolve in MoB, which is in good agreement with that reported in previous studies.

### 4.3.6 $Mo_2B$ Single Phase Region

$Mo_2B$ single-phase region was determined by quantifying the composition of $Mo_2B$ phase in Mo-3.7Si-38.4B (Alloy T9), Mo-6.2Si-33B (Alloy T10), Mo-6.2Si-30B (Alloy T11) and Mo-6.2Si-27B (Alloy T12) alloys, corresponding to $T_2$-$Mo_2B$-MoB and $Mo_{ss}$-$T_2$-$Mo_2B$ three-phase regions, respectively. The microstructure of Mo-6.2Si-30B (Alloy T11) is shown in Fig. 4.15. It appeared to consist of two phases of $T_2$ and $Mo_2B$ though the nominal composition of the alloy was aimed to that in the $T_2$-$Mo_2B$-MoB three-phase region. The chemical analyses of alloy compositions were done for all of the standard samples (S1 to S6) in chapter 2 and Alloy T1-T3, but not for Alloy T4-T12.

Remarkable composition change might occur during arc-melting due to the evaporation of B and/or Si, causing their microstructural discrepancy, and as a result the composition shifted to the $T_2$-$Mo_2B$ two-phase region. According to the liquidus projection [18], the nominal composition of (Alloy T11) is entirely in the region of primary MoB. Thus, the MoB phase was supposed to exist in a certain amount in the as-cast microstructure of the alloy. This strongly suggests that the primary MoB phase was completely decomposed during the heat treatment and the alloy achieved the equilibrium state at the temperature. As described in chapter 2, Alloy S1 that was aimed to $T_2$ single-phase and had almost the stoichiometric composition of $T_2$ showed the residual of MoB even after the heat treatment. Based on the $T_2$ single-phase region at 1800 °C determined in the present work, it is positive that the chemical composition of Alloy S1 (Mo-12.2Si-24.8B) is not in the $T_2$ single-phase region, which is also in good agreement with the existence of MoB in Alloy S1. Further studies would be required to more precisely determine the $T_2$ single-phase region.

$Mo_2B$ single-phase region for B widely ranged around the vicinity of the stoichiometric composition (33.3 at%B). The concentration of B in $Mo_2B$ was found to be 32.3 at% for Mo-6.2Si-27B (Alloy T12), 33.98 at% for Mo-6.2Si-30B (Alloy T11), and 37.1 at% for Mo-3.7Si-38.4B (Alloy T9) and Mo-6.2Si-33B (Alloy T10) as shown

in Fig. 16. The determined $Mo_2B$ compositional range can be divided into two regions; one was located near the stoichiometric composition and another located near 40 at%B. Therefore, it was considered for the existence of other borides near the composition of $Mo_2B$ in this study. In previous studies on Mo-B binary phase diagrams, Steinitz et al. [34] and Gilles et al. [35] reported the existence of $Mo_3B_2$ phase. From their results, the temperature that $Mo_3B_2$ is in equilibrium ranges from about 1900 to 2100 °C. Recently, Tojo et al. [36] studied the phase equilibria of Cr-Mo-B ternary system. $Mo_3B_2$ definitely existed in the temperature range from about 1900 °C about 100 °C-higher than in the Mo-B binary phase diagram by Tojo et al. [36]. From these references [34-36], the Mo boride of about 37 at%B observed in Mo-3.7Si-38.4B (Alloy T9) and Mo-6.2Si-33B (Alloy T10) is considered to be $Mo_3B_2$, though the temperature for the heat treatment was about 100 °C lower than that by Tojo et al. [36]. On the other hand, the XRD results for Alloy T9 and T10 indicates the existence of MoB, $T_2$ and $Mo_2B$ (see Fig. 4.17). It is questionable why the B concentration in the $Mo_2B$ is overquantified when the $Mo_2B$ coexists with MoB.

### 4.3.7 Combination of Determined Single Phase Regions

From the determined single phase regions, two and three-phase regions in Mo-rich portion was constructed as shown in Fig. 4.18. $T_2$ phase has narrow two-phase regions

with $Mo_2B$, $Mo_3Si$ and $Mo_5Si_3$, similar to that at 1850 °C by Katrych et al. [19]. On the other hand, $T_2$ exhibits considerably expanded two-phase region with MoB, which is in good agreement with those of Kim et al. [17] and Katrych et al. [19].

### 4.4 Conclusions

In this work, the solubility or compositional limits of the single phase regions at 1800 °C in the Mo-rich portion of the Mo-Si-B ternary system were quantitatively determined using the alloys corresponding to three-phase regions. The conclusions are listed as following.

(1) For accurate composition determination by EPMA, the correction was carried out using standard samples originally prepared aimed to each single phase composition.

(2) The solubility limits at 1800 °C in all the single phase regions obtained with the correction appear to be different with those of the previous reports at 1600 °C, especially for low level solubility.

(3) In the present study, the solubility was determined in the level of 0~1at%. This implies that the accurate measurement was achieved after the correction.

(4) $T_2$ single phase region determined in this study doesn't include its stoichiometric composition. This would be direct evidence that $T_2$ single phase can not

be obtained, even though it was aimed to the stoichiometric composition.

**References**


[1] Zhao JC, Westbrook JH. MRS Bulletin 2003;**28**:622-627.

[2] Bewlay BP, Jackson MR, Zhao JC, Subramanian PR, Mendiratta MG, Lewandowski JJ. MRS Bulletin 2003;**28:**646-653.

[3] Ma CL, Li JG, Tan Y, Tanaka R, Hanada S. Mater Sci Eng A 2004;**386:**375-383.

[4] Yamabe-Mitarai Y, Ro Y, Maruko T, Harada H. Metall Mater Trans A 1998;**29A:**537-549.

[5] Cornish LA, Fischer B, Völkl R. MRS Bulletin 2003; **28:**632-638.

[6] Waku Y, Nakagawa N, Wakamoto T, Ohtsubo H, Shimizu K, Kohtoku Y. Nature 1997;**389**:49-52.

[7] Llorca J, Orera VM. Prog Mater Sci 2006;**51:**711-809.

[8] Kurishita H, Shiraishi J, Matsubara R, Yoshiaga H. J Jpn Inst Met 1985;**49**:963-971.

[9] Suzuki T, Nomura N, Yoshimi K, Hanada S. Mater Trans JIM 2000;**41**:1164-1167.

[10] Suzuki T, Matsumoto H, Nomura N, Yoshimi K, Hanada S. Trans Mater Res Soc Jpn 2001;**26**:307-310.

[11] Ito K, Ihara K, Tanaka K, Fujikura M, Yamaguchi M. Intermetallics 2001; **9**:591-602.

[12] Yoshimi K, Nakatani S, Suda T, Hanada S, Habazaki H. Intermetallics

2002;**10**:407-414.

[13] Mitra R. Intl Mater Rev 2006;**51**:13-64.

[14] Nowotny H, Kieffer R, Benesovsky F. Planseeberichte Fuer Pulvermetallurgie 1957;**5:**86.

[15] Nunes CA, Sakidja R, Perepezko JH. in Structural Intermetallics 1997 ed by Nathal MV, Darolia R, Liu CT, Martin PL, Miracle DB, Wagner R, Yamaguchi M; TMS, Warrendale, PA, 831-839.

[16] Sakidja R, Myers J, Kim S, Perepezko JH. Int J Refract Met H 2000;18:193-204.

[17] Kim ST, Perepezko JH. J Phase Equilib Diffus 2006;**27:**605-613.

[18] Yang Y, Chang YA. Intermetallics 2005;**13:**121-128.

[19] Katrych S, Grytsiv A, Bondar A, Rogl P, Velikanova T, Bohn M. J Alloy Compd 2002;347:94-100.

[20] Huebsch JJ, Kramer MJ, Zhao HL, Akinc M. Intermetallics 2000;**8:**143-150.

[21] Yoshimi K, Nakatani S, Nomura N, Hanada S. Intermetallics 2003;11:787-794.

[22] Danzaki Y, Wagatsuma K, Syoji T, Yoshimi K. Fresenius J Anal Chem 2001;**369:**184-186.

[23] Okamoto H. JEPD 2011;32:176.

[24] Spear KE, Liao PK. Bull Alloy Phase Diag. 1988;9:457-466.

[25] Gokhale AB, Abbaschian GJ. Bull Alloy Phase Diag 1991;12:493-498.

[26] Rudy E, St. Windisch. Part I Vol III Systems Mo-B and W-B, 1965.

[27] Portnoi KI, Levinski YV, Romashov VM, Mordovin OA, Levinskaya MK, Izv Akad Nauk SSSR Met 1967;4:171-176.

[28] Zakharov AM, Novikov II, Polk VS, Gimelfarb FA. Izv Akad Nauk SSSR Met 1973;4:236-241.

[29] Sakidja R, Perepezko JH, Kim S, Sekido N. Acta Materialia 2008;56:5223-5244.

[30] Martienssen W, Warlimont H. Springer handbook of condensed matter and materials data 2005:1.

[31] Latreche H, Bozzolo G, Masseta PJ, Weber T, Schützea M. Mater Sci Eng A 2010;527:5837-5843.

[32] Ha SH, Yoshimi K, Maruyama K, Tu R, Goto T. Materials Transactions 2010;51:1699-1074.

[33] Nunes CA, Sakidja R, Dong Z, Perepezko JH. Intermetallics 2000;**8:**327-337.

[34] Steinitz R, Binder I, Moskowitz D. J Met 1952;4:983-987.

[35] Gilles PW, Pollock BD. J Met 1953;5:1537-1539.

[36] Tojo M, Tokunaga T, Ohtani H, Hasebe M. CALPHAD 2010;34:263-270.

**Table 1 Nominal and measured composition of the employed alloys.**

| Alloy no. | Nominal Composition (at%) | | Measured Composition (at%) | | Ti Content (ppm) | Cu Content (ppm) | W Content (ppm) |
|---|---|---|---|---|---|---|---|
| | Si | B | Si | B | | | |
| T1 | 5.7 | 20.4 | 6.0 | 20.8 | <10 | <10 | <100 |
| T2 | 8.7 | 17.4 | 8.5 | 17.2 | <10 | <10 | <100 |
| T3 | 11.7 | 14.4 | 12.0 | 14.6 | <20 | <10 | <100 |
| T4 | 18 | 10 | | | | | |
| T5 | 22 | 10 | - | - | - | - | - |
| T6 | 18 | 24.6 | - | - | - | - | - |
| T7 | 22 | 24.6 | - | - | - | - | - |
| T8 | 7.7 | 38.4 | - | - | - | - | - |
| T9 | 3.7 | 38.4 | - | - | - | - | - |
| T10 | 6.2 | 33 | - | - | - | - | - |
| T11 | 6.2 | 30 | - | - | - | - | - |
| T12 | 6.2 | 27 | | | | | |
| B1 | 15 | - | - | - | - | - | - |
| B2 | 30 | - | - | - | - | - | - |
| B3 | 50 | - | - | - | - | - | - |
| B4 | - | 20 | - | - | - | - | - |

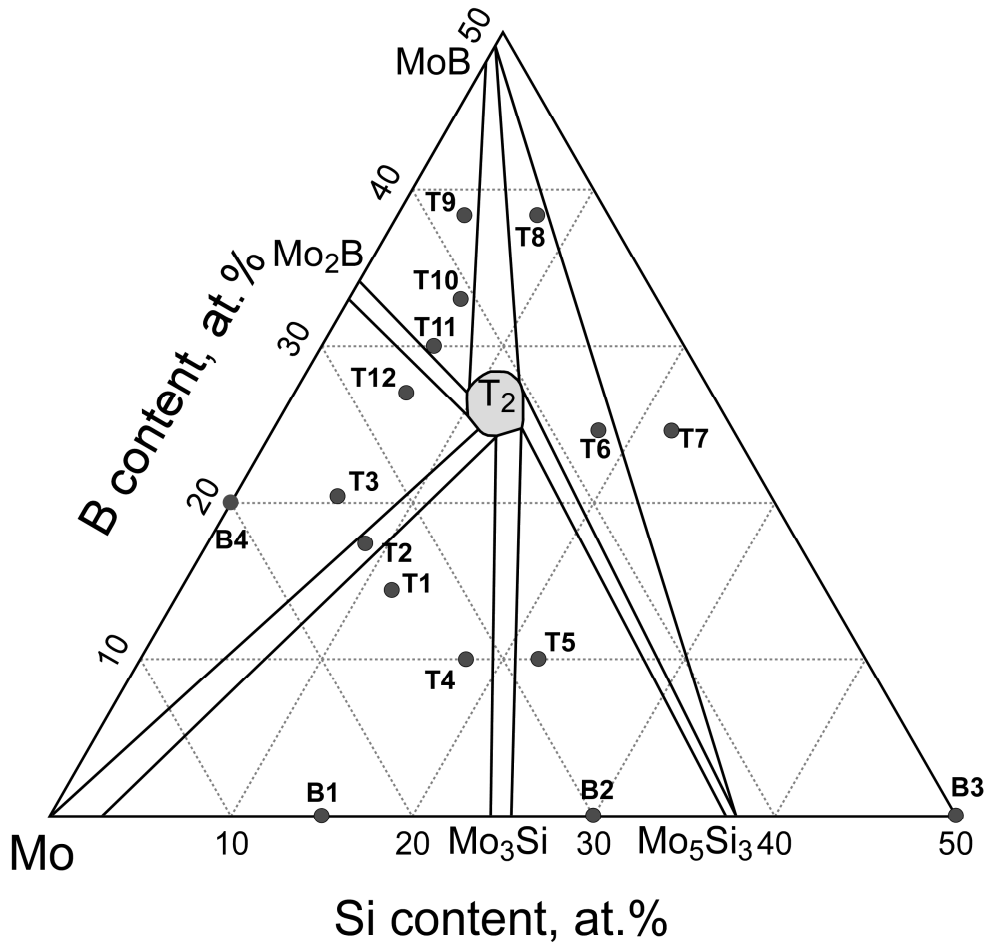


**Fig. 4.1 Compositions of the alloys plotted in the Mo-Si-B ternary phase diagram at 1600 ˚C by Kim et al. [17]**

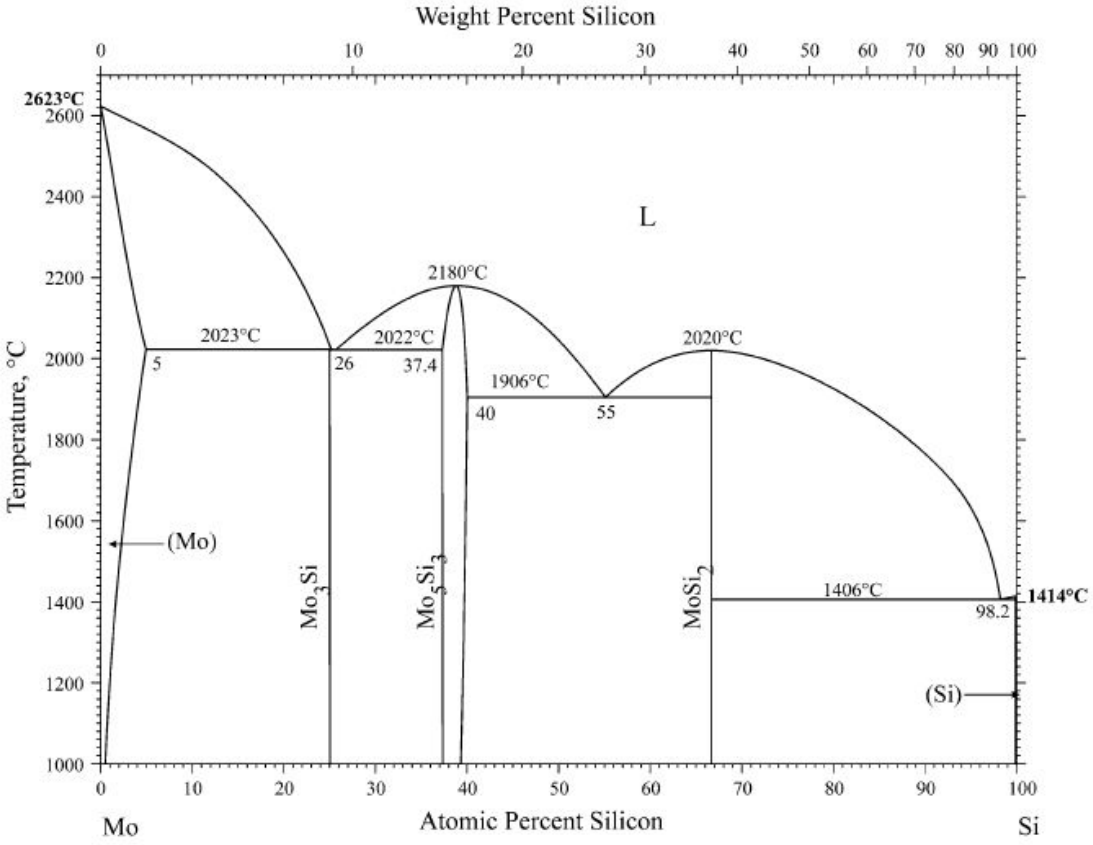


**Fig. 4.2 Mo-Si binary phase diagram [23].**

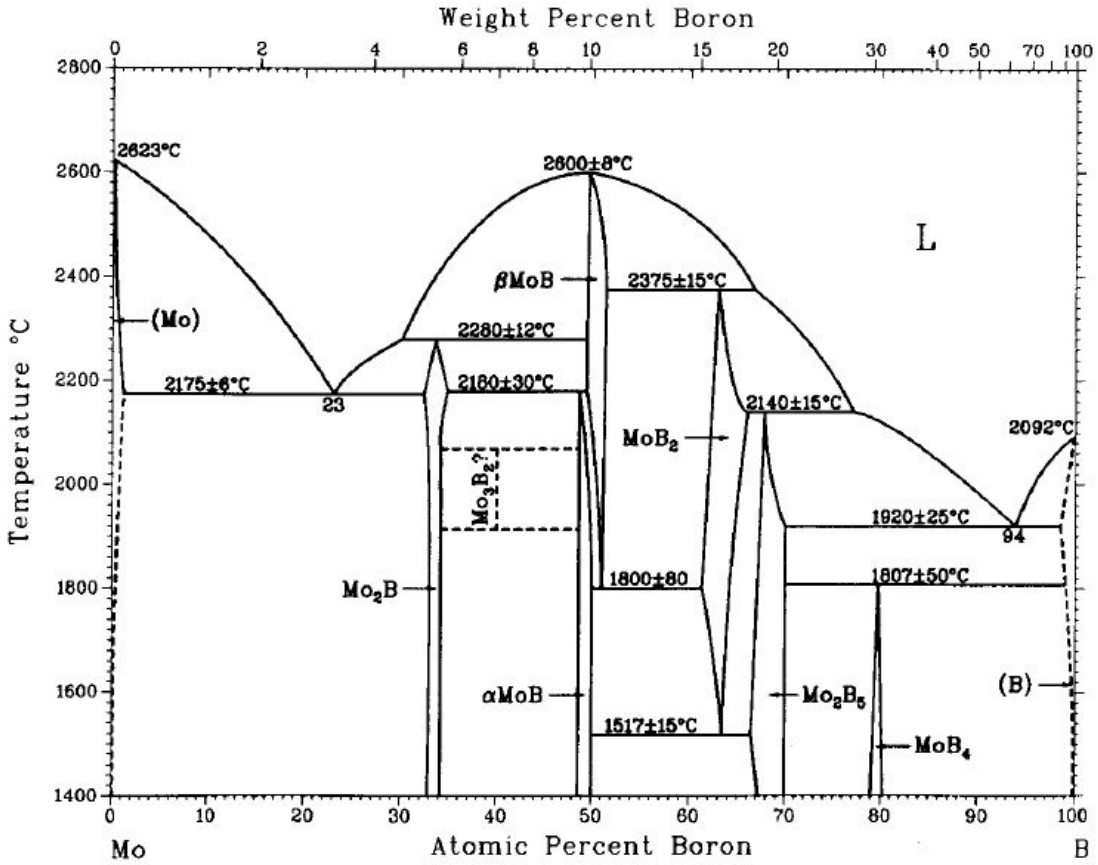


**Fig. 4.3 Mo-B binary phase diagram [23].**

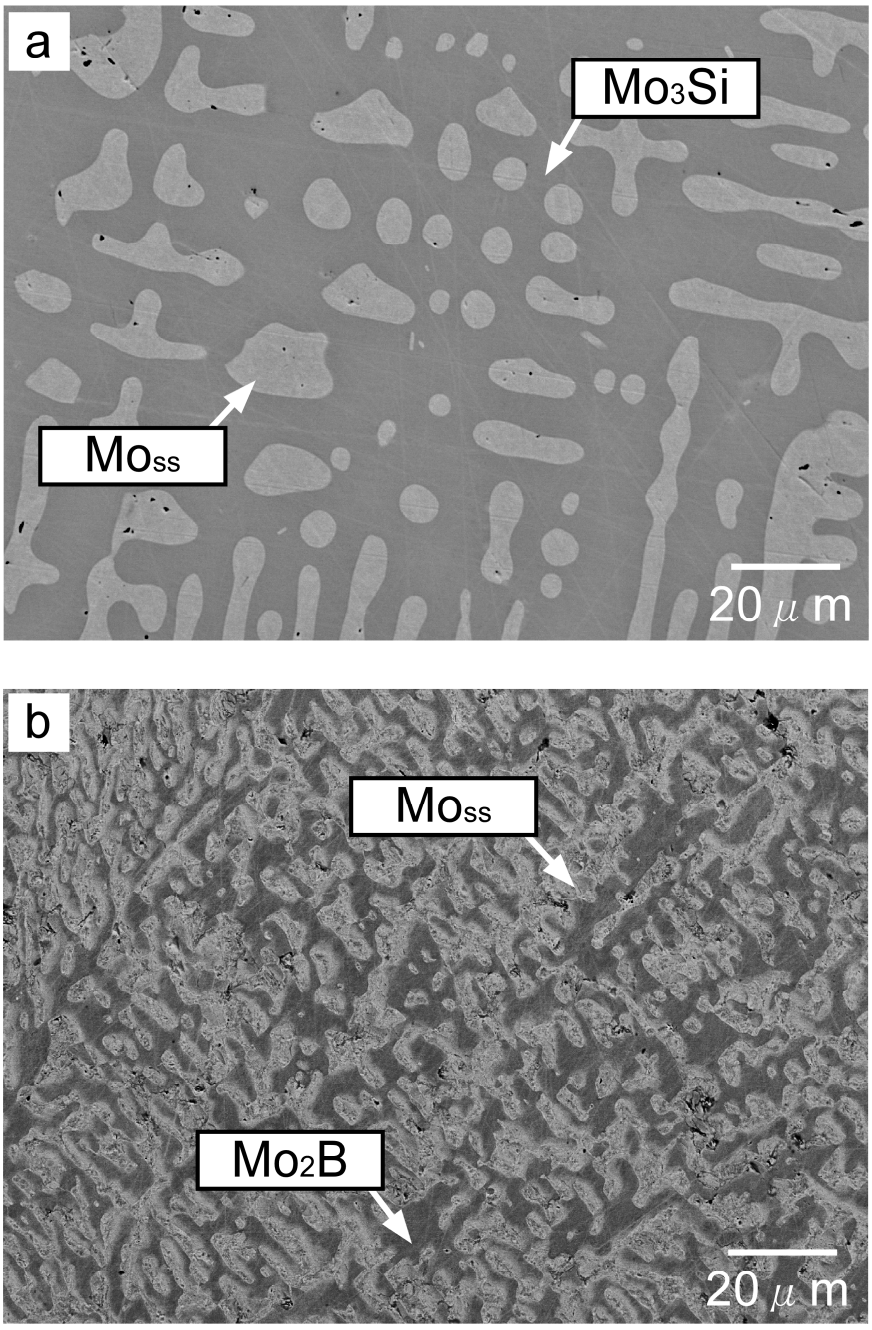


**Fig. 4.4 Microstructures after heat treatment at 1800 °C of (a) Mo-15Si (Alloy B1) and (b) Mo-20B (Alloy B4).**

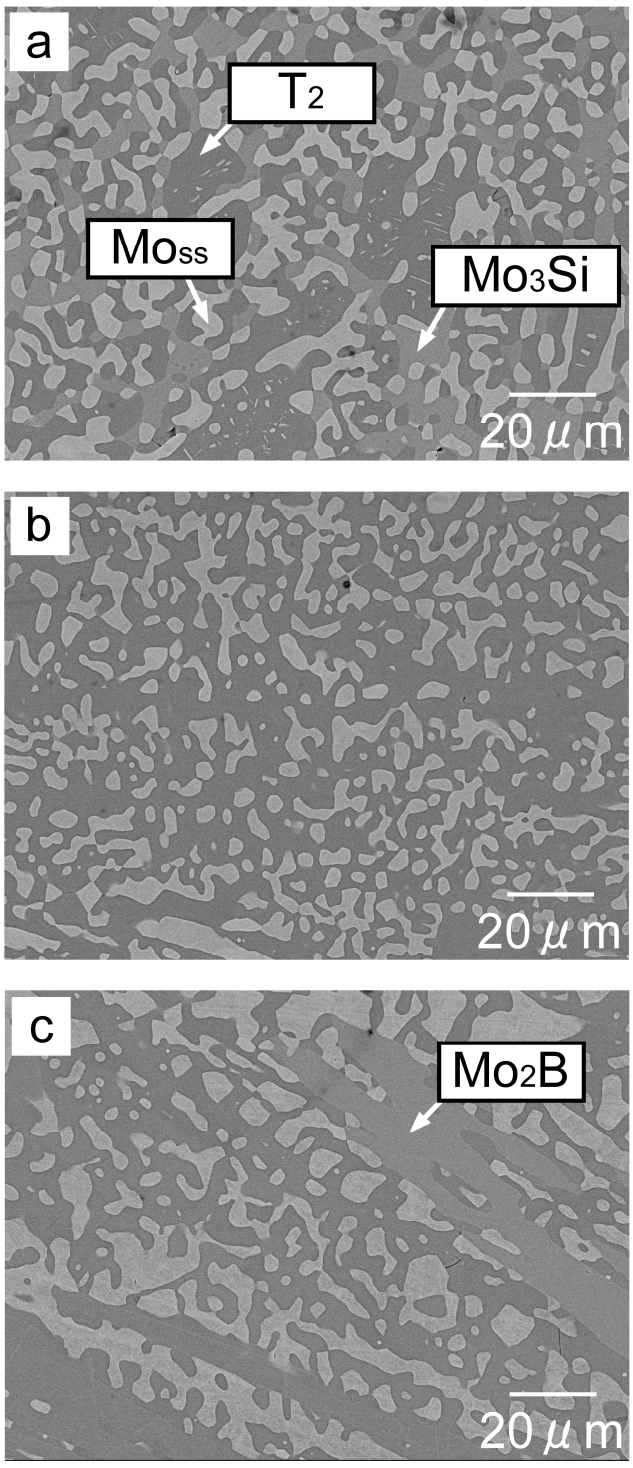


**Fig. 4.5 Microstructures after heat treatment at 1800 °C of (a) Mo-11.7Si-14.4B (Alloy T1), (b) Mo-8.7Si-17.4B (Alloy T2) and (c) Mo-5.7Si-20.4B (Alloy T3).**

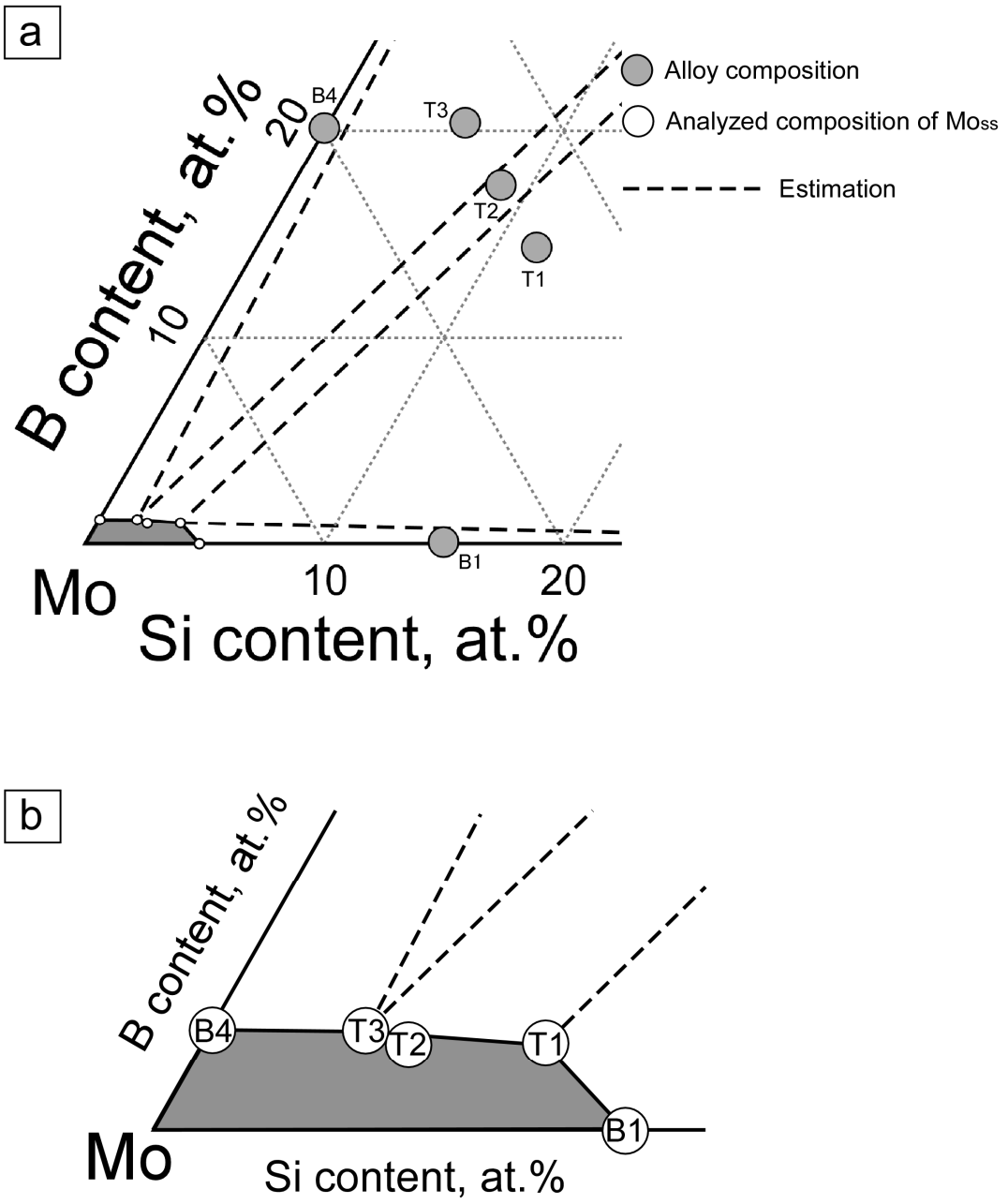


**Fig. 4.6 Determined $Mo_{ss}$ single phase region; (a) examined alloys and (b) expansion of the region.**

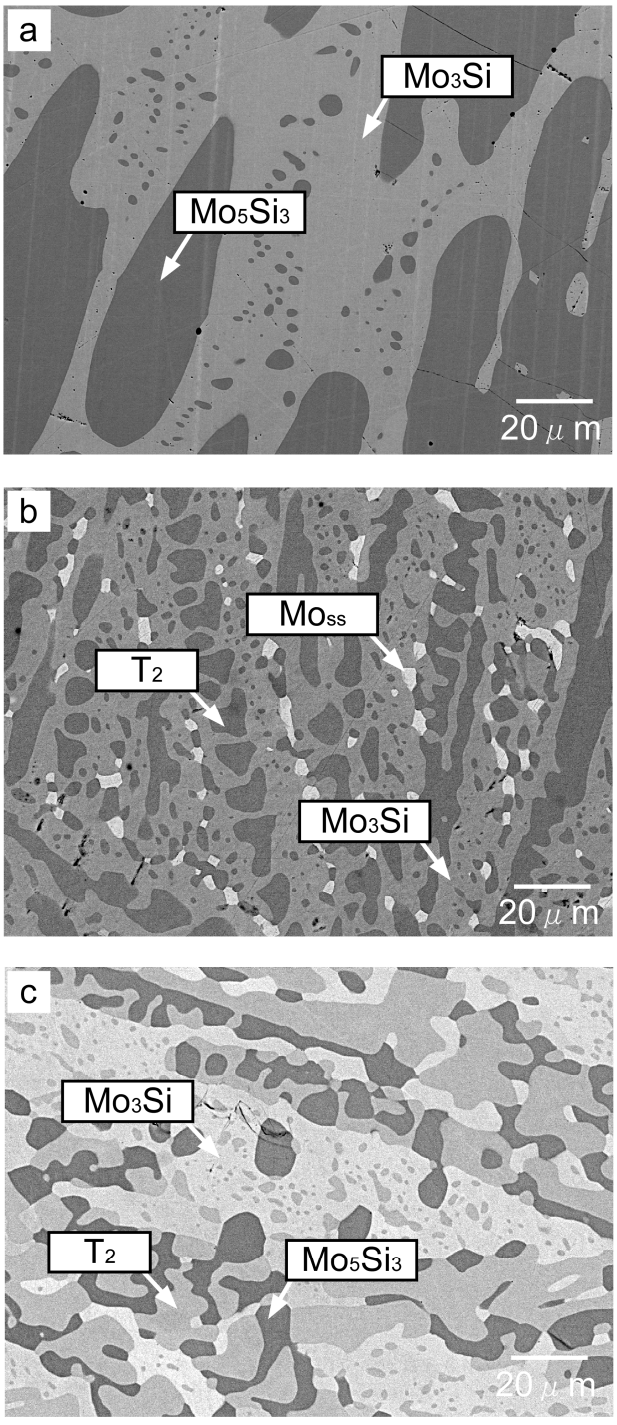


**Fig. 4.7 Microstructures after heat treatment at 1800 °C of (a) Mo-30Si (Alloy B2), (b) Mo-18Si-10B (Alloy T4) and (c) Mo-22Si-10B (Alloy T5).**

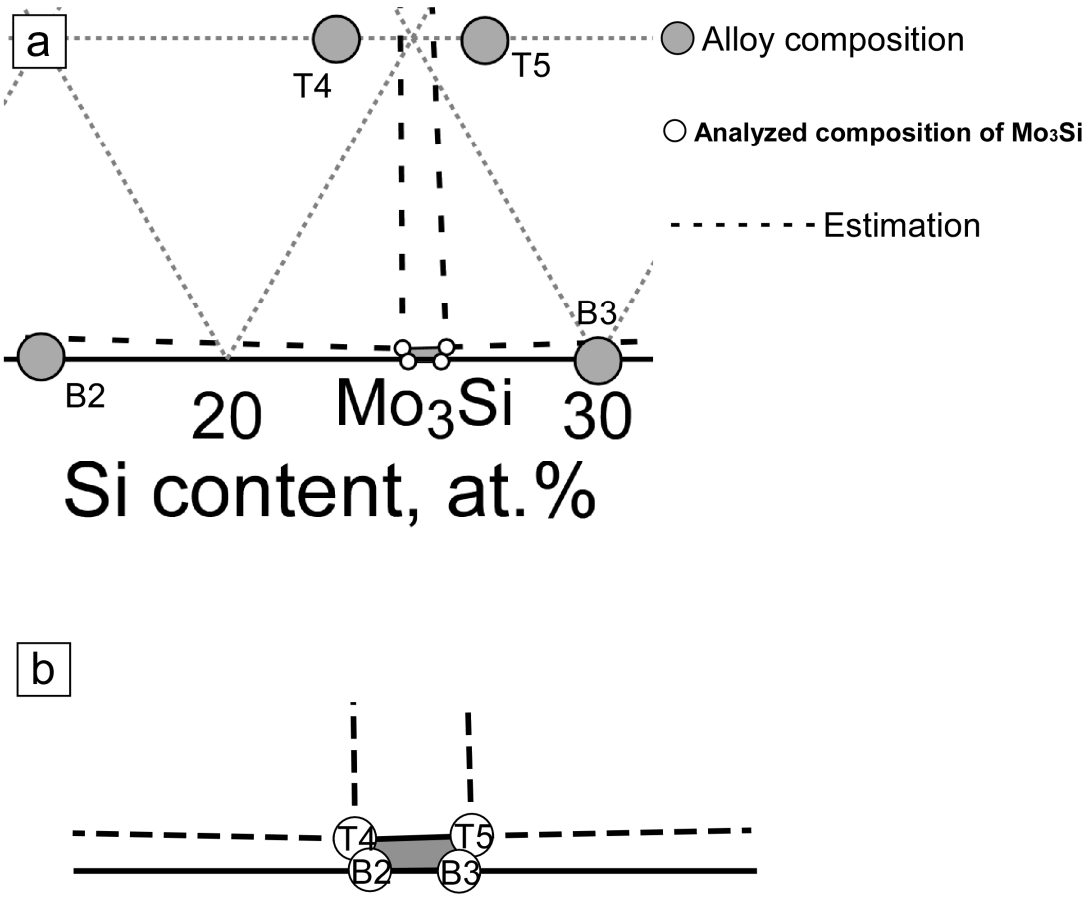


**Fig. 4.8 Determined $Mo_3Si$ single phase region; (a) examined alloys and (b) expansion of the region.**

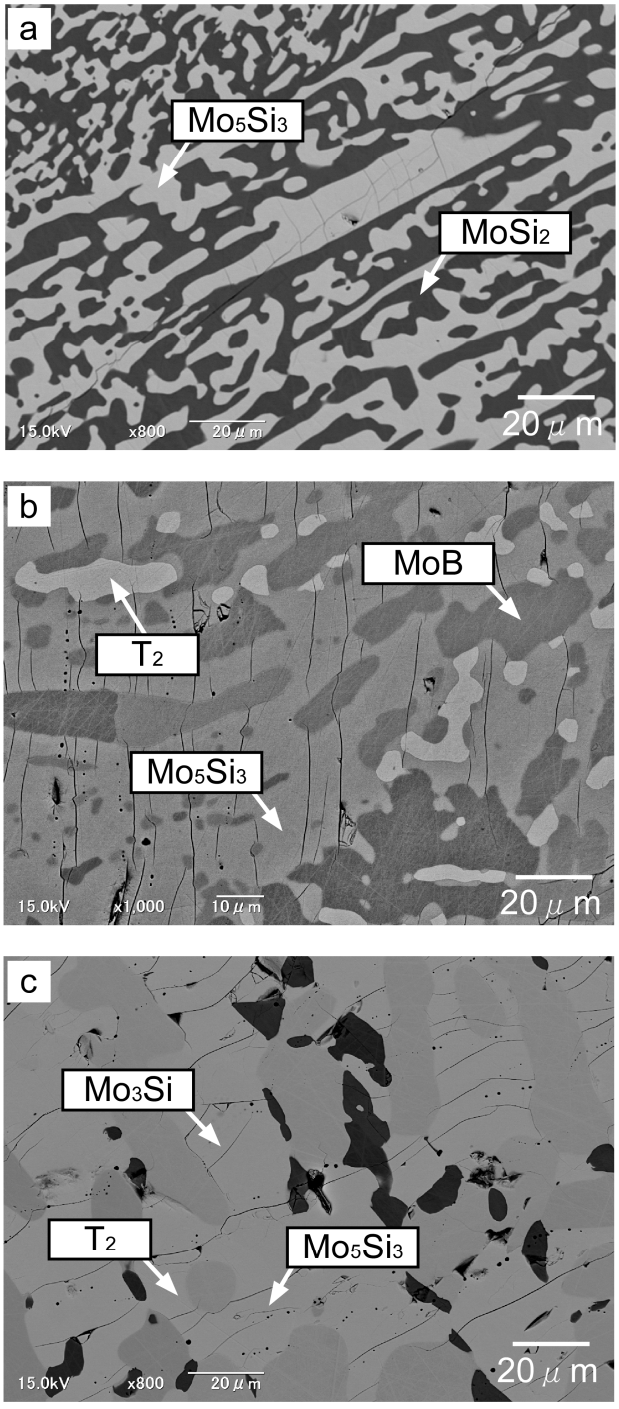


**Fig. 4.9 Microstructures after heat treatment at 1800 °C of (a) Mo-50Si (Alloy B3), (b) Mo-18Si-24.6B (Alloy T6) and (c) Mo-22Si-24.6B (Alloy T7).**

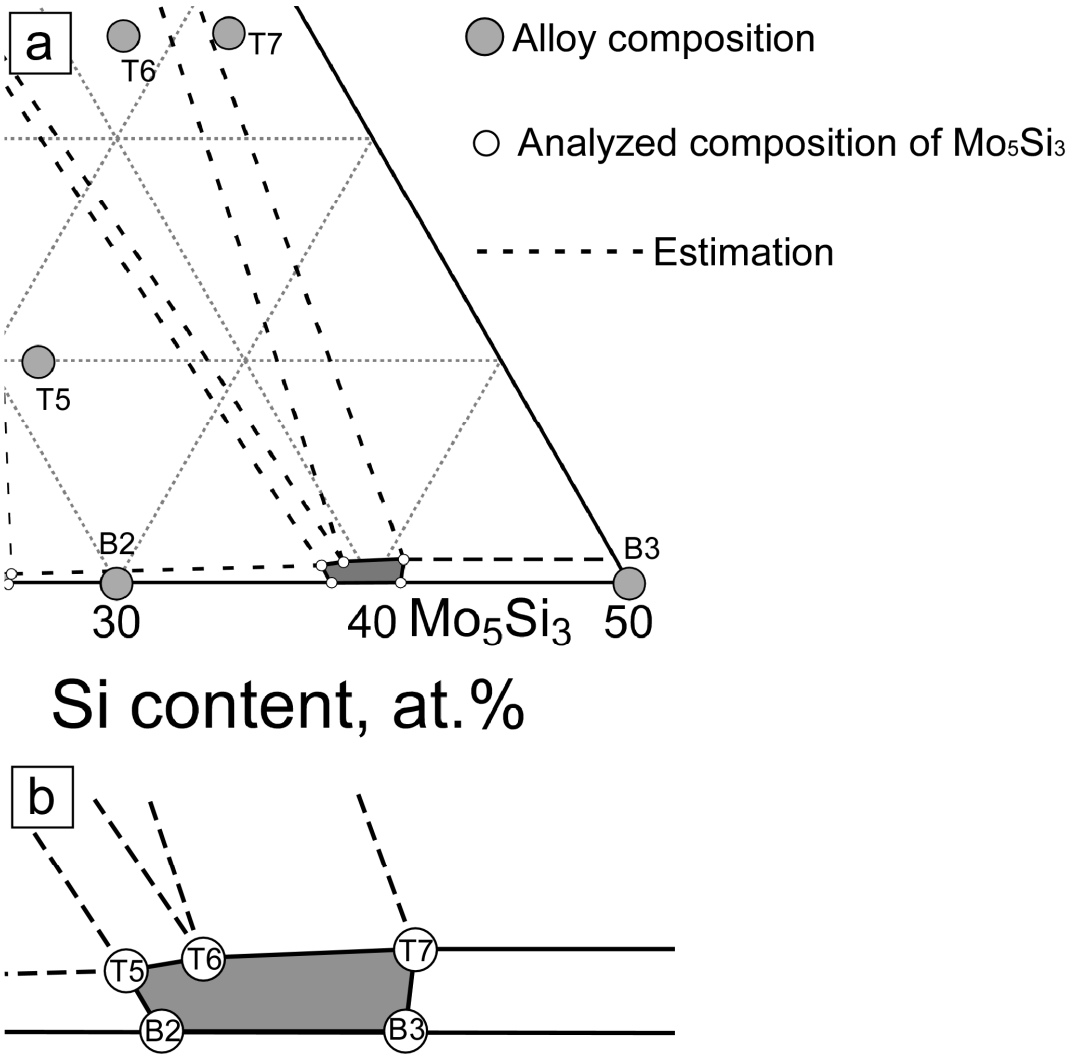


**Fig. 4.10 Determined $Mo_5Si_3$ single phase region; (a) examined alloys and (b) expansion of the region.**

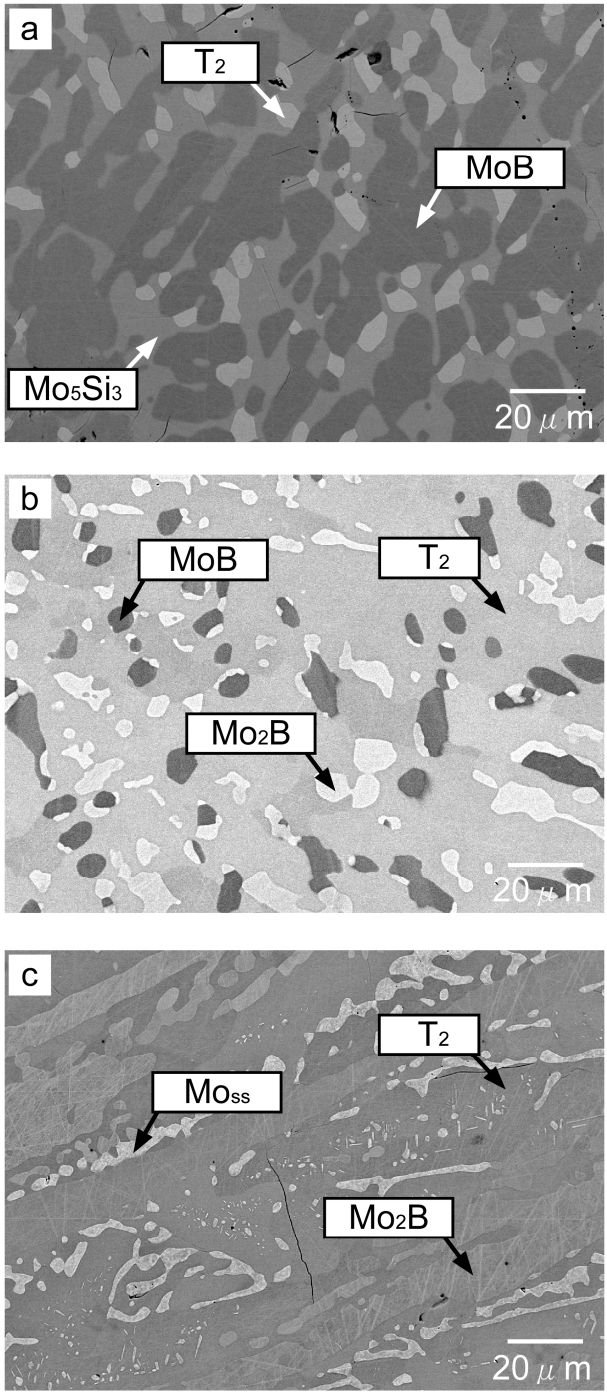


**Fig. 4.11 Microstructures after heat treatment at 1800 °C of (a) Mo-7.7Si-38.4B (Alloy T8), (b) Mo-6.2Si-33B (Alloy T10) and (c) Mo-6.2Si-27B (Alloy T12).**

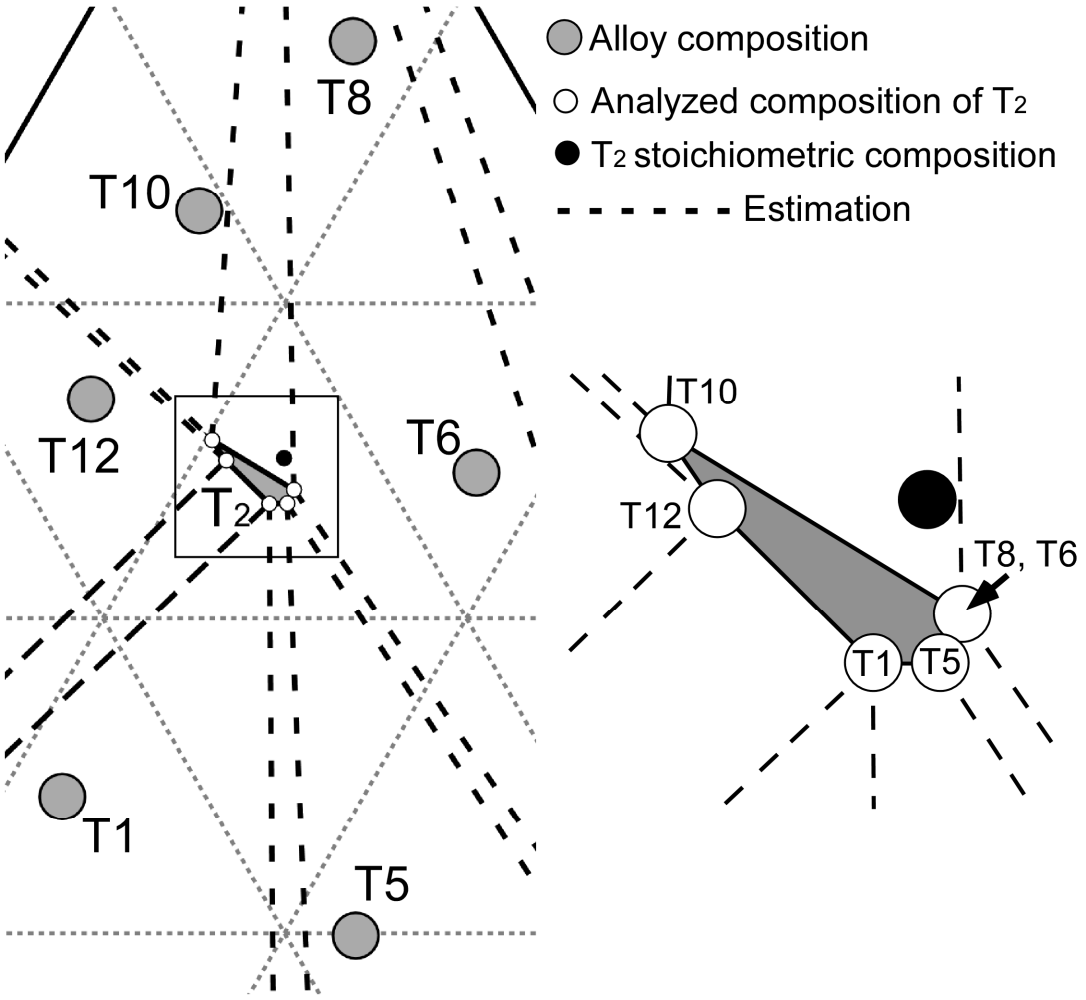


**Fig. 4.12 Determined $T_2$ single phase region.**

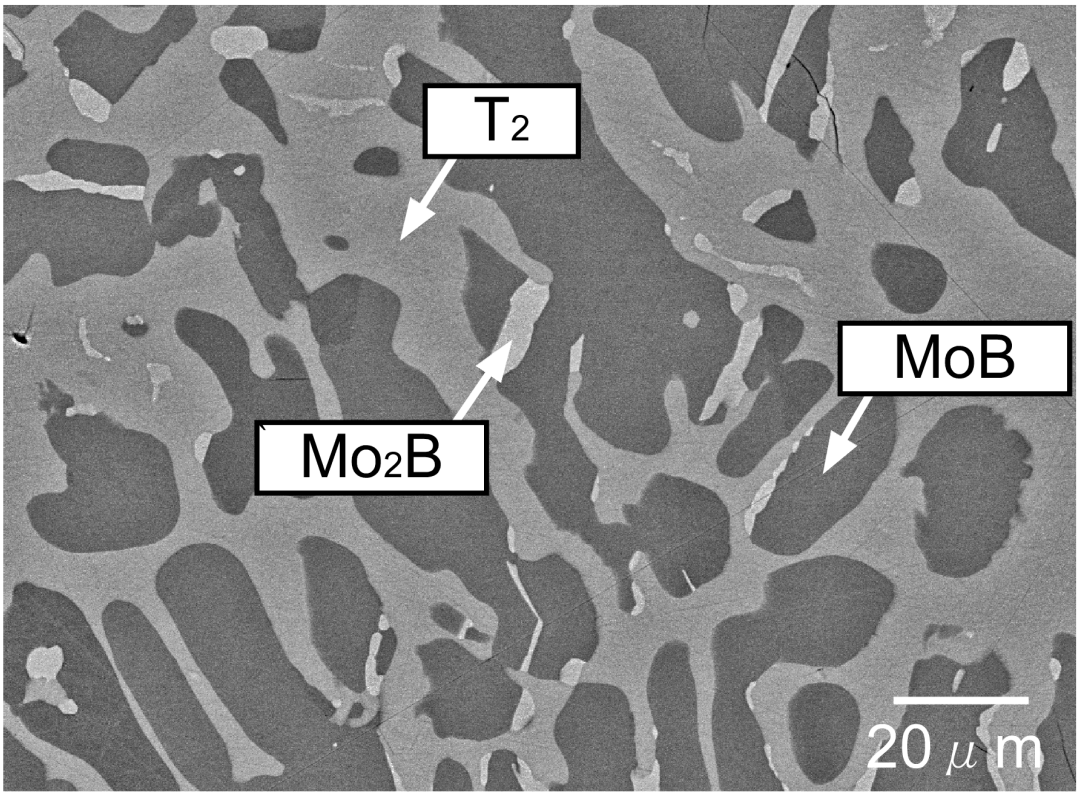


**Fig. 4.13 Microstructures after heat treatment at 1800 °C of Mo-3.7Si-38.4B (Alloy T9).**

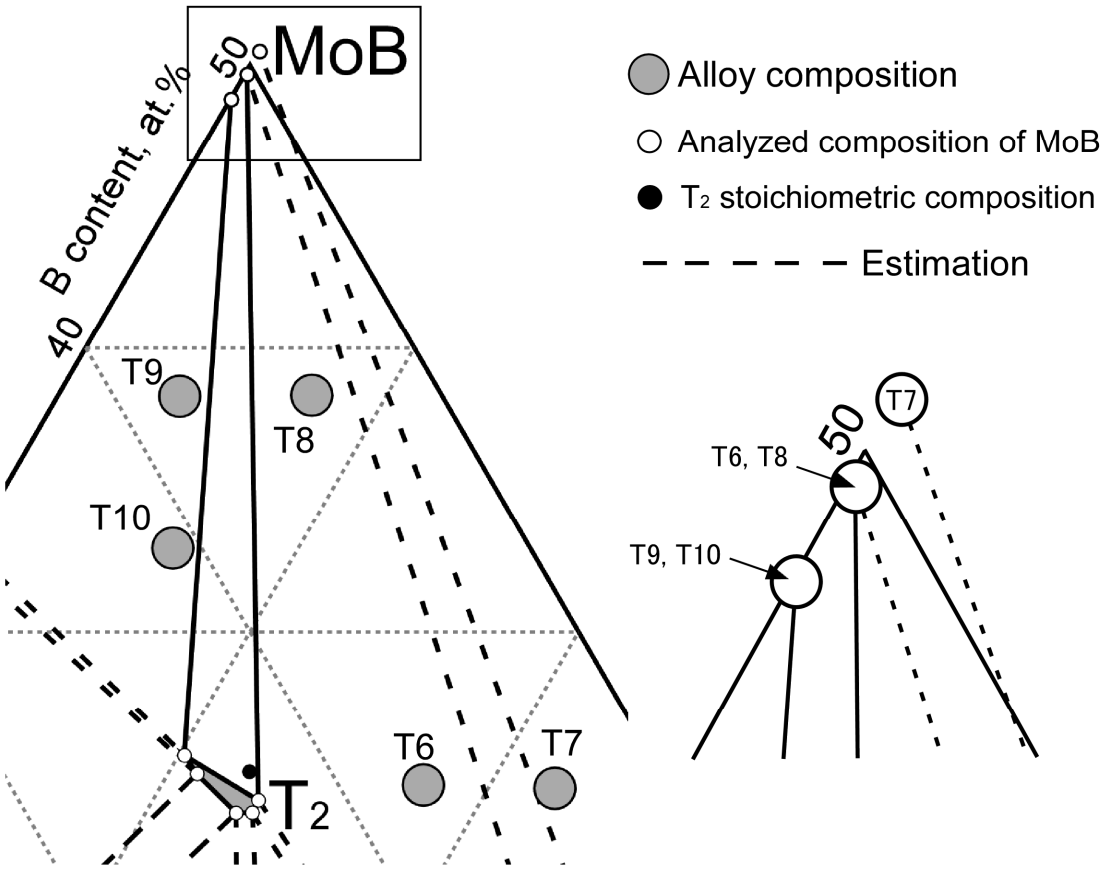


**Fig. 4.14 Determined MoB single phase region.**

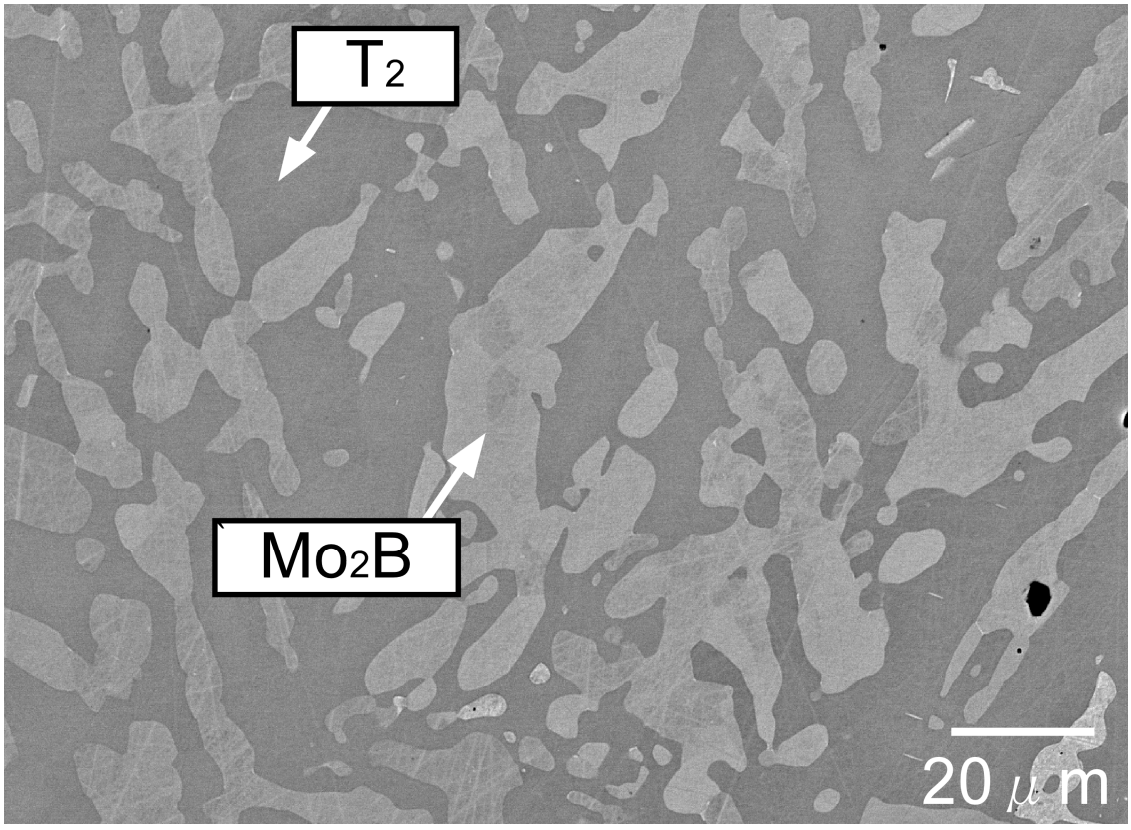


**Fig. 4.15 Microstructures after heat treatment at 1800 °C of Mo-6.2Si-30B (Alloy T11).**

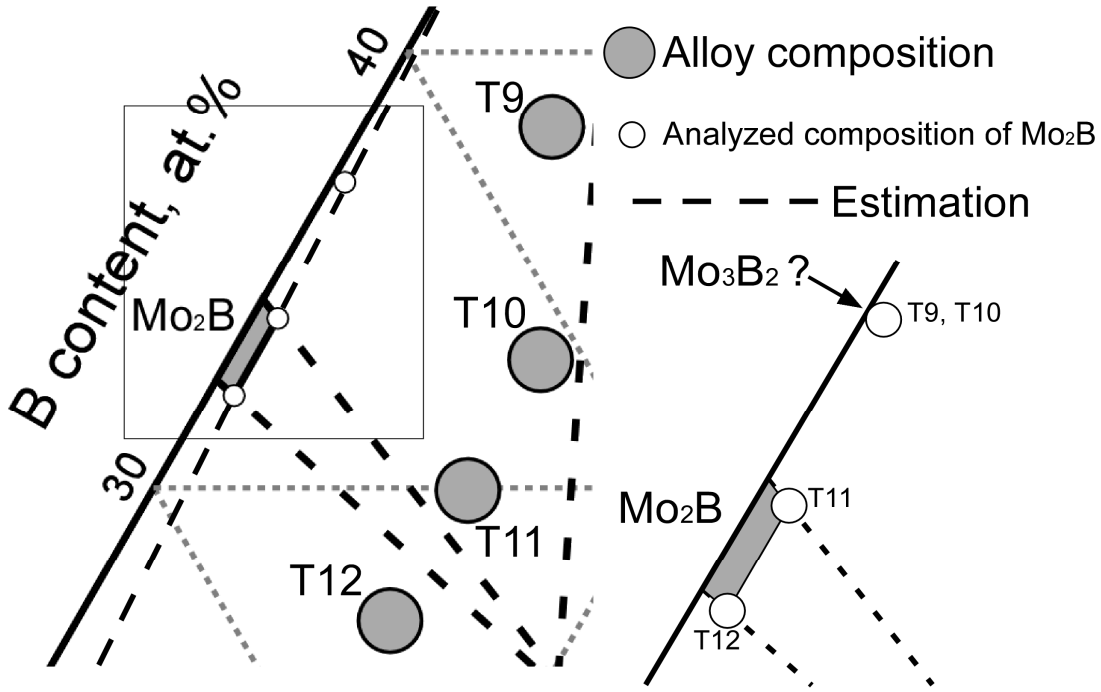


**Fig. 4.16 Determined $Mo_2B$ single phase region.**

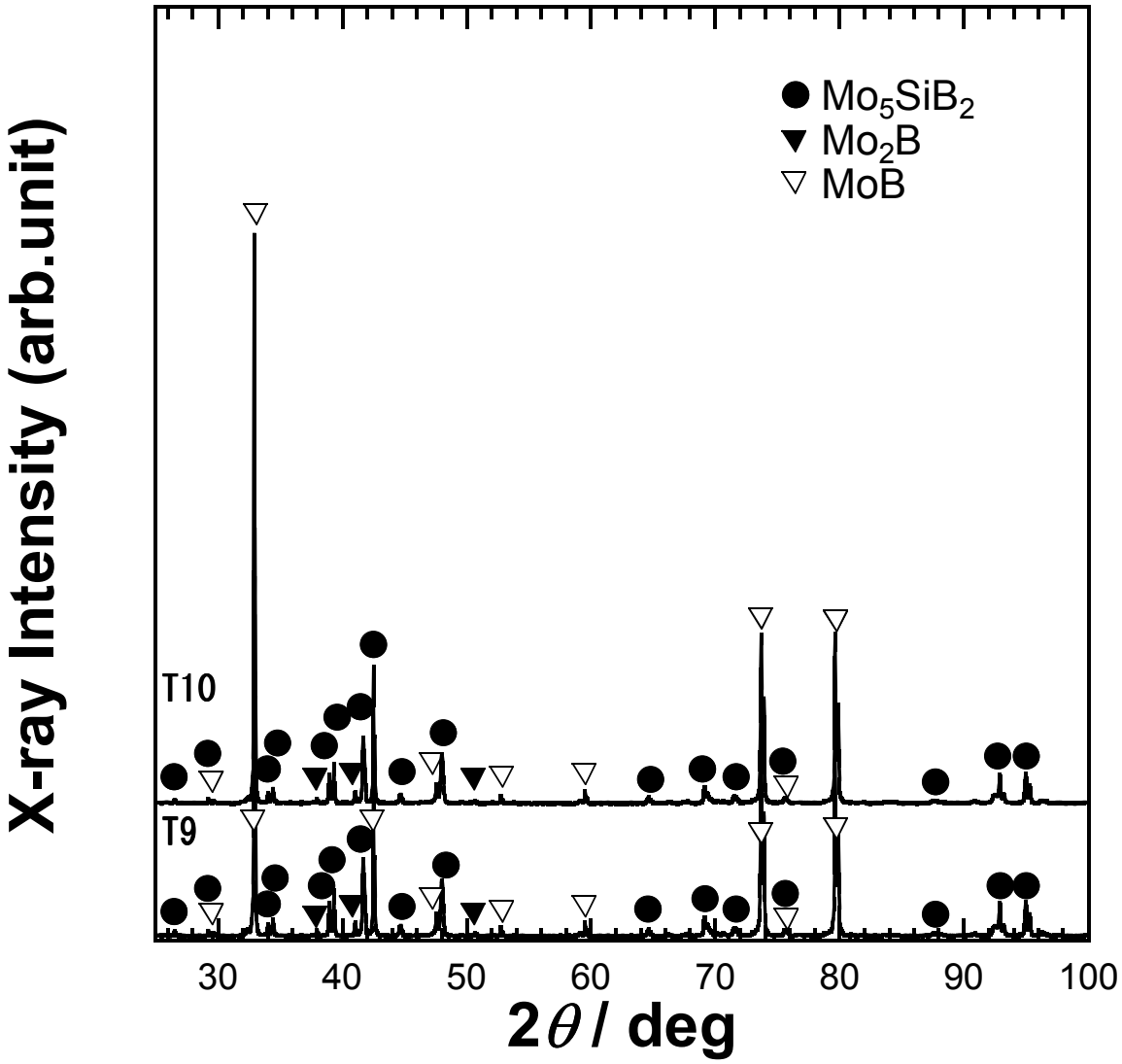


**Fig. 4.17 XRD patterns for Alloys T9 and T10.**

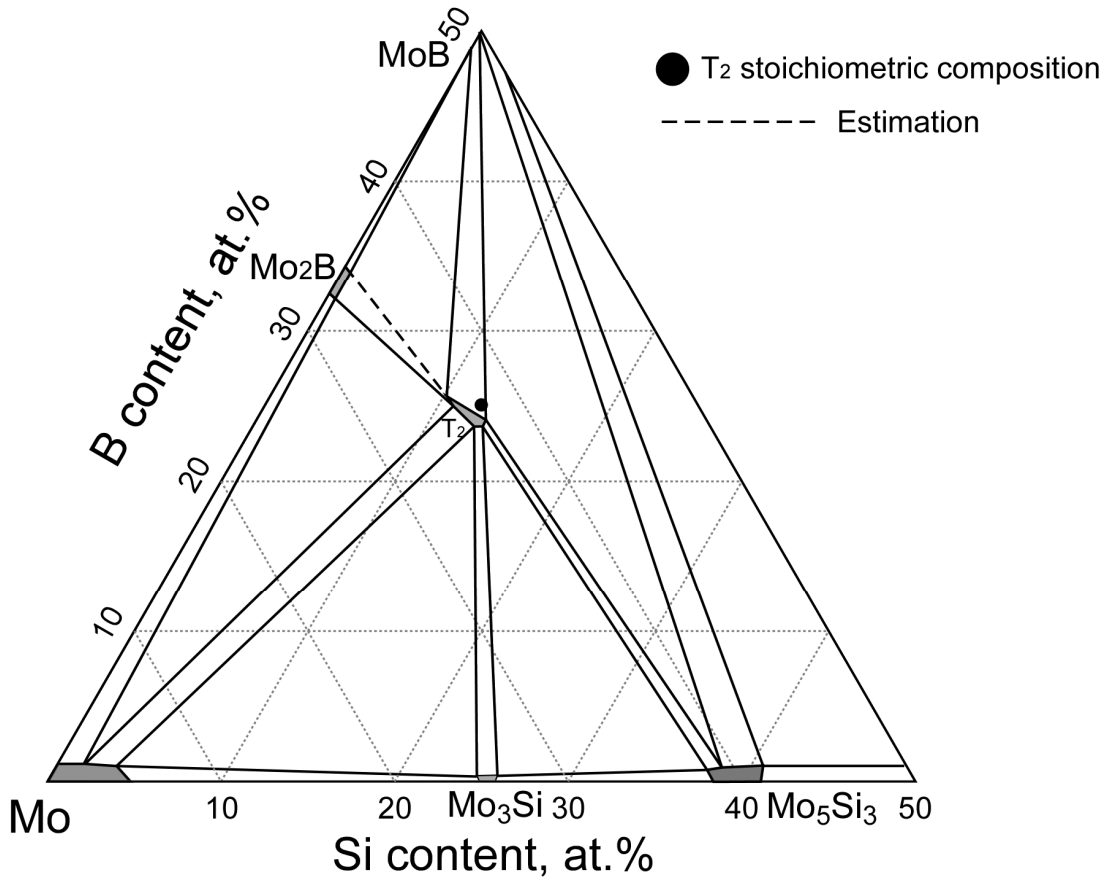


**Fig. 4.18 Isothermal phase diagram at 1800 ˚C in Mo-rich portion of Mo-Si-B system determined in this study.**

# CHAPTER 5

# Effect of TiC on Microstructure Formation and Phase Equilibrium of Mo-Si-B Ternary System

## 5.1. Introduction

Through Chapter 3 and 4, Mo-Si-B ternary system was mainly dealt in solidification route from liquid, microstructure change after the heat treatment and phase equilibrium at 1800 °C. The Mo-Si-B alloy has excellent strength and creep property at ultra-high temperature. However, the intermetallic phases are brittle; the room temperature fracture toughness values of $T_2$ phase are around 2-3MPa·$m^{1/2}$ [1]. As seen in Chapter 3 and 4, $T_2$ and $Mo_3Si$ have two or three-phase regions with ductile Mo. It improves greatly to the room temperature fracture toughness of $T_2$; the room temperature fracture toughness of $T_2$ increase with increasing $Mo_{ss}$ volume fraction and reach values as high as 21 MPa·$m^{1/2}$ [2].

On the other hand, the increase of $Mo_{ss}$ volume fraction induces rise of the alloy weight. As seen in Fig. 5.1, Mo has higher density than those of Ni and Nb. The alloy design should be considered to improve the fracture toughness and to keep or reduce the

weight, simultaneously. Transition metal carbide such as TiC, ZrC and HfC has been considered because of low density, their high hardness and thermal stability, as well as excellent creep and wear resistance [3-5]. In this chapter, TiC was employed to solve weight problem of the Mo-Si-B alloy. Eutectic point of Mo-TiC system was reported to exist at about 23.5mol% at 2175 °C (see Fig. 5.2) [6]. As described in chapter 3, the alloy composition is included in $Mo_{ss}$ primary region as $Mo_{ss}$ volume fraction increases up to about 50% in liquidus projection. This leads to the formation of coarse $Mo_{ss}$ in solidification and also, the distribution of coarser $Mo_{ss}$ by their combination during the heat treatment. Since Mo-TiC eutectic reaction occurs in Mo-richer area than that of $Mo_{ss}$-$T_2$, it is expected to disperse finely $Mo_{ss}$ phase through the combination of Mo-TiC and $Mo_{ss}$-$T_2$ two-eutectic phases. In this chapter, density change, microstructure formation and phase equilibrium at 1800 °C were investigated for TiC-synthesized Mo-Si-B alloys.

**5.2. Experimental Procedures**

In this study, 5 samples were prepared; 4 TiC-synthesized Mo-Si-B alloys and a Mo-Si-B ternary alloy for comparison. The nominal compositions of the samples prepared are shown in Table 5.1 and plotted in the phase diagram determined in this

study overlapped with liquidus projection of Yang et al. (Fig. 5.3) [7]. As seen in Fig. 5.3, TiC was added into the alloys included in $Mo_{ss}$ primary region of the liquidus projection by Yang et al. [7]. The button ingots of Mo-Si-B alloys approx. 20 g in weight were produced by a conventional arc-melting technique from pure Mo (99.9 wt.%), Si (99.9999 wt.%) and B (99.95 wt.%) with a water-cooled copper crucible under an Ar atmosphere. And then, cold-pressed TiC powders were arc-melted with the prepared Mo-Si-B ternary alloys. The chemical composition of the employed TiC powders was shown in Table 5.2. Each of the alloy ingots was flipped and re-melted more than 5 times maximally to achieve compositional homogeneity. Prior to each melting, the furnace was evacuated and filled with high-purity Ar gas several times. A pure Ti ingot was melted before every melting to remove residual $O_2$ and $N_2$ gases. There was no great difference in alloy weight between before and after melting. Specimens were taken from the center of the ingots and prepared for chemical analysis and microstructure observation. The atomic ratios of Mo, Si and B in the as-cast alloys were analyzed by inductively coupled plasma (ICP) – the optical emission spectrometry (OES) method [8]. The density was measured 5 times with micromeritics gas pycnometer accupyc and the values were obtained from the averages. The microstructures of the samples were observed by scanning electron microscopy (JEOL

JSM-6500F) with back scattered electron (BSE) images and the constituent phases were identified by X-ray diffractometry (XRD) (Bruker D-8 Advance). The quantitative composition analysis for constituent phases was performed by electron probe micro-analysis (EPMA) (JEOL JXA-8621MX). An additional work for Ti and C was not performed for the EPMA calibration in this study. Thus, the results for EPMA measurement wouldn't be as accurate as that for the Mo-Si-B ternary alloys. The hardness of constituent phases was measured by nano-indentation. EBSP analysis was performed to grasp the volume fraction of constituent phases.

## 5.3. Results and Discussion

### 5.3.1 Microstructure Examination

The as-cast microstructure change with increasing TiC content is shown in Fig. 5.5. Mo-7.3Si-14.6B alloy shows the distribution of primary $Mo_{ss}$ in the form of dendrite since its composition is included in that of $Mo_{ss}$ primary region. And also, $Mo_2B$ exists between dendrite $Mo_{ss}$ particles by sudden change of the composition to B-rich after the formation of primary $Mo_{ss}$ because the alloy composition is located near the border between $Mo_{ss}$ and $Mo_2B$ primary regions. There also exists $Mo_{ss}$-$T_2$ and $Mo_{ss}$-$Mo_3Si$-$T_2$ eutectic phases as those of the alloys examined in chapter 3. On the other hand, after

TiC addition, the existence of primary TiC and coarse $T_2$ was observed. The volume fraction of primary TiC and $T_2$ rises with increasing TiC content. Fine eutectic phases were also observed and expected to be $Mo_{ss}$-$T_2$ and $Mo_{ss}$-TiC-$T_2$ eutectic phases in BSE contrast. The as-cast microstructure change with increasing Mo/Si-B ratio in 15at%TiC addition is shown in Fig. 5.6. It is seen that the volume fraction of primary TiC increased and the $T_2$ is refined with the composition change to Mo-rich. $Mo_{ss}$-TiC eutectic phase was formed as primary in C4 alloy, which has Mo-richest composition in the alloys. Considering the ratio of Mo, Si and B, the primary should be coarse $Mo_{ss}$. However, after TiC addition, $Mo_{ss}$ was finely distributed by $Mo_{ss}$-TiC eutectic phase formation as primary.

The microstructure change with increasing TiC content after heat treatment at 1800 °C is shown in Fig. 5.7. In the microstructure of Mo-7.3Si-14.6B alloy, more coarsened $Mo_{ss}$ was observed by the combination between primary $Mo_{ss}$ particles. In TiC-synthesized alloys, primary TiC remains and the distribution of continuous $Mo_{ss}$ was observed after the heat treatment. The microstructure change with increasing Mo content in 15at%TiC addition after heat treatment at 1800 °C is shown in Fig. 5.8. With increasing Mo/Si-B content, the volume fraction of continuous $Mo_{ss}$ increased and also, fine TiC particles were distributed in the $Mo_{ss}$. Especially, the microstructure of C4

alloy appears to consist of $Mo_{ss}$ as matrix phase, and TiC and $T_2$ as dispersed phase. The results of quantitative analysis by EPMA for $Mo_{ss}$, $T_2$ and TiC are shown through Fig. 5.9, 5.10 and 5.11. It was confirmed that a certain amount of Ti and Si was dissolved in $Mo_{ss}$ (see Fig. 5.9). With increasing the Ti content in $Mo_{ss}$, the Si content was decreased. $T_2$ phase also has Ti concentration of about 10at% after TiC addition (see Fig. 5.10). A large amount of Mo (about 30at%) was dissolved in TiC as shown in Fig. 5.11. The solubility of Ti and Mo obtained in this study appears to be larger than that of the Mo-TiC phase diagram shown in Fig. 5.2 [6]. This would be attributed to the use of inappropriate standard samples.

### 5.3.2 Expectation for Fracture Toughness

The density of the alloys is shown in Fig. 5.4. The gray box shows the measured values and the hatched box does the calculated values. The density of pure Ni was referred and expressed as dotted line. In the calculated density, most of the alloys show the values lower than that of pure Ni, while the measured value is higher than that of pure Ni in the case of Mo-7.3Si-14.6B alloy. With TiC addition, the density was reduced and especially, both of the measured and calculated values are lower than that of pure Ni in C2 and C3 alloys. Therefore, it was confirmed that weight reduction was achieved by TiC addition. The solubility dependence of $Mo_{ss}$, $T_2$ and TiC on hardness by

nanoindentation is shown in Fig. 5.12. In $Mo_{ss}$, it was considered that there was no significant change in hardness. The increase of solubility in $Mo_{ss}$ leads to the improvement of the strength, but also the reduction of the ductility. However, from the result for $Mo_{ss}$, it was thought that there would be no considerable change in the ductility of $Mo_{ss}$ after TiC addition. In the $T_2$ and TiC, the increased values were observed from C1 to C3 alloy, while the hardness appeared to be reduced in C4 alloy. Since there was no visible change of the solubility in EPMA results, this doesn't appear to be related to Ti or Mo solubility. The phase volume fractions obtained from EPSP analysis are shown in Fig. 5.13. Alloy C3 has the $Mo_{ss}$ of 43.6%, $T_2$ of 27.5% and TiC of 29%. The interesting this is that C4 alloy showed the $Mo_{ss}$ of about 60% and $T_2$ and TiC of 40%, even though its density was the same level as that of pure Ni. Therefore, the fracture toughness of C4 alloy can be expected with the phase volume fraction, referring to the fracture toughness dependence of $Mo_{ss}$ volume fraction suggested by Kruzic et al. [9] (see Fig. 5.14). As seen in the figure, Mo-Si-B alloy had about 12 $MPa \cdot m^{1/2}$ in fracture toughness when the volume fraction of $Mo_{ss}$ was about 50%. Since the alloy system investigated in the study by Kruzic et al. [9] was based on the $Mo_{ss}$-$Mo_3Si$-$T_2$ three-phase, immediate comparison with C4 alloy in this study is difficult. However, C4 alloy is expected to have higher fracture toughness, simply

depending on the volume fraction of the $Mo_{ss}$. In addition, considering the density of C4 alloy is similar to that of pure Ni, it can be thought that TiC addition into Mo-Si-B ternary alloy met the toughening and the weight reduction, simultaneously.

## 5.4. Conclusions

In this chapter, density change, microstructure formation and phase equilibrium at 1800 °C were investigated for TiC-synthesized Mo-Si-B alloys. The conclusions are listed as following.

(1) With TiC addition, the density of Mo-Si-B alloys was reduced to a level lower than that of pure Ni.

(2) In as-cast microstructures, Mo-7.3Si-14.6B alloys showed coarse primary $Mo_{ss}$, while TiC or $Mo_{ss}$-TiC eutectic appeared as primary by TiC addition. $Mo_{ss}$ particles in TiC added alloys were refined by the formation of TiC or $Mo_{ss}$-TiC eutectic as primary and $Mo_{ss}$-$T_2$-TiC three-phase eutectic.

(3) After heat treatment at 1800 °C, the microstructure of Mo-7.3Si-14.6B consisted of $T_2$ and coarse $Mo_{ss}$ particles formed from the combination of primary $Mo_{ss}$, while TiC added alloys showed the uniform distribution of fine TiC particles and $Mo_{ss}$ continuous phase.

(4) From EBSP result and the density, it was confirmed that Mo-3.4Si-6.8B-15TiC alloy had about 60 % $Mo_{ss}$ in volume fraction and the density comparable with that of pure Ni, simultaneously.

(5) Mo-Si-B alloy having 50 % $Mo_{ss}$ in volume fraction showed the fracture toughness of 12 $MPa \cdot m^{1/2}$ according to a previous report. Therefore, it is suggested that Mo-3.4Si-6.8B-15TiC alloy may have a value higher than 12 $MPa \cdot m^{1/2}$ in fracture toughness.

**References**

[1] Mitra R. Intl Mater Rev 2006;**51**:13-64.

[2] Sturm D, Heilmaier M, Schneibel JH, J´ehanno P, Skrotzki B, Saage H. Mater Sci Eng A 2007;**463:** 107-114.

[3] Kurishita H, Shiraishi J, Matsubara R, Yoshiaga H. J Jpn Inst Met 1985;**49**:963-971.

[4] Suzuki T, Nomura N, Yoshimi K, Hanada S. Mater Trans JIM 2000;**41**:1164-1167.

[5] Suzuki T, Matsumoto H, Nomura N, Yoshimi K, Hanada S. Trans Mater Res Soc Jpn 2001;**26**:307-310.

[6] Cedat D, Rey C, Clavel M, Schmitt JH, Le Flem M, Allemand A. J Nucl Mater 2009;**385**:533–537

[7] Yang Y, Chang YA. Intermetallics 2005;**13:**121-128.

[8] Danzaki Y, Wagatsuma K, Syoji T, Yoshimi K. Fresenius J Anal Chem 2001;**369:**184-186.

[9] Kruzic JJ, Schneibel JH, Ritchie RO. Scripta Materialia 2004;50:459-464.

**Table 5.1 Nominal compositions of the employed alloys.**

| Alloy no. | Nominal Composition (at%) | | |
|---|---|---|---|
| | Si | B | TiC |
| Ternary | 7.3 | 14.6 | |
| C1 | 6.6 | 13.1 | 10 |
| C2 | 6.2 | 12.4 | 15 |
| C3 | 5.1 | 11.1 | 15 |
| C4 | 3.4 | 6.8 | 15 |

**Table 5.2 Measured composition of the employed TiC powder.**

| Sample | Measured Composition (at%) | | | H Content (ppm) |
|---|---|---|---|---|
| | Ti | C | O | |
| TiC | 48.89 | 50.18 | 0.91 | 56 |

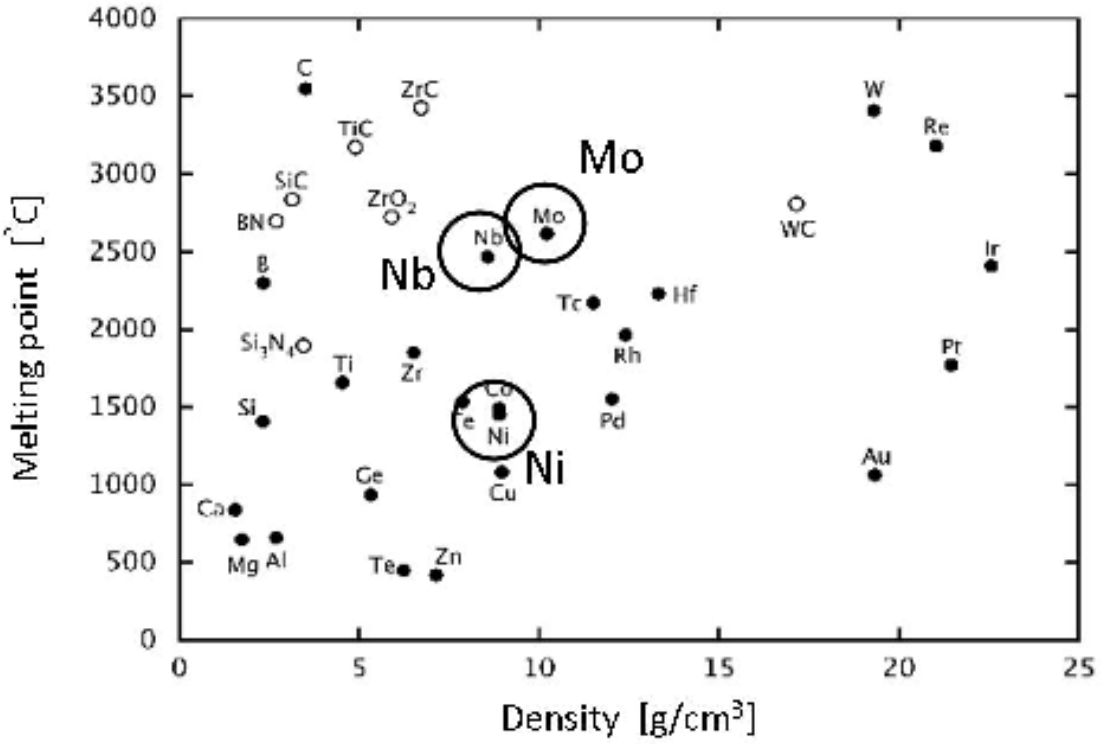


**Fig. 5.1 Density and melting point of each metal and ceramic.**

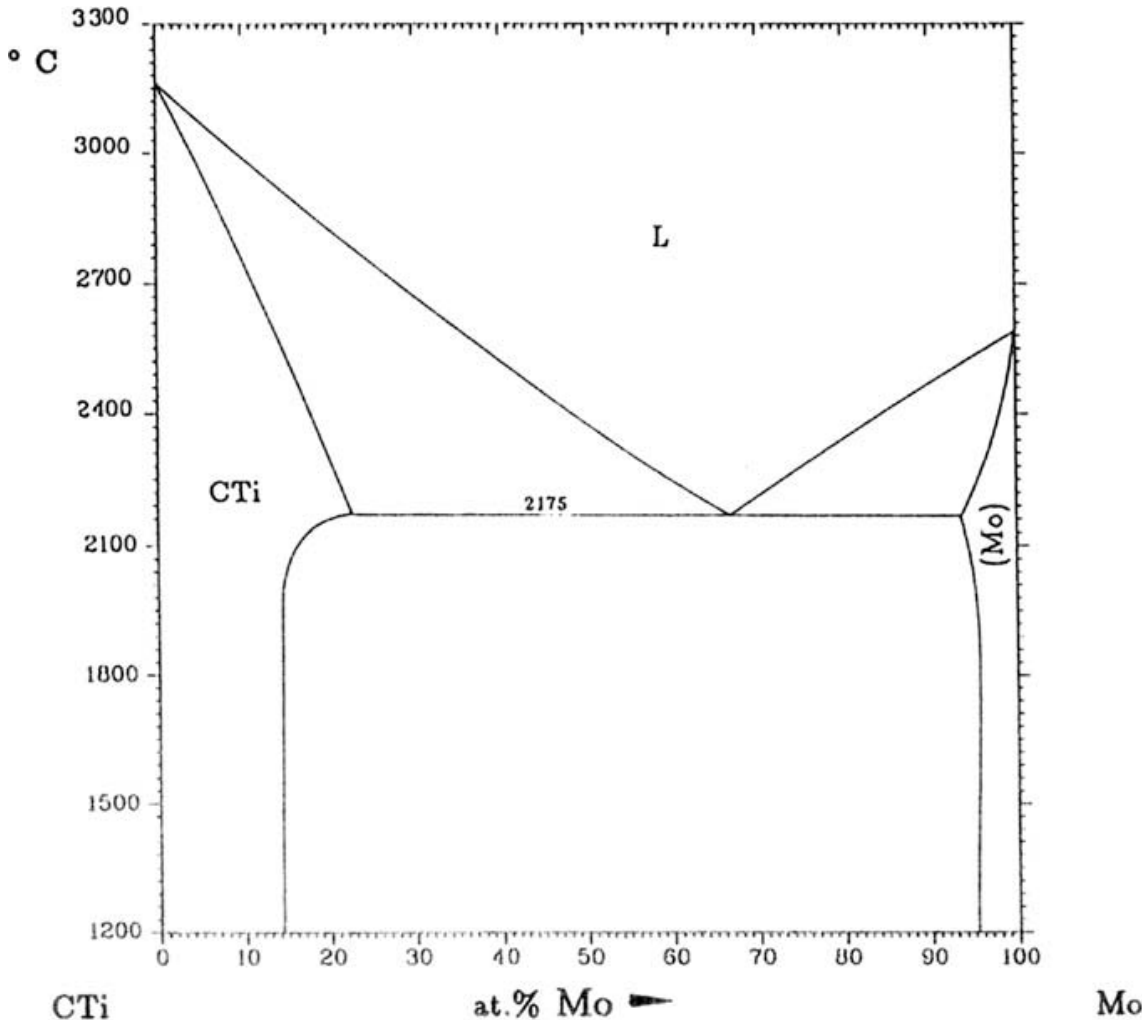


**Fig. 5.2 Phase diagram of Mo-Ti-C suggested by Cedat et al. [6].**

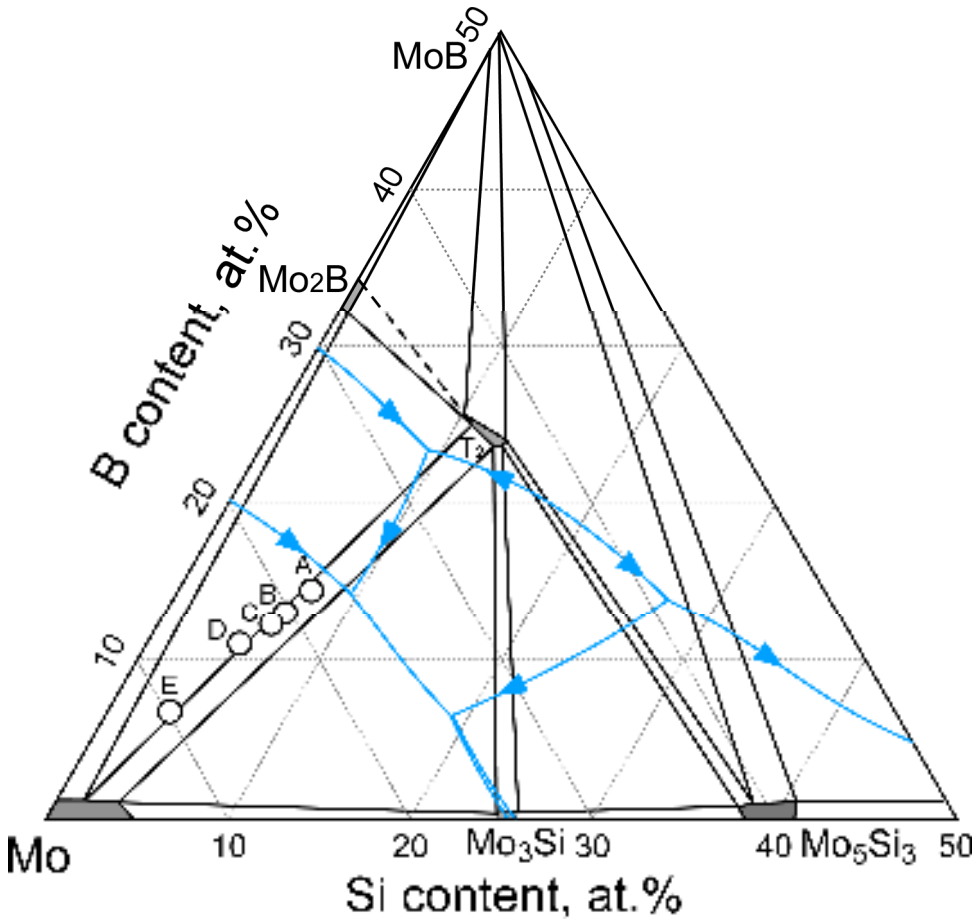


**Fig. 5.3 Nominal composition of the examined alloys with phase diagram at 1800 ° C determined in this study and liquidus projection of Yang et al. [7].**

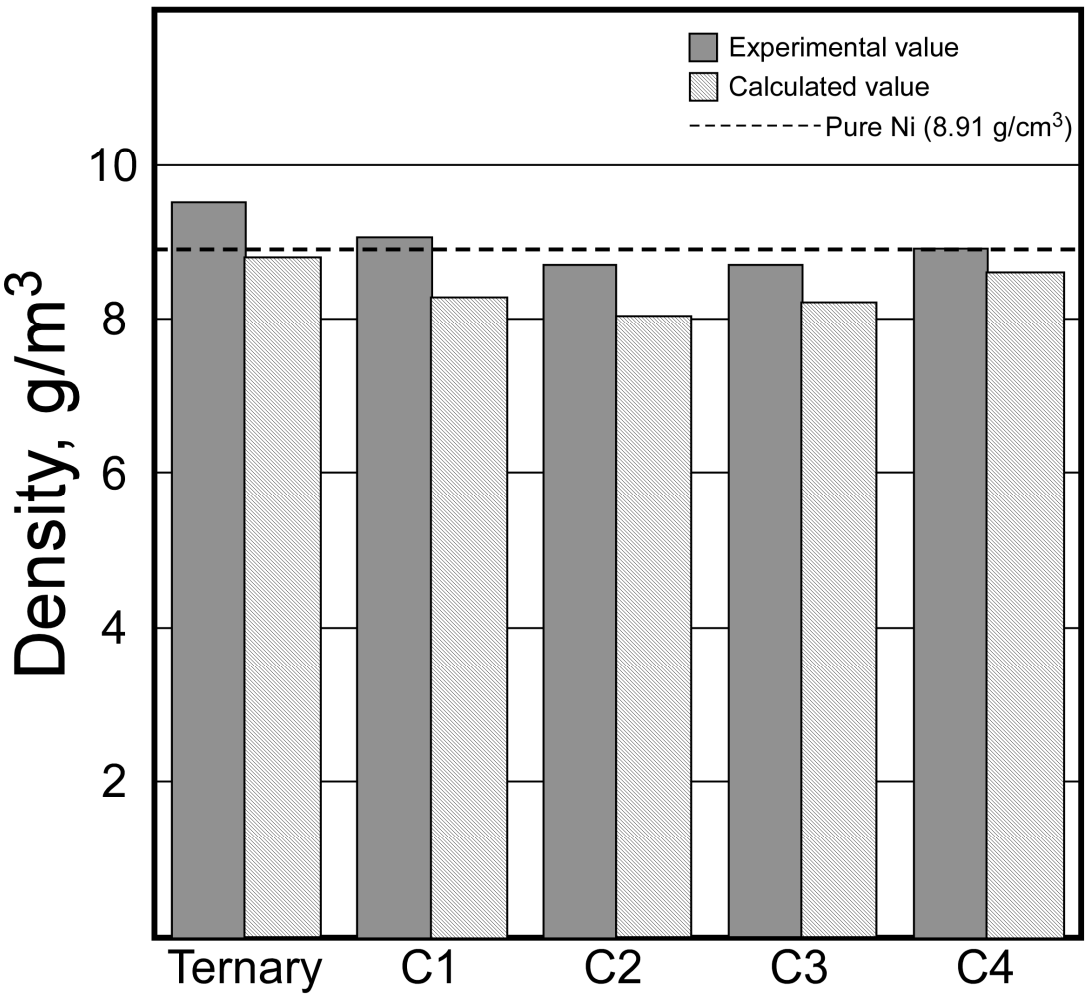


**Fig. 5.4 Density of the examined alloys.**

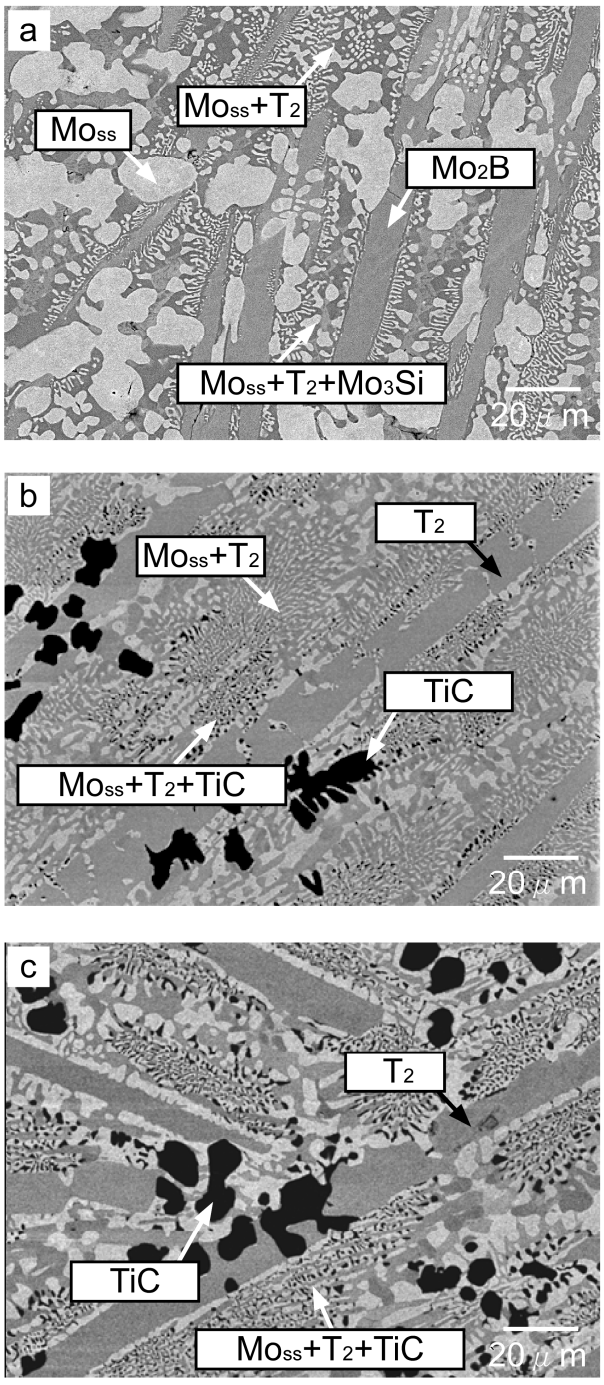


**Fig. 5.5 Microstructure change with increasing TiC content; (a) Ternary, (b) C1 and (c) C2 alloys.**

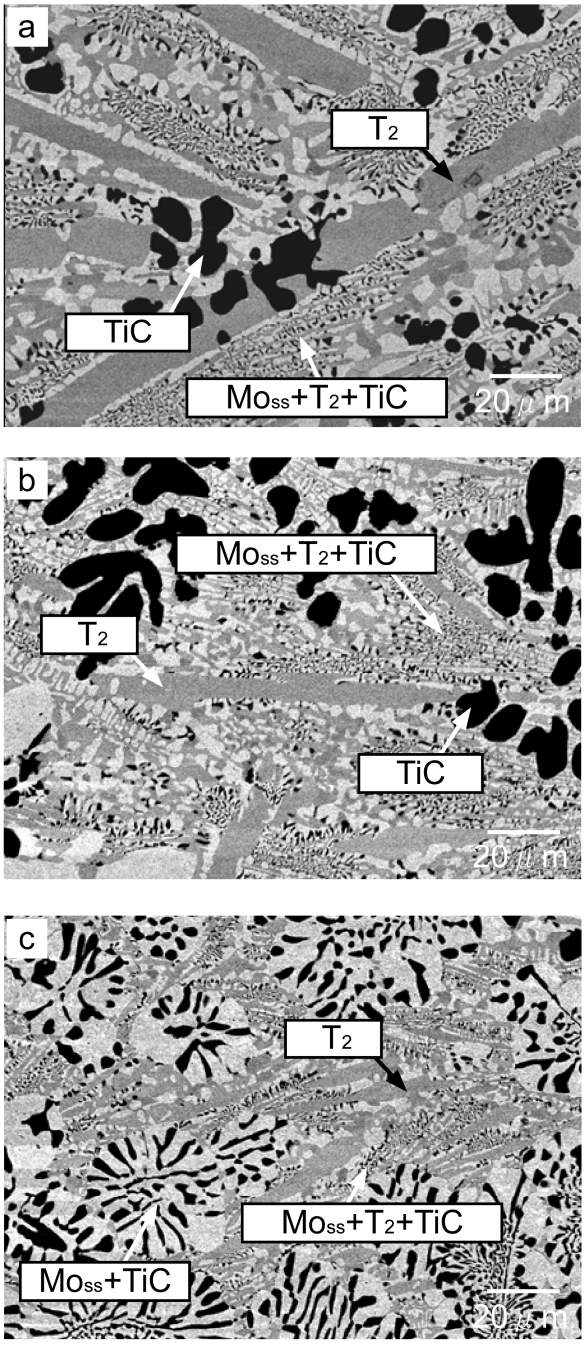


**Fig. 5.6 Microstructure change with increasing Mo content; (a) C2, (b) C3 and (c) C4 alloys.**

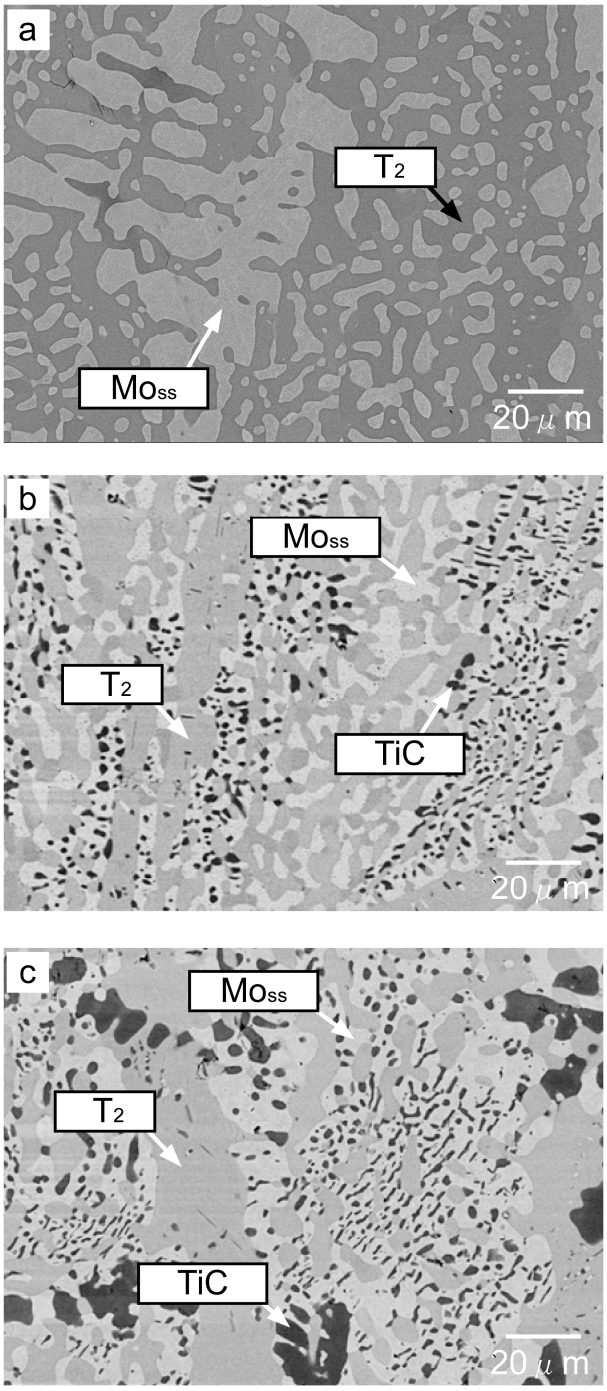


**Fig. 5.7 Microstructure change with increasing TiC content after heat treatment at 1800 ˚C; (a) Ternary, (b) C1 and (c) C2 alloys.**

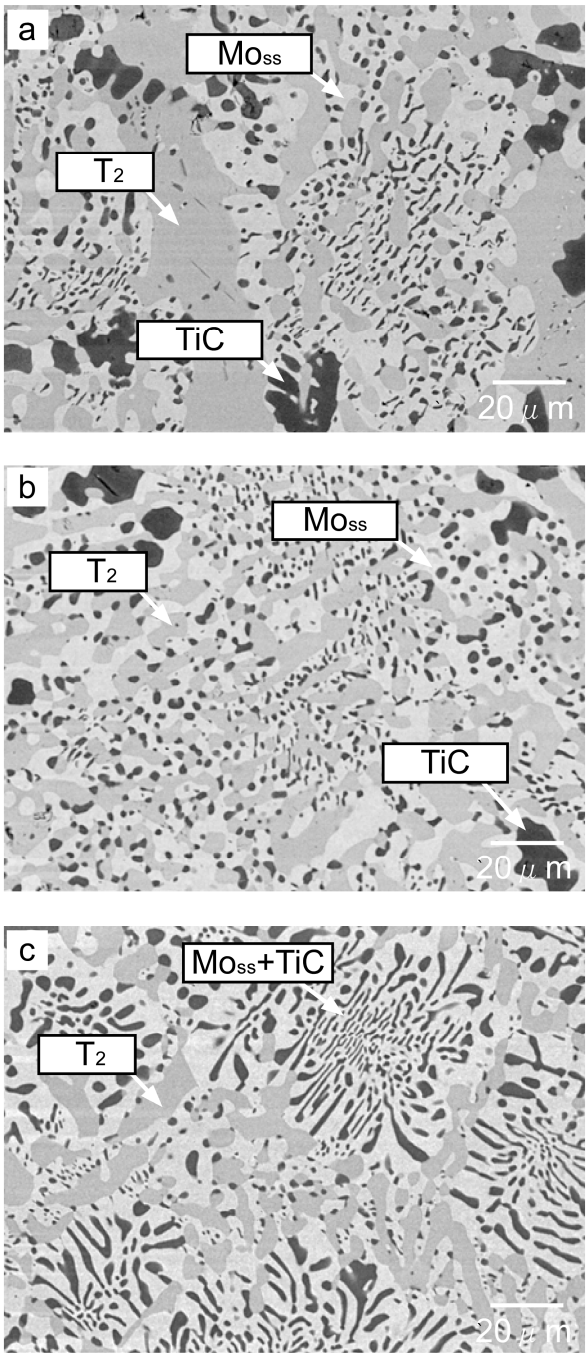


**Fig. 5.8 Microstructure change with increasing Mo content after heat treatment at 1800 ˚C in TiC addition; (a) C2, (b) C3 and (c) C4 alloys.**

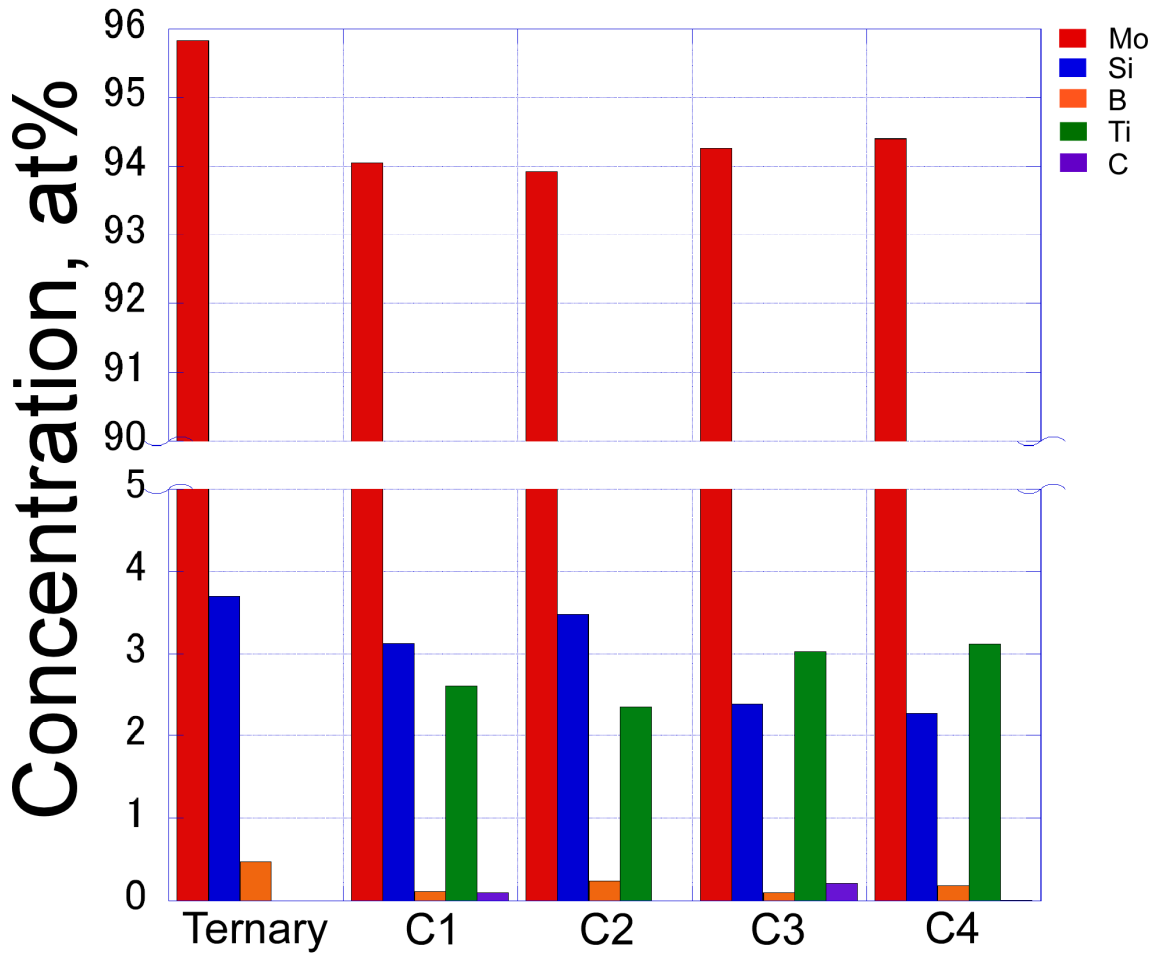


**Fig. 5.9 Concentration of the constituent elements in $Mo_{ss}$ determined by EPMA.**

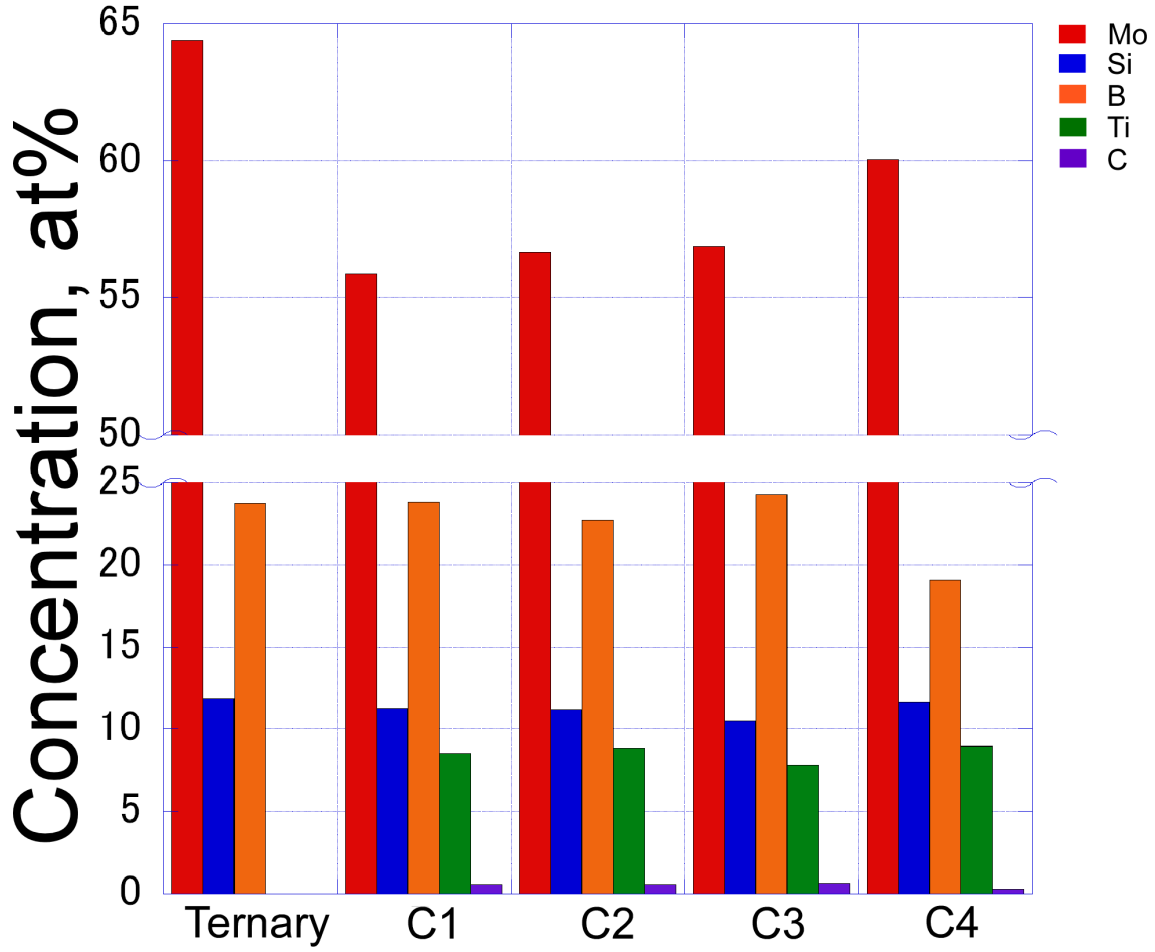


**Fig. 5.10 Concentration of the constituent elements in $T_2$ determined by EPMA.**

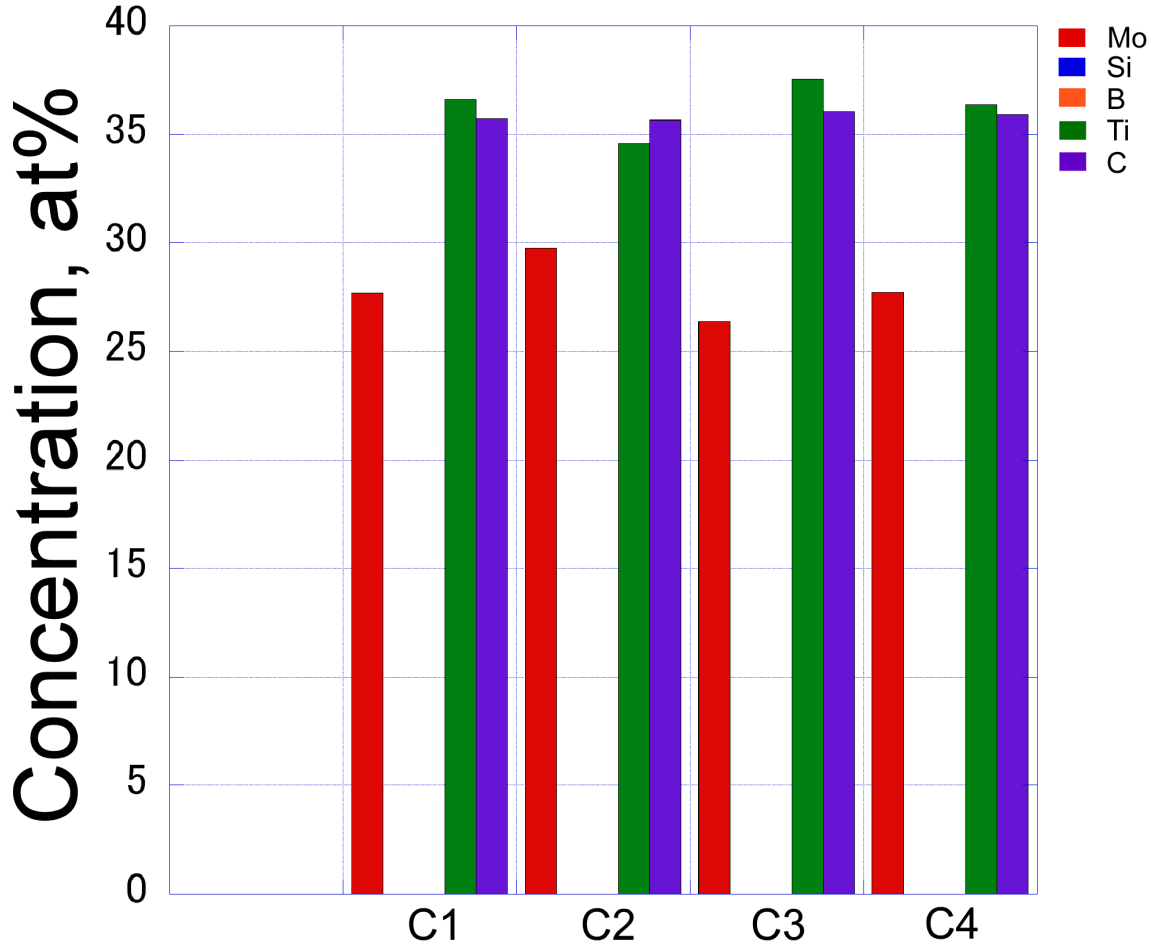


**Fig. 5.11 Concentration of the constituent elements in TiC determined by EPMA.**

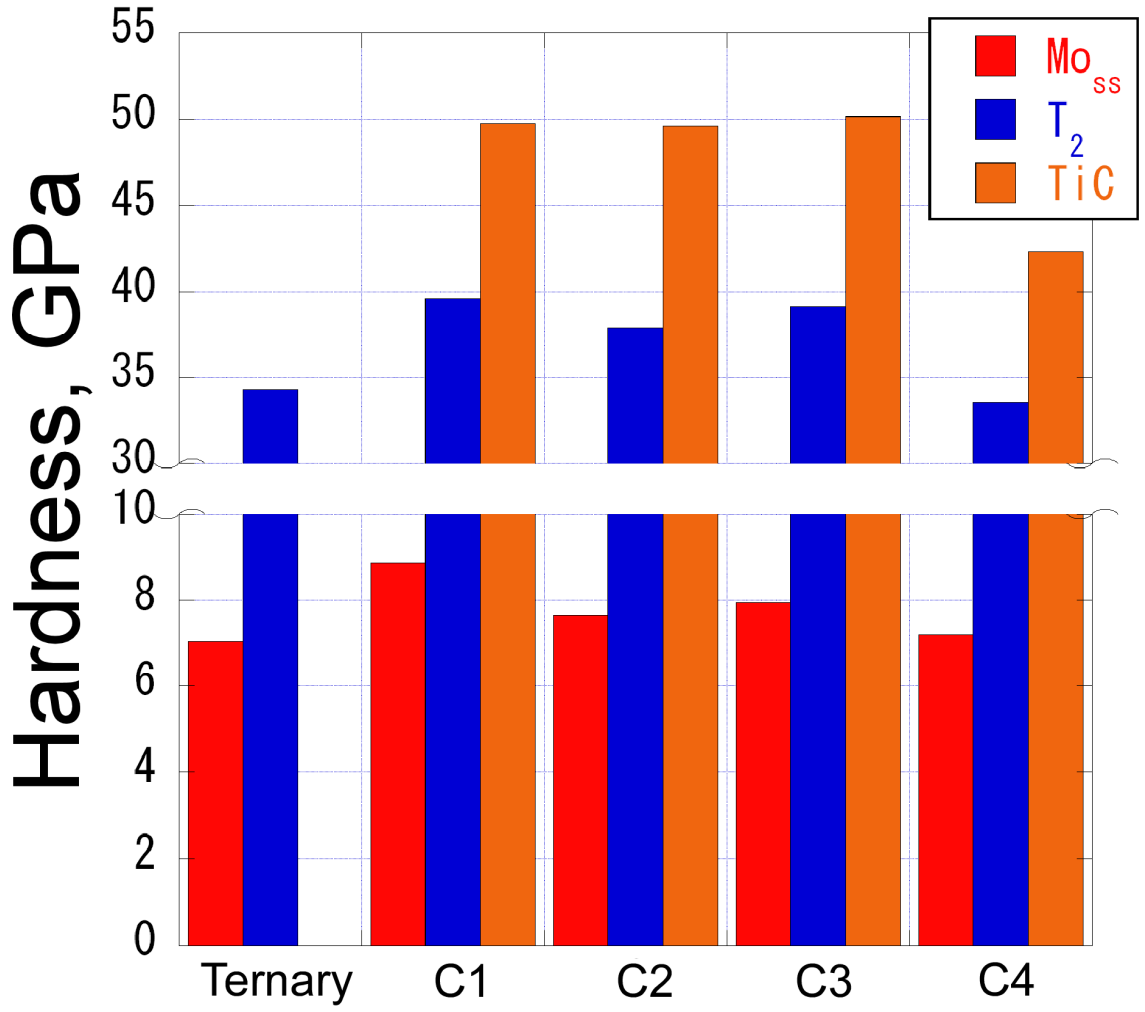


**Fig. 5.12 Hardness of the constituent phases in the alloys after heat treatment at 1800 ˚C determined by nanoindentation.**

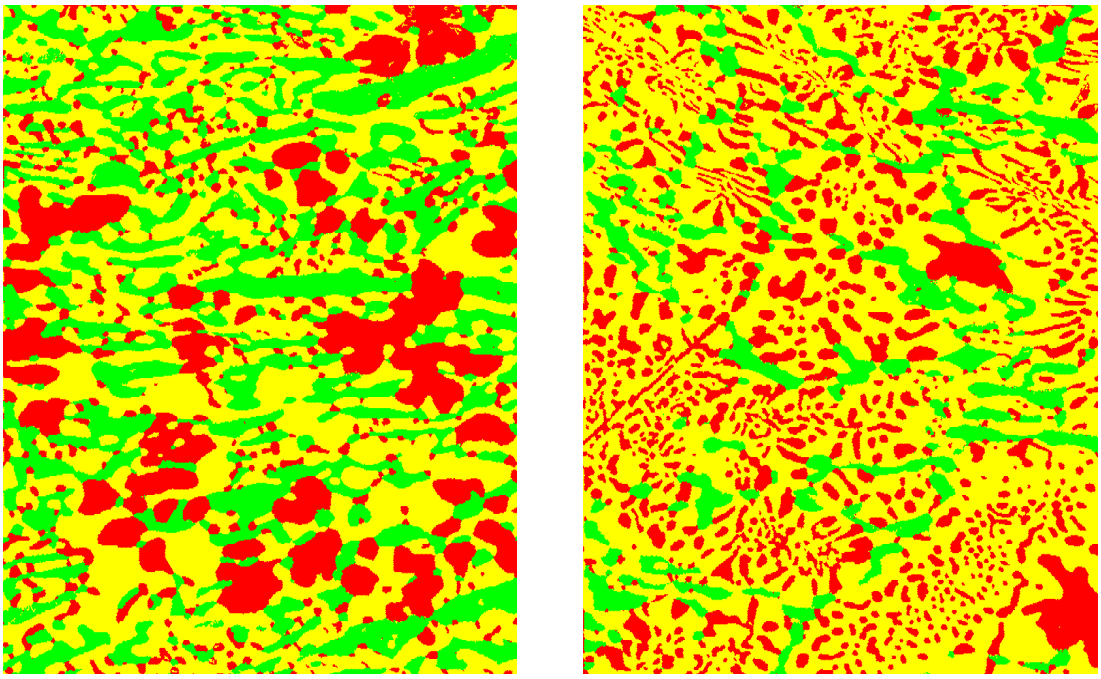

**Volume fraction**

| Alloy | $Mo_{ss}$ | $T_2$ | TiC |
|---|---|---|---|
| **C3** | 43.6% | 27.5% | 29.0% |
| **C4** | 60.5% | 16.0% | 23.5% |

**Fig. 5.13 Volume fraction of the constituent phases in the alloys after heat treatment at 1800 ˚C determined by EBSP.**

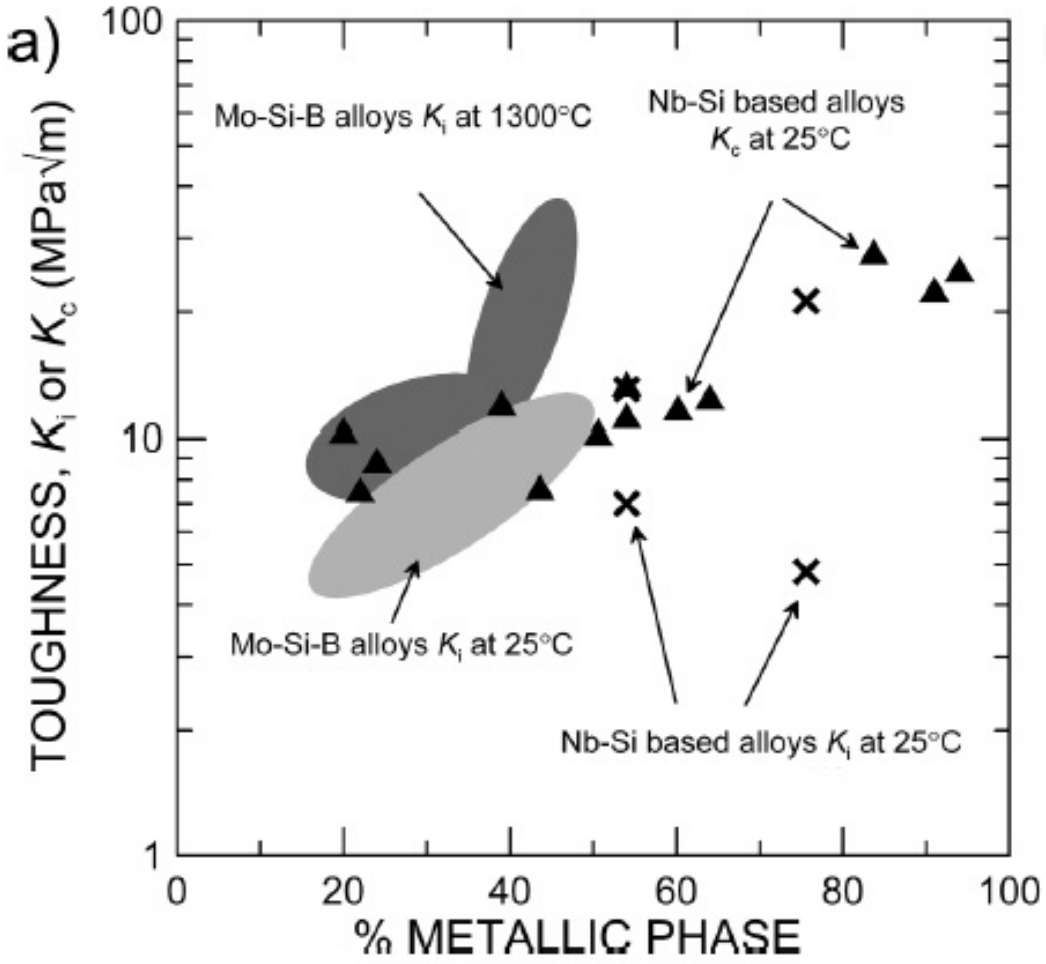


**Fig. 5.14 Relation between fracture toughness and metallic phase in Mo-Si-B alloy suggested by Kruzic et al. [9].**

# CHAPTER 6

## Summary

This study dealt with microstructure formation through eutectic reactions and determination of isothermal phase diagram at 1800 °C in Mo-rich Mo-Si-B Alloys and these were carried out based on EPMA quantitative analysis with the correction devised in the present study. The behavior of TiC in Mo-Si-B ternary system was investigated in terms of microstructure formation and phase equilibrium. The conclusions of each chapter are summarized as following.

In chapter 2, EPMA correction with standard samples aimed to the stoichiometric compositions of $T_2$, $Mo_{ss}$, $Mo_3Si$, $Mo_5Si_3$, $Mo_2B$ and MoB was carried out for accurate element measurement in quantifying those single phases in Mo-rich portion of Mo-Si-B system. Correction method with using standard samples was successfully determined to define each single phase in Mo-rich portion of Mo-Si-B system. Single phase after heat treatment at 1800 °C was not obtained even though the standard samples were aimed to their stoichiometric composition. The samples aimed to $Mo_5Si_3$ single phase showed no existence of precipitates, indicating that it might be single phase. Based on pure Mo,

$SiO_2$ and $NdB_6$ as standard sample, the B concentration was as excessive as the compositions of the boride phases were largely deviated from their stoichiometric compositions. In $Mo_{ss}$ and silicide phases, the B solubility can not be accurately determined. After correction, the B solubility was determined in the range of 0~1at% in $Mo_{ss}$ and the silicides and the compositions of the borides corresponded to those of stoichiometry.

In chapter 3, the phase formation behavior of the Mo-Si-B system during solidification was experimentally examined around the $Mo_{ss}$-$T_2$ and Mo-$Mo_3Si$-$T_2$ eutectic points in the Mo-Si-B liquidus projection proposed by Yang et al. The primary phase formation observed in this study was in good agreement with that of the liquidus projection by Yang et al. Alloy 1 (Mo-9.5Si-14.2B) with a composition closest to the $Mo_{ss}$-$T_2$ point had two microstructural areas, $Mo_{ss}$-$T_2$ superfine eutectic and $Mo_{ss}$-$T_2$-A15 fine three-phase areas. Alloy 5 aimed to that of the Mo-$Mo_3Si$-$T_2$ eutectic point also showed the development of fine $Mo_3Si$-$T_2$ eutectic phase. Utilizing the microstructural and compositional homogeneity of Alloy 1 and 5, the quantitative analysis results obtained by EPMA were well calibrated, with particular interest in the results for B. Alloy 2, 3 and 4 showed the existence of primary phases; $Mo_{ss}$, $Mo_2B$ and $T_2$, respectively. From the existence of the $Mo_5Si_3$-$T_2$ phase by monovariant eutectic

reaction in the microstructure of Alloy 6, it was reconfirmed that the result of this study was in a good agreement of the liquidus projection by Yang et al. From the EPMA results, it was realized that the compositional information is limited in what primary reaction is in liquidus projection. The compositional solidification route following the $Mo_{ss}$-$T_2$ and $Mo_{ss}$-$Mo_3Si$-$T_2$ eutectic reaction was suggested.

In chapter 4, the solubility or compositional limits of the single phase regions at 1800 °C in the Mo-rich portion of the Mo-Si-B ternary system were quantitatively determined using the alloys corresponding to three-phase regions. For accurate composition determination by EPMA, the correction was carried out using standard samples originally prepared aimed to each single phase composition. The solubility limits at 1800 °C in all the single phase regions obtained with the correction appear to be different with those of the previous reports at 1600 °C, especially for low level solubility. In the present study, the solubility was determined in the level of 0~1at%. The most interesting thing is that $T_2$ single phase region determined in this study doesn't include its stoichiometric composition. This would be direct evidence that $T_2$ single phase can not be obtained, even though it was aimed to the stoichiometric composition.

In chapter 5, density change, microstructure formation and phase equilibrium at 1800 °C were investigated for TiC-synthesized Mo-Si-B alloys. The conclusions are

listed as following. With TiC addition, the density of Mo-Si-B alloys was reduced to a level lower than that of pure Ni. In as-cast microstructures, Mo-7.3Si-14.6B alloys showed coarse primary $Mo_{ss}$, while TiC or $Mo_{ss}$-TiC eutectic appeared as primary by TiC addition. $Mo_{ss}$ particles in TiC added alloys were refined by the formation of TiC or $Mo_{ss}$-TiC eutectic as primary and $Mo_{ss}$-$T_2$-TiC three-phase eutectic. After heat treatment at 1800 °C, the microstructure of Mo-7.3Si-14.6B consisted of $T_2$ and coarse $Mo_{ss}$ particles formed from the combination of primary $Mo_{ss}$, while TiC added alloys showed the uniform distribution of fine TiC particles and $Mo_{ss}$ continuous phase. From EBSP result and the density, it was confirmed that Mo-3.4Si-6.8B-15TiC alloy had about 60 % $Mo_{ss}$ in volume fraction and the density comparable with that of pure Ni, simultaneously. Mo-Si-B alloy having 50 % $Mo_{ss}$ in volume fraction showed the fracture toughness of 12 $MPa \cdot m^{1/2}$ according to a previous report. Therefore, it is suggested that Mo-3.4Si-6.8B-15TiC alloy may have a value higher than 12 $MPa \cdot m^{1/2}$ in fracture toughness.